Biotechnological applications of thermophoresis

Dissertation

zur Erlangung des Grades
Doktor der Naturwissenschaften (Dr. rer. nat.)

der Fakultät für Physik
der Ludwig-Maximilians-Universität München

vorgelegt von
Christoph Jens Wienken
aus Kissing

München, Mai 2011

Erstgutachter: Prof. Dr. Dieter Braun

Zweitgutachter: Prof. Dr. Hermann E. Gaub

Mündliche Prüfung am 04. Juli 2011

Table of Contents

I. Summary

For over 150 years it is known that particles in a temperature gradient conduct a directed movement. This is called the Soret effect or thermophoresis. Still the underlying physical principles of thermophoresis in aqueous solutions are not totally understood. In the first part of this thesis new experiments on the thermophoresis of small single-stranded DNA oligonucleotides try to elucidate the fundamental principles of the Soret effect and the results seem to support a thermodynamic description of the thermophoretic movement. With this approach the experimental results for DNA could be predicted without free fitting parameters. Assuming this theory the thermophoretic movement mainly depends on the strength of ionic shielding and on the hydration sphere of the particle. This direct influence of the water-particle interface implicates that thermophoresis is very sensitive to even slight changes of particles. Applied to biomolecules like DNA or proteins the Soret effect allows for a precise analysis of the molecule under investigation. Any binding reaction, for example, will at least result in a change of the hydration sphere of the molecule and thus, binding reactions are readily accessible with thermophoresis.

This is demonstrated in the second part of this work. The experiments range from DNA aptamers binding to nucleotides or proteins over protein-protein interactions to single ion binding. Especially low molecular weight binders like small molecules or ions are notoriously difficult to measure with standard interaction analysis tools. Interestingly, in thermophoresis measurements the signal to noise ratio does not significantly depend on the molar weight ratio as it is the case for other interaction analysis techniques. High affinities in the nanomolar regime are equally well measured as low affinities in the high micromolar range. The thermophoretic method also allows monitoring interactions of biomolecules directly in biological liquids like cell lysate or blood serum. To overcome potential influences of the typically used fluorescent label on the interaction strength, intrinsic protein fluorescence is also suitable for monitoring the thermophoretic movement of proteins. This approach allows a complete label-free measurement of protein interactions directly in solution without any labeling or surface functionalizing procedure.

Third, also structural changes of molecules could be analyzed with thermophoresis. This is demonstrated in the last part of this thesis with measurements on the thermal stability of nucleic acids. Most conformational changes affect at least the hydration sphere of a molecule and thus lead to a measurable readout in the thermophoresis signal. Again, the thermophoretic method shows a high sensitivity for small changes in the molecule structure and thus, allows for revealing intermediate states upon the unfolding of nucleic acids.

Zusammenfassung

Bereits vor mehr als 150 Jahren entdeckten Charles Soret und Carl Ludwig die Bewegung von Teilchen in einem Temperaturgradienten. Aber bis heute sind die zugrundeliegenden Mechanismen für diese Thermophorese (auch Soret Effekt) in wässrigen Lösungen nicht vollständig verstanden. Im ersten Teil dieser Arbeit wurden neue Experimente mit kurzen einzelsträngigen DNA Oligonukleotiden durchgeführt, um die fundamentalen Prinzipien der Thermophorese aufzuklären. Die gewonnenen Ergebnisse unterstützen eine thermodynamische Beschreibung des Soret Effekts und es war möglich mit dieser Theorie die Messergebnisse ohne freie Fitparameter vorherzusagen.

Von dieser Theorie ausgehend bestimmen hauptsächlich die ionische Abschirmung eines Teilchens in Lösung und die Hydrathülle die thermophoretische Bewegung. Der direkte Einfluss der Hydrathülle impliziert, dass die Thermophorese äußerst sensitiv auf kleinste Änderungen in den Eigenschaften der gemessenen Teilchen sein sollte. Der Soret Effekt sollte also eine sehr genaue Charakterisierung von Biomolekülen wie beispielsweise DNA Molekülen oder Proteinen erlauben. Damit sind auch Analysen von Bindungsreaktionen möglich, da jedes bindende Molekül mindestens die Hydrathülle ändern sollte.

Im zweiten Teil der Arbeit wurde die breite Anwendbarkeit der Thermophorese zur Analyse von biomolekularen Interaktionen dargestellt. Dafür wurden Interaktionen aus vielen verschiedenen Biomolekülklassen analysiert, angefangen bei DNA Aptameren die Proteine oder einzelne Nukleotide binden, über Protein-Protein Interaktionen bis hin zu so kleinen Bindungspartnern wie einzelnen Ca^{2+}-Ionen. Hoch affine Interaktionen im nanomolaren Bereich konnten mit einer ähnlichen Genauigkeit gemessen werden wie schwach affine Bindungen im hohen mikromolaren Bereich. Außerdem erlaubt die thermophoretische Messmethode, Interaktionen direkt in biologischen Flüssigkeiten, wie zum Beispiel Zelllysat oder Blutserum, zu messen. Um einen möglichen Einfluss des Fluoreszenzlabels auf die Interaktion zu verhindern, kann bei vielen Proteinen die intrinsische Proteinfluoreszenz genützt werden. Dies erlaubt die Molekülbewegung von nativen Proteinen zu messen und schafft die Grundlage für eine Label-freie Analyse von Interaktionen direkt in Lösung.

Desweiteren kann Thermophorese dafür verwendet werden, um Konformations-änderungen von Molekülen zu beobachten, da diese meist mit einer Änderung der effektiven Ladung (und damit der ionischen Abschirmung) oder der Hydrathülle einhergehen. Dies wurde im dritten Teil dieser Arbeit verwendet um die thermische Stabilität von Nukleinsäuren zu messen. Dabei konnten aufgrund der hohen Sensitivität des Soret Effekts intermediäre Zustände beim Aufschmelzen der DNA gefunden werden.

II. Introduction - Thermophoresis of biomolecules

Like charged molecules move in electrical fields, temperature gradients also induce a directed motion of molecules. The effect is known as thermophoresis, thermodiffusion or Soret effect. In liquids it was first observed by Carl Ludwig in 1855, who found a change in the concentration of salt ions induced by temperature gradients (1). During the last century the effect was used to concentrate particles in so-called Clusius tubes (2-3). Thermophoresis in combination with a fluid flow is further discussed as a mechanism to accumulate biomolecules in hydrothermal vents in the deep sea (4). To shed light on the theoretical basis of thermophoresis Braun and Libchaber (5) as well as Piazza (6) have recently performed first experiments on thermophoresis of biomolecules. Although the underlying theoretical basis is still under debate, the importance of ionic contributions (i.e. charge), and nonionic contributions (i.e. molecular surface properties, hydration shell) for thermophoresis are now widely accepted (7-14). Today, different techniques exist to measure the Soret effect in aqueous solutions and many of these use optical means to analyze the temperature induced change in concentration. Diffusion cells, heated from above and cooled from below are the most simple approach but due to the millimeter sized dimensions of these cells equilibration times are rather slow in the order of hours (15). To overcome this limitation Köhler established an optical method which uses forced Rayleigh light scattering to infer the concentration change in solution (16). Another approach to measure the strength of the thermophoretic effect was developed by Piazza et al. who used the effect of thermal lensing to quantify the thermophoresis of biomolecules (17). An application of temperature gradients for analytical or preparative purpose is thermal field flow fractionation (ThFFF), a chromatographic technique for molecule separation. However, due to the comparably high temperatures needed for separation of molecules and limitations in resolution such instruments are rarely used for biomolecule analytics.

In the last years the availability of infrared laser diodes in the range of 1480nm, a fully developed fluorescence microscopy and highly reproducible glass capillaries offered new possibilities to measure the thermophoretic behavior of particles and especially of biomolecules. These approaches to measure the Soret coefficient of biomolecules and possible biotechnological applications are the topic of this thesis. In the following a detailed description of the method will be given and the usage of microscale temperature gradients for interactions studies and thermal stability studies will be discussed.

III. Theory and Experimental Details

While the theoretical basis for thermophoresis is still under debate a thermodynamic approach to describe the movement of particles has proved valid to describe the thermophoretic behavior of biomolecules like for example double stranded DNA. In the following this theory shall be discussed in more detail followed by a detailed description on how to experimentally measure the Soret coefficient of biomolecules.

a. Basics of thermophoresis

When an aqueous solution is locally heated particles start to move in the given temperature gradient. The resulting movement is described by a linear thermophoretic drift $v = -D_T \nabla T$ which is then counteracted by a backdiffusive flux $j = -D\nabla c$ with diffusion coefficient D. These two fluxes lead to a steady state molecule distribution which is characterized by the Soret coefficient. The Soret coefficient is defined as the ratio $S_T = D_T/D$ and determines the magnitude of the change in concentration in steady state. In steady state, a temperature difference ΔT results in a change in concentration Δc, which can be derived from the following equation (18).

$$\frac{c}{c_0} = \exp(-S_T \Delta T) \tag{1}$$

The concentration in the heated region c is normalized with respect the initial concentration c_0 before applying the temperature gradient.

But the theoretical models predicting thermophoresis in aqueous solutions are still subject of ongoing debate and experiments. There are various approaches ranging from hydrodynamic flow theories and thermo-electrophoresis (i.e. a Seebeck effect) to thermodynamic models (12-13). In case of the Seebeck effect, ions in the buffer move along a thermal gradient and give rise to an electric field, which in turn moves the molecules by electrophoresis (19-21). But it was found that for buffer systems based on NaCl which are used for many biotechnological applications, the resulting Seebeck contribution is suggested to be small (21) and cannot be responsible for the measured concentration gradients. To give an estimate if hydrodynamic flows can account for the particle movement an effective Peclet number P_e is calculated:

$$\mathrm{P_e} = a\frac{v}{D} = a\frac{D_T}{D}\nabla T = aS_T \nabla T \tag{2}$$

Here, a denotes the particle radius, v the particle drift velocity, D the diffusion coefficient, D_T the thermophoretic mobility, S_T the Soret coefficient and ∇T the temperature

gradient. For microscopic particles in moderate temperature gradients this Peclet number is much smaller than 1. Such a system is diffusion dominated and hydrodynamic flows play a minor role. Only provided that $P_e >> 1$, which is experimentally challenging to achieve even for micrometer-sized particles, a local fluid flow of solvent around the molecules could experimentally be confirmed (22).

In the limit of moderate temperature gradients, diluted molecules and under interface-free conditions, the steady state of thermophoresis can be described by a local Boltzmann distribution of the particle density. The diffusive movement of single molecules allows the reversible equilibration between particle positions due to temperature differences in the Gibbs free enthalpy of the molecule-solvent complex (7, 12-14, 23-24). Assuming a local equilibrium the Soret coefficient S_T is given by the temperature derivative of the Gibbs free energy G of the molecule-solvent complex (7, 18):

$$S_T = \frac{1}{k_B T}\frac{\partial G}{\partial T} = -\frac{S}{k_B T} \qquad (3)$$

The second part of the equation is derived by locally applying the thermodynamic relation dG=-SdT+Vdp+μdN. For single particles at constant pressure the Soret coefficient equals the negative entropy S of the particle-solvent system. In water, two contributions dominate the particle entropy: the entropy of ionic shielding and the entropy of hydration (Figure 1). Effects of particle-particle interactions can be neglected as we normally work in highly diluted systems. The entropy of ionic shielding can be calculated from the temperature derivative of Gibbs free enthalpy. This enthalpy can be interpreted as the electric energy stored in a capacitor build of the molecule's surface and the surrounding ion cloud.

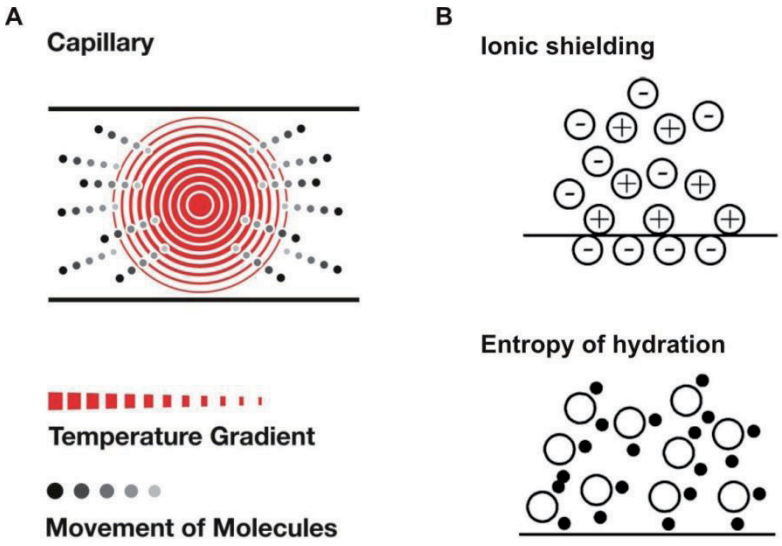

Figure 1 Schematic drawing of thermophoresis and its molecular contributions. ***(a)*** *Molecules move in a temperature gradient, an effect termed thermophoresis. Typically, in aqueous solutions the movement is directed away from regions of elevated temperature.* ***(b)*** *Thermodiffusion in water is dominated by ionic shielding (top) and water hydration (bottom) (Illustration from Duhr et al. (7)).*

With these contributions the Soret coefficient can be written as:

$$S_T = \frac{A}{k_B T}\left(-s_{hyd} + \frac{\beta\sigma_{eff}^2}{4\varepsilon\varepsilon_0 T}\lambda_{DH}\right) \qquad (4)$$

Here, s_{hyd} is the hydration entropy per molecule surface area A, k_BT the thermal energy, σ_{eff} the effective charge per surface area and ε and ε_0 the permittivity of water and free space, respectively. λ_{DH} represents the Debye length corresponding to the salt concentration in use. The parameter β contains the temperature dependence of both permittivity of water (25) and Debye length: $\beta = 1 - (T/\varepsilon)(d\varepsilon/dT)$. In Eq. 4, s_{hyd} accounts for the change in water structure due to the presence of the molecules, including for example the creation of the water cavity for the molecule and the hydrophobic interactions at its interface. The direct contribution from Brownian motion is typically small ($S_T = 0.0034\ K^{-1}$). However it can make a contribution for small molecules measured at large salt concentrations and thus add a small error to a derived value for the entropy of hydration.

The approach was tested with polystyrene beads with varying particle size, salt concentration and temperature and for the case of double stranded DNA with varying length. The theory could characterize the Soret coefficient quantitatively without fitting

parameters (7). Further confirmation of the approach resulted from the study of quartz beads (26). Extensions of the theory were reported in (27). Subsequent experiments on polystyrene beads (28) came to different conclusions concerning the size dependence. However, the thermodynamical description of thermophoresis depicts the movement of small particle in solutions quite well and indicates that the Soret effect might be able to monitor changes on a molecular level as they occur for example along binding reactions.

b. Schematic Experimental Setup

The setup used to acquire the thermophoretic properties of fluorescently labeled molecules consists of a modified fluorescence microscope (Figure 2). An IR laser is coupled into the beam of light with a dichroic mirror, which reflects IR radiation and is transparent for visible light. Both the IR beam and the fluorescence light are focused into the same plane in the sample with the microscope objective. The information about the thermophoretic movement is collected with a standard CCD camera.

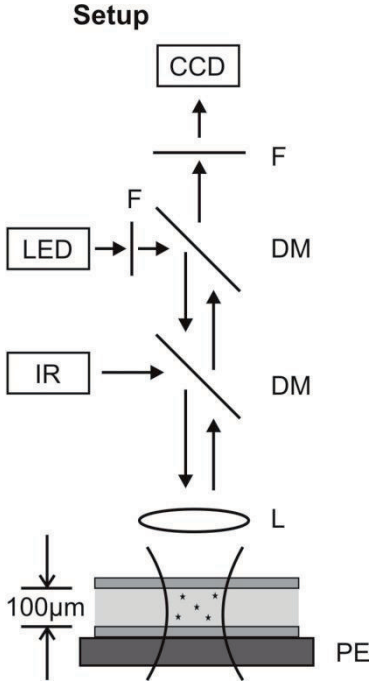

Figure 2 Experimental setup for thermophoresis measurements. *An epi-fluorescence microscope is extended by an additional dichroic mirror (DM) that couples an infrared laser (IR) into the beam of light. The laser is focused into an aqueous solution inside a capillary. Due to absorption of IR radiation by the water molecules it creates a local temperature profile that allows quantifying the Soret coefficient of particles in the solution. The capillary is placed on top of a peltier stage (PE) to adjust the overall sample temperature. L, lens; LED, light emitting diode; F, filter; CCD, CCD camera.*

For measuring the low light intensities found for intrinsic protein fluorescence, the CCD camera is exchanged with a photomultiplier tube which allows analyzing the concentration change of proteins without additional fluorescence label.

The sample is provided in glass capillaries that are placed between the objective of the microscope and a peltier element used to adjust the overall sample temperature. An automation of the setup was achieved by placing the peltier element on top of a 1d-translation stage. With this, multiple samples can be measured in series without any action of the user needed. This leads to an increase in accuracy when measuring the Soret coefficient of multiple samples, for example when analyzing the change of the thermophoretic effect upon binding events. A more detailed description of the setup is found in Appendix A of this thesis.

c. Thermophoresis Measurements

To measure the thermophoretic properties of particles or biomolecules time traces of the developing concentration profile are recorded. This allows inferring all necessary information for an evaluation of the Soret coefficient. All images were normalized to images before laser heating to correct for minor illumination inhomogeneities of the microscope. After switching on the laser heating the evaluation of the fluorescence signal allows to monitor temperature dependent particle properties. On short time scales around 100ms the change in fluorescence due to the temperature rise is analyzed. This temperature dependence of the dye highly depends on the fluorophor in use and was found to be in the order of 0.0 %/K - 0.24 %/K for the fluorophor HEX. The temperature dependence was also determined in independent measurements using the temperature controlled peltier stage. This information about temperature effects of the dye is included into the analysis when a highly precise absolute value for the Soret coefficient was necessary like for the analysis of the thermophoretic properties of single-stranded DNA. When analyzing relative changes of the Soret coefficients due to binding or unfolding of a molecule a more simple approach was used to correct for the temperature dependence of the fluorophor. As thermophoresis and the establishing of the temperature profile happen on clearly separated time scales (29-30) it was possible to analyze the change relative to the situation after the temperature response of the dye but before thermophoresis has lead to a change in concentration of the molecules. This is done by normalizing the time traces not to images before switching on the laser but to images around 200ms after the start of laser heating. By doing so, the change in fluorescence is only due to a change in

concentration and not due to a temperature. This approach results in a slight underestimation of the Soret coefficient but relative changes in the Soret signal still remain unchanged. On longer time scales thermophoresis leads to a change in concentration in the heated region which is counteracted by diffusion. After some time a steady state profile is established. This occurs on time scales of seconds to minutes depending on the molecules under investigation. Figure 3 shows such a corrected fluorescence time trace from which the Soret coefficient can now be inferred.

When switching of the IR heating the depleted molecules diffuse in the concentration gradient established by thermophoresis and reestablish the initial homogenous concentration profile. From this backdiffusion the Stokes-Einstein diffusion coefficient D can be inferred which allows an independent measurement of the size of the particles.

To increase the accuracy of the measurement by minimizing bleaching artifacts, low excitation intensities are used. Still photobleaching occurs and results in an exponential decay of fluorescence signal over time. For measurements for which a precise absolute value of the Soret coefficient is necessary, the fluorescence time traces were corrected for this effect.

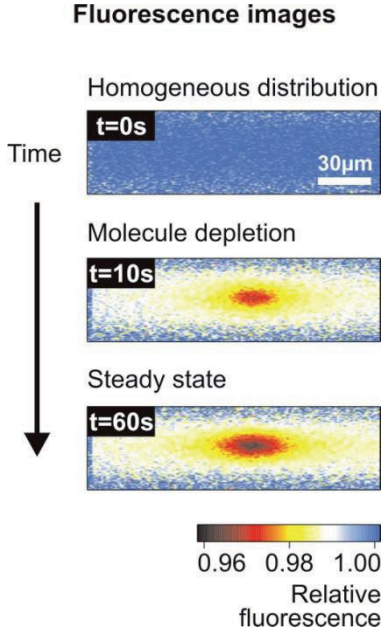

Figure 3 Fluorescence images. *Fluorescence images are acquired over time. Initially, fluorescently labeled molecules are distributed evenly. After switching on the heating with a focused infrared-laser, the molecules experience the thermophoretic force in the temperature gradient and typically move out of the heated spot. In the steady state, this molecule flow is counterbalanced by ordinary mass diffusion and a steady-state concentration profile is established. From the concentration profile the Soret coefficient is inferred.*

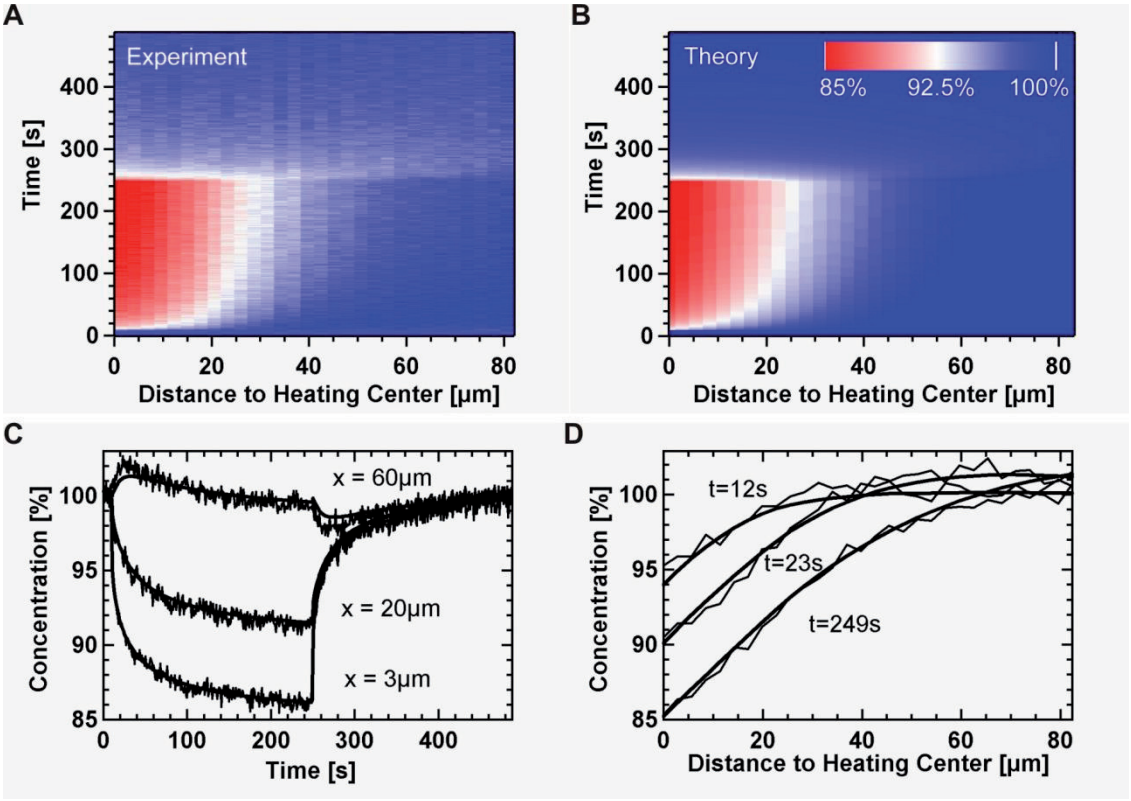

Figure 4 Thermophoresis in experiment and theory. *Comparison of measurements and simulations for a 50-base Single stranded DNA molecule at a Debye length of* λ_{DH} *= 3.7 nm.* ***(a, b)*** *The concentration in a space–time plot of the thermophoretic depletion is represented by colors. The experimental space–time (a) is well described by the theoretical space–time (b).* ***(c)*** *Change of the concentration over time is evaluated at different positions along the capillary.* ***(d)*** *Concentration profiles parallel to the capillary at its center at specific times are well described by the simulated concentration profiles using the 2-D model. Note that the information represented in (c) and (d) are vertical and horizontal cross sections of the space–time plot at fixed values of distance or time, respectively.*

The corrected concentration profiles over time can be illustrated in a space time diagram which also allows comparing the experimental data with a theoretical model. This was done when investigating the Soret coefficient of single-stranded DNA molecules. Figure 4A-B shows such a plot for a 50nts DNA oligomer. On the bottom Figure 4C-D shows cross-sections in space and time to illustrate the fine agreement between theory and experiment.

The experimental error for S_T measurements is ± 0.0021/K due to noise of the fluorescence signal in addition to a relative error of ±2.3% to ±4% which accounts for the precision of the temperature measurements. Diffusion constants are determined with an

accuracy of ±10% to ±20% since depletion kinetics of simulations match measured traces equally well within this range (31).

d. Conclusions

In contrast to most state of the art techniques to infer thermophoretic parameter the described fluorescence based approach offers simple access to the concentration changes in solution. For diluted concentration regimes the recorded fluorescence can be assumed to be linear and thus is an ideal measure for the concentration profiles. Furthermore, using an IR laser in combination with a microscope objective allows creating temperature profiles on the micrometer scale which speeds up thermophoresis measurements from hours to seconds.

Still, for inferring the Soret coefficient from the acquired concentration profile precise knowledge of the temperature profile in the sample is necessary. This is typically done by measuring the temperature dependent change in fluorescence of the dye. The temperature dependence has to be acquired in a separate experiment and then can be used like a molecular thermometer. The acquisition of the temperature profile can be performed simultaneously with the normal thermophoresis measurement using a second fluorophor at a different wavelength. However, using glass capillaries that are highly reproducible allows a determination of the temperature profile once before the actual Soret experiment. This is especially important if the Soret coefficient of more than one sample shall be measured and if an automation of the Soret analysis is required.

Furthermore, the combination of the fluorescence based thermophoresis setup with a one dimensional translation stage allows measuring multiple samples in series. As the translational stage has a positioning precision around 3 microns and capillaries are typically 100 microns in diameter the repeatability of the created temperature profile in the capillary is very high and the signals of different samples can be compared directly. This is especially important for measuring the change of the thermophoretic parameters when binding affinities shall be determined with thermophoresis.

IV. Thermophoresis of single-stranded DNA

To check the proposed capacitor model of thermophoresis (eq. 4) the thermophoretic properties of particles have to be measured over a changing Debye length. While it is difficult to precisely chemically modify the surface of polystyrene beads in a way that the modification is independent of particle size, DNA is a highly defined and characterized molecule. DNA is biologically highly relevant and gives us highly defined length and molecule characteristics.

a. Measurements of ssDNA

The Soret coefficient of single stranded DNA molecules of 5, 10, 22 and 50 bases length, diluted to a concentration of 1 μM, was measured in solution as a function of salt concentration. The Debye shielding length is inversely proportional to the square root of salt concentration. The solution was buffered with 1mM TRIS at pH 7.6. Salt concentrations in the range between 2 mM and 500 mM KCl were investigated. This range corresponds to Debye shielding lengths of 5.6 nm and 0.43 nm respectively. Values for D and S_T were obtained by fitting the measured data in a spacio-temporal manner. Soret coefficients scale linearly with Debye length for all molecules with a small intercept at $\lambda_{DH} = 0$ (Figure 5A). The diffusion constants (Figure 5B) decrease with increasing oligonucleotide length.

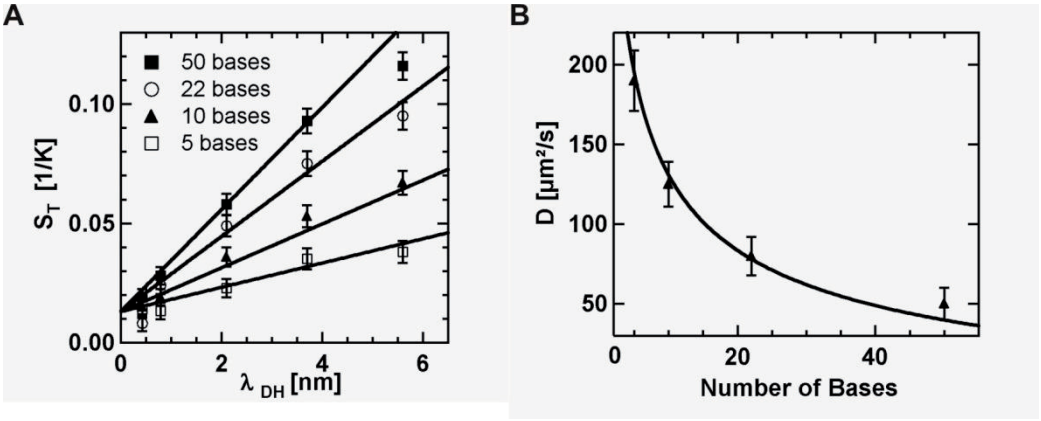

Figure 5 Salt dependence. (a) *The Soret coefficient ST versus Debye length for single stranded DNA ranging from 5 to 50 bases in length. The linear increase is quantitatively described by eq. 4 with* $Q_{eff} = 0.5e$*/base without fitting parameters other than the comparably small offset at zero Debye length.* ***(b)*** *Diffusion coefficients for the DNA molecules obtained from the same measurement. Values are well fitted with a power law* $D \sim \#\,bases^{-0.45}$.

Considering that for short ssDNA the fluorescent label cannot be neglected and will result in a slightly reduced diffusion coefficient, the results are in fair agreement with literature values (32-33). Diffusion constants are fitted with a power function. Including a minor offset we find D proportional to $L^{-0.45}$ with L denoting the number of bases.

The theory of counterion condensation predicts an effective charge of 0.6 e/base for ssDNA (34-35). This value does not depend on salt concentrations in the range investigated here and is shown to be largely temperature insensitive. The surface area of the molecules was approximated to be spherical with a radius inferred from the measured diffusion coefficients according to the Stokes-Einstein relation. Measurements performed on longer ssDNA fragments (280 to 5386 bases) yield a persistence length ranging from 1 nm to 5 nm for salt concentrations in the 10^{-1} M to the 10^{-3} M regime (32-33). Assuming a polymer length of 1.5 nm for the 5-mer, persistence length is longer than polymer length for most measurements. But given a width of about 1nm for ssDNA, a spherical approximation is still feasible.

As seen in Figure 5A, the linear increase of S_T for ssDNA is described well by eq. 4 Besides an offset resulting from the entropy of hydration and the contribution of Brownian motion, no fitting parameters were used and the Soret coefficients were described microscopically from first principles. For each measurement point, the measured diffusion coefficient was used to infer the molecule size. The results of Figure 5A imply that the length dependence of the thermophoresis of ssDNA should be predictable as well. Starting with a fixed offset and interpolating the diffusion coefficient from the power law fit of Figure 5B, the length dependence of the Soret coefficient can be directly inferred without introducing additional external parameters (Figure ***6***). We see that the measured Soret coefficients are fairly well predicted by eq. 4 as a function of DNA length at various salt concentrations.

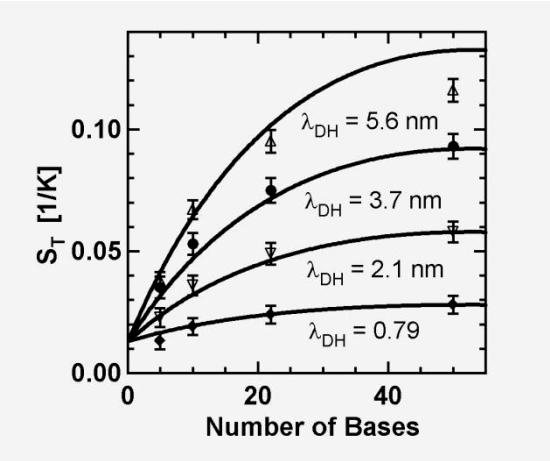

Figure 6 Length dependence. *The Soret coefficient as a function of DNA length calculated from eq. 4 with the interpolated diffusion coefficient obtained from Figure 5B. The measured S_T values match well the theoretical expectations for various salt concentrations, indicated by the respective Debye lengths.*

b. Conclusions

The measured Soret coefficients for short DNA oligonucleotides were predictable from the thermodynamics based theory without free fitting parameters. The experiments showed the predicted linear dependence of the Soret coefficient with the Debye length as well as the expected size dependence. From an extrapolation of the measurement data to a Debye length of 0nm, an estimation of the entropy of hydration of the molecules is accessible.

The optical thermophoresis measurements also allow obtaining the diffusion coefficients of the molecules under investigation. These values are in good agreement with previously measured datasets.

V. Binding studies with Thermophoresis

Methods to analyze proteins and their interactions with other biomolecules or low molecular weight compounds are of great importance for the evaluation of cellular functions and the development of pharmaceuticals. Potential drug candidates range from specifically designed aptamers and antibodies to low molecular weight compounds that inhibit or activate cellular processes. Although there are a variety of *in vitro* approaches which can address particular interactions, there is a constant need for new techniques. In particular, the analysis of binding processes of small molecules and the general complications of making measurements in biological liquids remain significant challenges in modern bio-analytics.

a. Thermophoresis - a tool to study biomolecular interactions

The thermophoresis of a labeled molecule A typically differs significantly from the thermophoresis of a molecule-target complex AT since the differential contributions from size, charge and solvation entropy do not compensate. This difference in the molecule's thermophoresis is utilized to quantify the binding in titration experiments under constant buffer conditions.

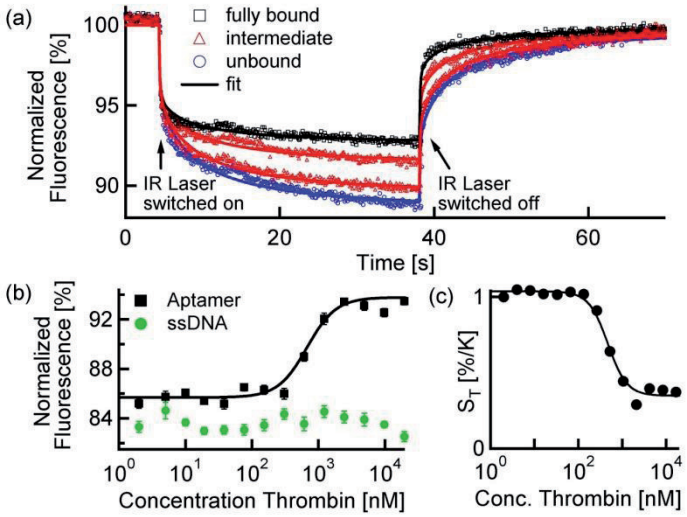

Figure 7 ***Thermophoretic binding studies.*** ***(a)*** *Time series of a DNA thrombin aptamer show different thermophoresis for the unbound and bound state.* ***(b)*** *The normalized fluorescence F_{norm} at t=30s is plotted for different concentrations of thrombin (black). From this a binding curve is inferred and the affinity of the interaction can be calculated. Random 25mer ssDNA (green) shows no change in thermophoresis with increasing thrombin concentration.* ***(c)*** *The Soret coefficient S_T equally reports the binding.*

To analyze binding events, the measurement is performed at various concentration ratios of the binding partners. Typically, the fluorescent binding partner is kept at a constant concentration and the unlabeled molecule is titrated until a saturation of all binding sites is obtained. Due to linearity of the fluorescence intensity and the thermophoretic depletion, the normalized fluorescence from the unbound molecule $F_{norm}(A)$ and the bound complex $F_{norm}(AT)$ superpose linearly. By denoting x the fraction of molecules bound to targets, the changing fluorescence signal during the titration of target T is given by:

$$F_{norm} = (1-x)F_{norm}(A) + xF_{norm}(AT) \qquad (5)$$

The analysis of the interaction of a 5.6 kDa aptamer to thrombin (MW = 37 kDa) is used to exemplify the principle of thermophoretic binding analysis. The thermophoresis of 100 nM thrombin-aptamer (36) was measured in 10% human serum with various concentrations of thrombin (0 nM to 19500 nM). The aptamer was labeled with a Cy5 dye at the 5' end. The observed time traces of the pure aptamer differ significantly from the traces of aptamers bound to thrombin (Figure 7a). Plotting the normalized fluorescence F_{norm} at a given time t against the varying thrombin concentration results in a binding curve (Figure 7b) with an EC_{50}=680 nM and a Hill coefficient of 2. Control experiments with a randomly chosen sequence ssDNA show no binding signal (Figure 7b).

This measurement principle is now applied to various classes of biomolecules to show the broad applicability of thermophoresis to analyze bimolecular interactions. Especially interactions of uncharged proteins were expected to be difficult to measure as the Soret effect for proteins is much smaller than for example for highly charged DNA molecules.

b. Protein binding reactions measured with thermophoresis

Specific interactions between proteins play a fundamental role in cellular functions and are important for biotechnological applications and antibody-based assays. In the following, several typical experiments are shown demonstrating the feasibility of thermophoresis for use in interaction studies in the course of drug development or pharmaceutical research.

As a first example for protein-protein interactions obtained with thermophoresis the affinity of an antibody for its antigen was analyzed. The interaction of an anti-Interferon-gamma antibody (Anti-IFN-γ, 120 kDa) with its antigen, human interferon gamma (hIFN-γ, 17 kDa) was chosen as hIFN-γ plays an important role in cell processes (37). The interaction showed that also protein thermophoresis leads to sufficient thermophoresis signals which allow for a discrimination of different binding states.

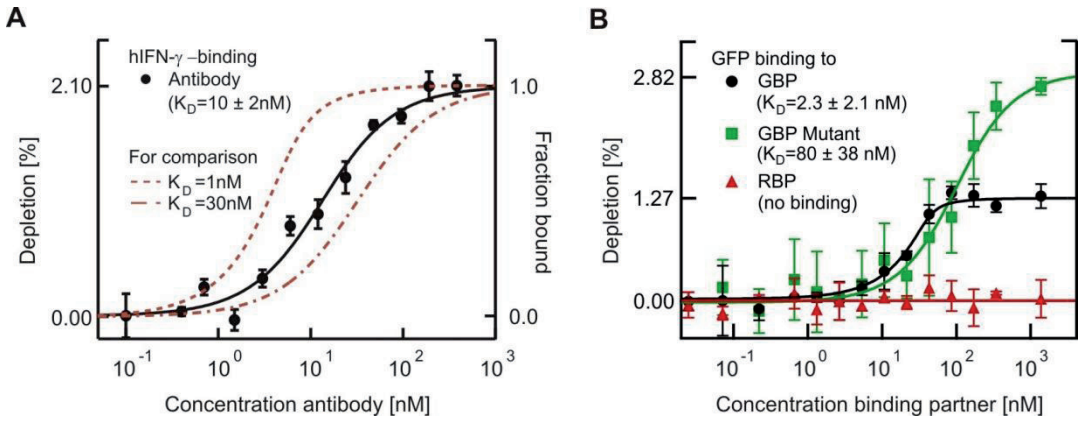

Figure 8 Protein–protein interactions measured with MST. *(a) The binding of fluorescently labeled hIFN-γ to a specific antibody is analyzed with MST. The dashed lines illustrate the resolution of the measurement.* ***(b)*** *The interaction of the intrinsic fluorescent protein GFP with binders of varying affinities is measured. The GBP shows a high affinity of 2.3 ± 2.1 nM (black circles), while a GBP mutant (R37A) shows a reduced binding strength. A non-binding RBP shows the expected baseline (red triangles).*

The difference in the thermophoretic concentration signal between unbound hIFN-γ (depletion: 2.14%) and the bound complex (depletion: 4.24%) was 2.1% which allows to resolve the binding affinity in detail (Figure 8A). The data revealed a dissociation constant of $K_D = 10 \pm 2$ nM. For comparison, the expected binding behavior for $K_D = 1$ nM and $K_D = 30$ nM is also plotted in Figure 8A.

An example which demonstrates that the amplitude of the binding reaction also carries information about the interaction was found when investigating the binding between a green fluorescent protein (GFP) and a small antibody fragment known as GFP-binding protein (GBP) (38) shown in Figure 8B. The dissociation coefficient was determined to be $K_D = 2.3 \pm 2.1$ nM with an amplitude of 1.27%. The same interaction was measured with a GBP with a point mutation at the binding site. At position 37 an arginine was replaced by an alanine, which is known to reduce the binding affinity. We not only found a reduced binding affinity of 80 ± 38 nM for the GBP mutant but the depletion also changed from 1.27% to 2.82% for GBP and the GBP mutant (R37A), respectively. This is due to the fact that the thermophoretic amplitude not only depends on the size of the complex but also contains contributions from both charge and structure. By replacing a charged arginine by a structurally different and uncharged alanine, a resulting influence on the complex is very likely and can be observed in the thermophoretic amplitude (39).

To test the sensitivity of thermophoresis as a tool to quantify binding reactions, interactions with very small binding partners were analyzed. Such interactions do not lead to a pronounced change in the size of the molecule and thus are difficult to measure with most techniques used to for interaction analysis (40-42).

An uncharged low molecular weight inhibitor is a typical target which is difficult to address with state-of-the-art techniques. An example for such an interaction is for example the binding of the inhibitor quercetin (0.34 kDa) to the cAMP dependent kinase (PKA, 38 kDa). The affinity measured with thermophoresis (130 ± 35 nM) is in good agreement with literature (43-44). The thermophoretic concentration signal changed from 3.8% for the unbound state to 4.53% for the bound state, showing a 19% relative change upon binding of quercetin (Figure 9A). Since the mass of the bound complex differed by only 1% and charge contributions are unlikely, we attribute the large signal to changes in the hydration shell originating from water molecules that are either displaced in the binding pocket or reorganized when the protein undergoes conformational changes.

An even smaller change in the size occurs upon the binding of Ca^{2+}-ions to calmodulin (CaM, 16.7 kDa) shown in Figure 9B. CaM regulates a multitude of protein targets and is the primary receptor for calcium ions in human cells (45). Upon binding to calcium, CaM undergoes a conformational change, rearranging more than 35 water molecules per CaM (46) which allows regulating a multitude of protein targets. This conformational change and the rearranged water molecules lead to a significant change in the thermophoretic properties. The inferred dissociation constant of 2.8 ± 0.2 µM and a cooperativity of 1.97 ± 0.2 are in good agreement with the reported K_D values for CaM-Ca^{2+} which in the range from 1 to 10 µM (47). The acquired affinity proofed to be a specific binding signal as Mg^{2+}-ions used instead of Ca^{2+}-ions did not show any change in the thermophoretic properties.

This data highlights the application fields of thermophoresis as a tool to analyze binding reactions. Due to its sensitivity to changes in the hydration shell of the particles under investigation almost all kinds of interactions are accessible with thermophoresis. Even the binding of very small binding partners can be analyzed with reasonable signal to noise ratio (snr=5 for Ca^{2+} binding and snr=12.5 for small molecule binding). This demonstrates one of the mayor advantages of the developed technique over surface-based techniques like surface plasmon resonance or quartz crystal microbalances which need a significant change in the molecular mass to detect a binding reaction.

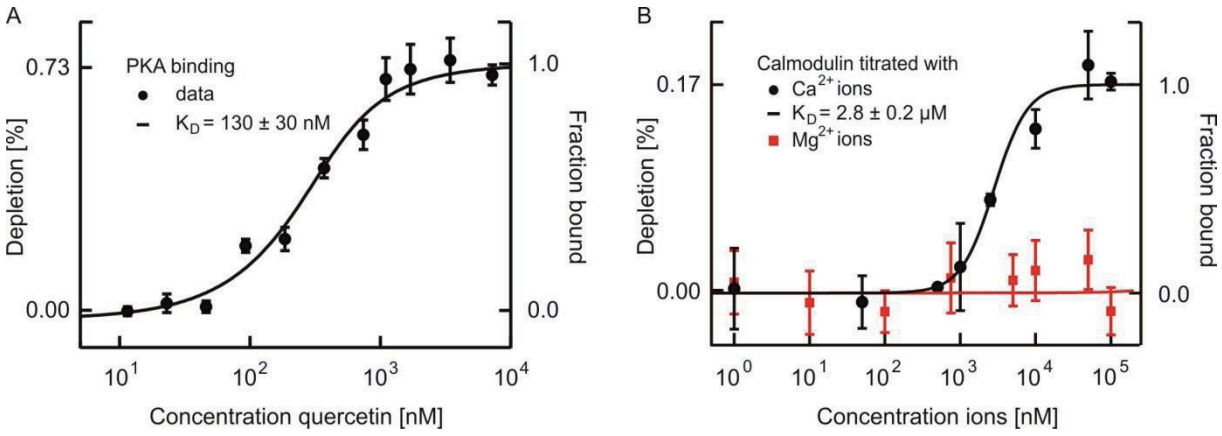

Figure 9 Analysis of the binding of ions and small molecules. *(**a**) The binding of the small, uncharged inhibitor quercetin to the cAMP-dependent kinase PKA is measured with MST. Despite the small changes in the molecule's mass, a signal-to-noise ratio of 12.5 allows an accurate determination of the interaction strength. The determined affinity is in good agreement with reported values. (**b**) Binding of Ca^{2+} ions to fluorescently labeled calmodulin is quantified in PBS buffer. To test for specificity of the interaction, the same titration series was performed with magnesium ions which showed no binding.*

c. Buffer dependence of aptamer binding reactions analyzed with thermophoresis

As thermophoresis is a free-solution analysis method interactions can be measured in various liquids with differing ionic strength and buffer composition. Furthermore, as fluorescence is used as a read-out for our thermophoretic concentration profile interaction analyses are also possible in complex biological liquids like for example human serum or crude cell lysate. By using fluorescent dyes in the red wavelength regime almost no fluorescent background arises from the biological liquid and the measured fluorescence signal only results from the labeled molecules.

As an example the buffer dependence of aptamer binding reactions was analyzed. Aptamers are nucleic acids ligands selected in vitro for their ability to bind to specific molecular targets (48-51). They are promising candidates for diagnostic applications because of their antibody comparable affinity, specificity and the ease with which novel aptamers can be designed (52-57). As model systems, the binding reactions of an aptamer with adenosinemonophosphate (AMP) and adenosinetriphosphate (ATP) were analyzed in different buffers and the binding of the protein thrombin to a different DNA aptamer was quantified in buffers and human serum (Figure 10).

The experiments revealed a high dependence of the binding affinity on the biological matrix (i.e. solution in which the interaction takes place). While the dissociation constant for the aptamer-thrombin binding in selection buffer (K_D=30 nM) is in good agreement with literature (36), the affinity decreases to K_D=190 nM in 1xSSC. In 50% (10%) human serum the binding was best fitted with the Hill equation, yielding an EC_{50}=720 nM (670 nM) and a cooperativity of n=2.

For the aptamer-ATP/AMP interaction a cooperative binding was found which is consistent with the literature (54, 58). Again, the measured affinities in the selection buffer are well within the reported value (54). Measurements in HEPES buffer also confirm these results. Interestingly, in 2x SSC buffer, the EC_{50} values of the ATP/AMP-aptamer binding were both strongly shifted to lower affinities, resulting in an almost 20 times lower EC_{50}.

These shifts in the interaction affinities are in agreement with Cho and Ellington (53), who stated that the aptamer-target binding is strongly depending on the chosen buffer: Binding of the aptamers in the respective selection buffers showed always the highest affinity. For the aptamer-thrombin interaction the shift to lower affinities and enhanced cooperativity in human serum may be due to interactions of the thrombin with blood serum components. For the ATP-aptamer the unexpected big shift to lower affinities in the SSC buffer as compared to the TRIS and HEPES buffers can be attributed to a competing interaction of the strongly negative $Citrate^{3-}$- with the Mg^{2+}-ions as the latter are essential for the aptamer-ATP/AMP binding.

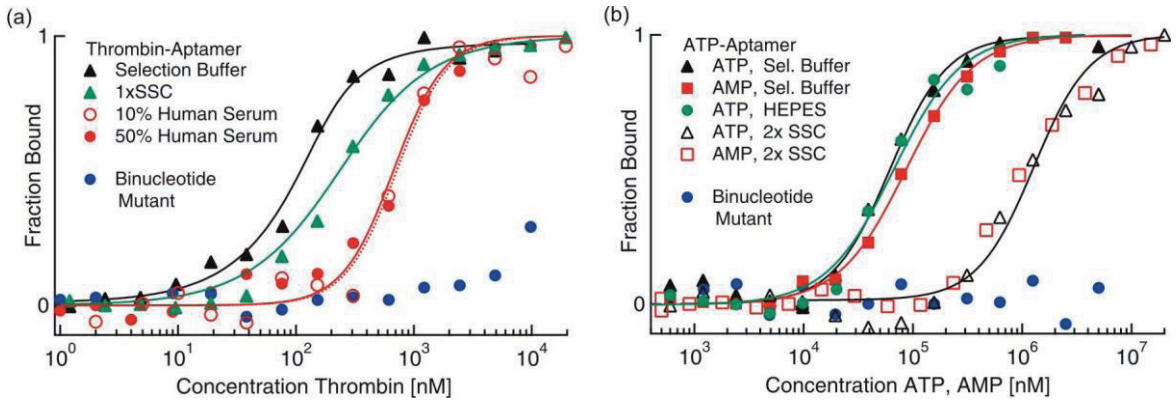

Figure 10. ***Binding curves in various buffers***. ***(a)*** *Aptamer-thrombin binding in selection buffer, SSC and 10% and 50% untreated human serum.* ***(b)*** *Aptamer binding to ATP and AMP in selection buffer, HEPES and 2x SSC. For both ligands, a control experiment with a binucleotide mutant was performed that showed no binding.*

Interestingly, the composition of the matrix did not significantly affect the sensitivity or specificity of the approach, as it is the case with chip based technologies such as surface plasmon resonance (SPR). In all experiments, a high signal-to-noise-ratio (SNR) was achieved, even in 50% human serum. For example the binding of AMP with a molecular weight of only 347Da showed a SNR=93 in selection buffer and SNR=23 was found for thrombin-binding in 50% human serum. To test for the specificity of the thermophoresis signal control experiments were performed with DNA strands including point mutations to prevent the correct folding of the binding site of the aptamers.

d. Effects of competitive interactions in serum

Today, most protein interactions are measured with analysis tools that need special artificial buffer systems to interrogate binding affinities as components present in the original biological liquid may disturb the signal. But these additional components may have a strong influence on the interaction under investigation and thus the results measured in artificial buffer systems may lead to wrong decisions when developing drug candidates.

Using a red fluorescent dye, the auto-fluorescence of serum or cell lysate components are negligible and the measured fluorescence signal is only due to the labeled protein. Hence, the measured thermophoresis signal only results from the protein and any change in thermophoretic parameters reports a change in the protein. This allows investigating the effects of biological liquids on interaction strengths and provides precise information about the binding behavior inside the human body.

The experiments revealed that for example the binding of hIFN-γ to a specific Anti-IFN-γ antibody dramatically shifts to lower affinities when the interaction is probed in cell extracts instead of a buffer system like PBS buffer (Figure 11A). Reasons for such a shift in binding strength can be differences in viscosity, pH or ionic strength (59) or also competitive interactions of one binding partner with components of the matrix. Such competitive interactions can have a strong effect on the apparent interaction strength especially if the competitive binder is present in the biological matrix at high concentrations. Especially in the field of drug development this information is of great importance as one can test for possible side reactions in an *in-vitro* assay and can thus gather information about the necessary dose of a drug to be effective in the human body.

Low molecular weight binders (or small molecules) are likely candidates for new drugs and such binders make up a strong field in pharmaceutical research. When performing a

thermophoretic binding analysis of quercetin with the kinase PKA in human serum predictions about its applicability as a drug can be made. The experiments were performed in 5% and 30% human serum (Figure 11B). The resulting apparent dissociation constants were determined to be $K_D = 6 \pm 0.4$ µM and $K_D = 50 \pm 7$ µM, respectively (Figure 4B) which is a factor of 46 (5% human serum) and 384 (30% human serum) weaker in affinity compared to the measured value in HEPES buffer. Such a strong shift in affinity is most likely due to a competitive interaction with a serum component. Therefore the effect of the most abundant blood protein, human serum albumin (HSA), on the binding of quercetin to PKA was analyzed. With its hydrophobic binding pockets, this protein is a universal transport protein for a wide range of molecules and is known to bind, amongst others, to flavonoids like quercetin (60).

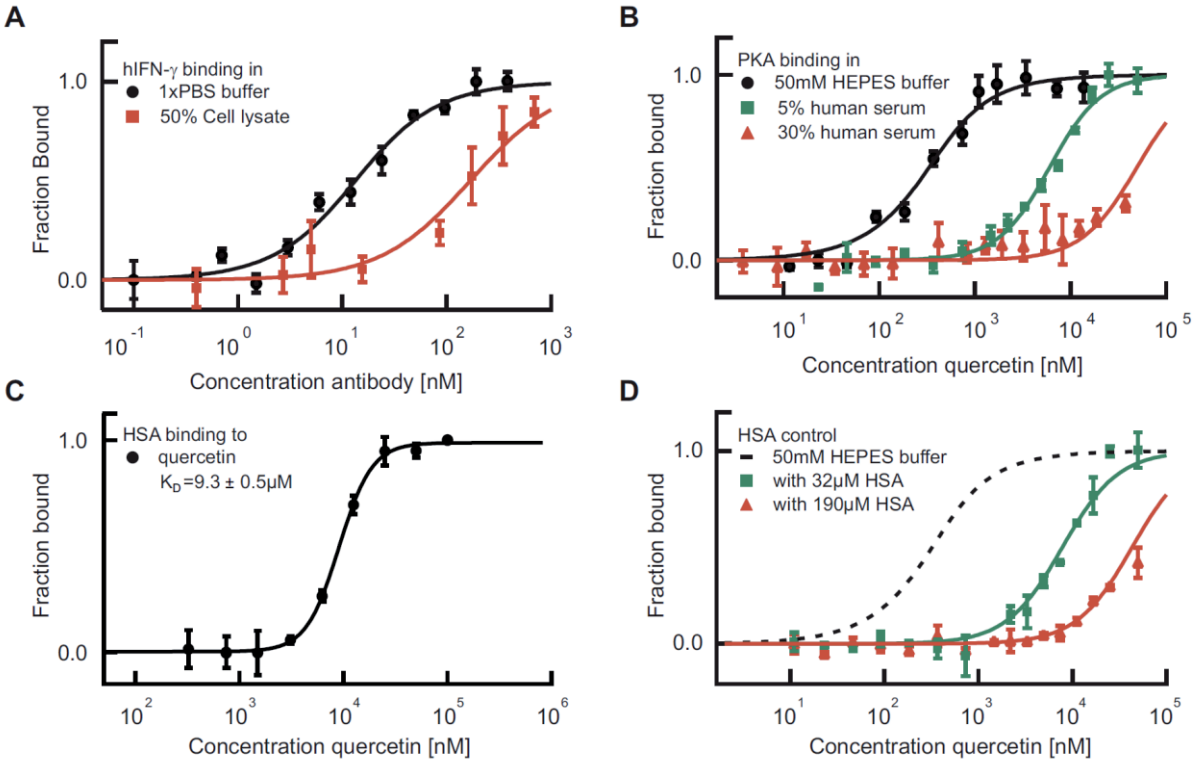

Figure 11 Thermophoretic analysis of interactions in biological liquids. *(**a**) The interaction of hIFN-γ with a specific antibody is analyzed in buffer and compared with the same interaction in crude E. coli cell lysate. In lysate the binding strength shifts towards lower affinities. (**b**) The binding of the inhibitor quercetin to the cAMP-dependent kinase PKA is analyzed in human serum and a strong dependence on the amount of serum is found. (**c**) The shift in affinity results from an interaction of quercetin with the blood protein HSA. (**d**) By adding HSA in concentrations corresponding to human serum the observed shifts can be mimicked.*

An adsorption of quercetin to HSA would dramatically reduce the free concentration of the small molecule available for a binding to PKA. This would lead to a shift of the apparent binding constant towards lower affinities. To confirm the binding of quercetin to HSA a thermophoretic experiment was performed which yielded a dissociation coefficient of 9.3 ± 0.5 μM and is in good agreement with literature values (60) (Figure 11C). Hence, human serum albumin is likely to influence the apparent affinity of PKA for quercetin in human serum.

To reproduce the strong shift in the binding strength of PKA to quercetin in human serum a PKA-quercetin binding experiment in 50 mM HEPES buffer was performed with HSA concentrations corresponding to 5% and 30% human serum (Figure 11D). With these artificial systems a similar shift in the apparent affinity of the PKA-quercetin interaction was observed which differed only by about 20% from those obtained in serum. Since in the artificial buffer systems the buffer, ionic strength and viscosity were constant at all concentration of quercetin, the reduced apparent affinity in serum seems to be a result of the binding of quercetin to human serum albumin.

e. Interactions of membrane proteins using intrinsic protein fluorescence

Membrane proteins play an important role in many cell functions; they work as ion channels or transport proteins to maintain cell functionality and are essential for signal transduction processes. Especially G protein coupled receptors (GPCR) are an important group of such membrane proteins as they are target of many modern drugs. Despite their importance, a detailed investigation is quite difficult due to bottlenecks when producing sufficiently large amounts of such proteins. To overcome many of these bottlenecks short peptide surfactants were used to stabilize diverse membrane proteins. But even highly related proteins may react differently to the same detergent. This sensitivity of the soluble proteins also renders an interaction analysis with state of the art analysis technologies impossible. The use of surface-based sensors is very laborious as the protein not only needs to be stable in solution but also needs to survive the surface coupling without aggregation and with correct biological function. Even the attachment of fluorescent dyes to such membrane proteins remains very difficult and the surfactants used for unlabeled membrane proteins may not be the right choice for the tagged one. Furthermore, promising drug candidates that target membrane proteins are often low molecular weight binders. As result, surface-based techniques that rely on a change in molecular weight or diffusion coefficient based techniques like FCS run into trouble when analyzing such interactions of small molecules with relatively large membrane proteins.

The thermophoretic method showed to be suitable for an analysis of such small molecule interactions and thus seems to be a promising tool to investigate the binding properties of membrane proteins. To overcome the problem of tagging the sensitive proteins with a fluorescent dye it was necessary to develop an alternative read-out for monitoring the concentration change inside the temperature gradient. This is achieved by using the intrinsic fluorescence of aromatic amino acids like phenylalanine, tyrosine and tryptophan. The amino acids absorb light in the UV range around 260nm to 290nm and emit light spectrally shifted to the red. Thus, they act like a fluorophor. The brightest of these intrinsic dyes is tryptophan with an absorption maximum around 280nm and a broad emission above 310nm. For this wavelength UV-LEDs exist that provide sufficient light intensities and fair diode lifetimes. To enhance the sensitivity of the fluorescence detection the typically used CCD camera was exchanged by a photomultiplier tube (PMT). The PMT allows counting incoming photons and is particularly sensitive in the blue and ultraviolet wavelength regime.

The aromatic amino acids are relatively rare amino acids meaning that not all proteins are accessible with the UV fluorescence approach. Still, typical proteins contain 100-300 amino acids resulting in at least one or two intrinsic fluorophores in most proteins. However, this is somehow the bottleneck of intrinsic fluorescence as a read out: Only if just one binding partner contains an intrinsic dye the thermophoresis signal can be analyzed without complex correction algorithms. Fortunately, most small molecules do not contain aromatic amino acids making thermophoresis combined with UV fluorescence a perfect suit for analyzing and screening protein-small-molecule interactions.

The feasibility was shown by analyzing purified GPCRs and their ability to bind to their ligands. The ligands were odorants of less than 300Da in molecular weight while the receptors were larger than 300kDa. With thermophoresis the binding of mOR103-15 receptor to its ligand heptanal was analyzed resulting in a half maximal effective concentration (EC_{50}) of 900nM. A control using boiled and therefore denatured mOR103-15 receptor showed no binding (Figure 12).

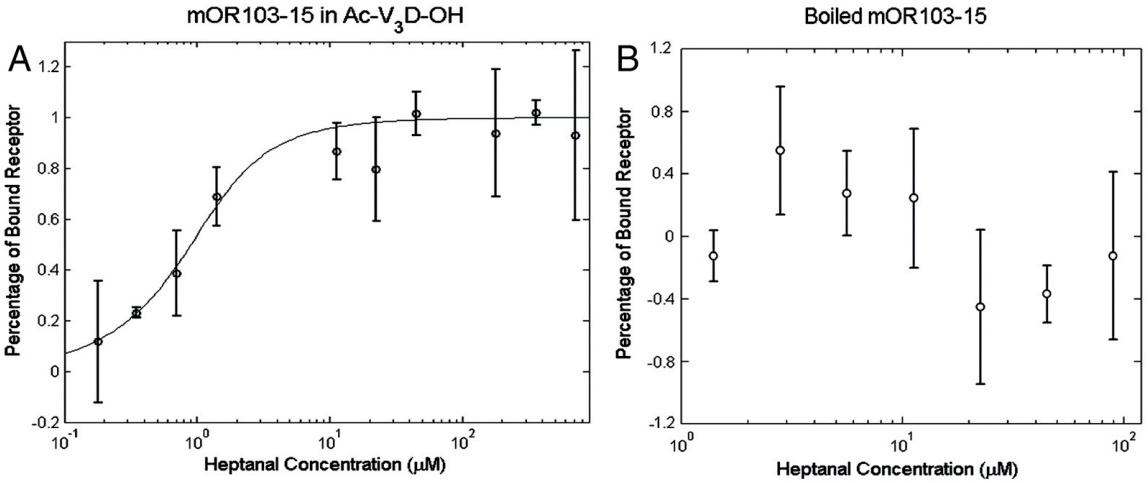

Figure 12 Thermophoretic binding analysis using intrinsic protein fluorescence. (a) *The GPCR mOR103-15 binds to its ligand heptanal, a small molecule of 114 Da in molecular weight. The data yields an EC_{50} of 900nM.* ***(b)*** *A control experiment using boiled receptors showed no binding signal indicating that the binding observed in (A) is not due to the unspecific interaction with the surfactant or the denatured receptor.*

f. Conclusions

The experiments showed that thermophoresis is a suitable tool to analyze various kinds of binding reactions. Due to its sensitivity to the hydration sphere also very small changes are detectable like for example the binding of uncharged small molecules or even single ions. In contrast to other techniques the sensitivity of the measurement does not depend on the size ratio of the two binding partners and interactions between two proteins of approximately the same molecular weight can be analyzed with the same sensitivity as interactions with small molecules, or even ions. This is of importance as both protein-protein affinities and low molecular weight binders are topics in current basic and pharmaceutical research.

The use of a fluorescence label also allows determining binding affinities directly in biological liquids such as blood serum or crude cell extract. This enables a determination of affinities of unpurified, expressed antibodies directly in the supernatant of a cell suspension, opening novel ways for fast antibody selection. It furthermore allows a quantification of binding reaction near *in vivo* conditions showing potential side reactions and providing insights into dose response relations. This is of great importance as such

information is typically obtained through clinical studies involving intense efforts and the risk of possible harm for the volunteers.

On the other hand, if the fluorescence label is suspected to influence the binding properties the usage of intrinsic tryptophan fluorescence provides the means for a label-free free-solution binding analysis tool. This is however limited to analyses in artificial buffer systems as biological fluids typically contain many components with a fluorescence in the UV regime.

As only microliter volumes are necessary to conduct the measurements valuable samples can be saved. The usage of a simple Mix&Read protocol simplifies preparations and the possibilities of mistakes during the preparation are reduced. The entirely optical method is contact-free and therefore a contamination of the sample is minimized. It further measures the interaction in free-solution and no surfaces can disturb the interactions. In solution the binding partners can move and rotate in all dimensions and are not limited by any surfaces.

This is the case for today's most widespread interaction analysis tools which us for example Surface Plasmon Resonance (SPR) to monitor binding reactions (61, 62). This technique requires the immobilization of one binding partner on a sensor surface, raising issues of steric hindrance or molecular activity. These surface based methods are very sensitive in detecting minimal changes in the mass of sensor, but high affinity interactions are often not accessible for measure due to mass transport effects and transient binders are in most cases difficult to quantify (40).

Other free-solution technologies like fluorescence correlation spectroscopy (FCS) (41), back-scattering interferometry (BSI) (63-65) and isothermal titration calorimetry (ITC) (66) do not suffer from such surface effects but have other limitations. FCS relies on a significant change in the diffusion constant upon binding and is only applicable to a limited number of biomolecular interactions (41). BSI and ITC are label-free technologies and do not need a label or surface coupling. Still ITC, for example, can conduct measurements at a relatively low throughput and with exceptionally high sample consumption. BSI typically suffers from a refractive index background arising from non-reacted ligand, particularly at high concentrations. In addition, temperature-induced changes of the refractive index may interfere with the binding signal and render the interpretation difficult.

The presented results suggest that thermophoresis is suitable for the quantification of a broad range of biomolecules. Still additional work is required to understand the intricacies of thermophoresis in more detail. Especially exact relations between the amplitude of the thermophoresis signal and changes of the protein conformation or in its hydration shell (e.g. release of water molecules from binding sites) need further clarification. With deeper understanding of such dependencies the amplitude could give additional information on the binding location of the small molecule and, for example, detect if a binding occurs deep inside a hydrophobic binding pocket or at the protein's surface.

VI. Melting studies with Thermophoresis

Measuring the stability of biomolecules and especially of DNA is of great importance in the field of biology, medical diagnostics and biotechnology. Typically it is inferred in a thermal denaturation experiment where molecules are thermally destroyed and the response of a physical property is monitored during this process. This directly provides information about the DNA sequence or the biomolecular structure.

The read-out signal for such melting curve experiments, mostly fluorescence or UV absorbance, is continuously collected while scanning the sample through a range of temperature (67-70). Traditionally, such methods consume considerable amounts of molecules as they use large cuvettes as a sample compartment. Therefore, fluorescence approaches have gained momentum and allow reducing volume and concentration in such experiments (29, 71-73). Fluorescence melting analysis usually is performed using intercalating fluorescent dyes, which fluoresce strongly in the presence of double-stranded DNA and show a considerable decreased fluorescence without double stranded DNA. The most familiar of these is ethidium bromide, but asymmetric cyanine dyes, such as SYBR Green I are even brighter and are dyes of choice in fluorescence melting analysis and real-time PCR. For protein melting curves, fluorescent dyes like SYPRO Orange are applied which bind to the hydrophobic regions of a protein and increase their fluorescence upon binding. When a protein unfolds more hydrophobic region become accessible for the dye and the fluorescence increases. A major drawback of this technique is that the intercalating dye may affect the stability of the protein.

As thermophoresis also monitors surfaces properties of molecules it is possible to use this effect as a read-out for a melting curve analysis. Especially, the high sensitivity even to minute changes in the molecules surface will allow for a very detailed melting profile and provide deeper insight into the mechanisms upon unfolding.

a. Thermophoretic DNA melting curves

As model systems for thermophoretic melting curve analysis nucleic acids where chosen as they can be tailor-made with multiple mutations or molecular variations. Furthermore, there are good theoretical models which allow a prediction of the stability based on nearest-neighbor-thermodynamics. The analysis of various kinds of DNA molecules allow to demonstrate the high sensitivity of thermophoresis as a tool for melting curve analysis.

The temperature dependence of the Soret effect shows a characteristic dependence which was found by Piazza et al. (74). They measured the thermophoretic properties of various biomolecules, which is described well with an empirical fitting function:

$$S_{T,i}(T) = S_{T,i}^{\infty}\left[1 - \exp\left(\frac{T^* - T}{T_{0,i}}\right)\right]. \qquad (6)$$

In this equation S_T represents the thermophoretic limit for high temperatures T, T^* is the temperature where S_T switches its sign and T_0 is a rate of exponential growth that embodies the strength of the temperature effect. This high temperature limit of the Soret coefficient is like the Soret coefficient S_T at room temperature a unique characteristic for molecules and therefore also differs for double- and single-stranded molecules. This is reflected in the index i.

To allow a precise analysis of the melting temperature all thermophoretic melting curves are corrected for a standard temperature dependence as described in eq. 6. This reduces the signal to transitions which deviate from the standard temperature dependence and allows monitoring changes in the molecular structure. Presenting the data in the thermophoretic limit for high temperatures S_T^{∞} provides information about the thermophoretic properties of a molecule like the molecular size and conformation and can be used to distinguish different kinds of molecules.

This $S_{T,i}^{\infty}$ is constant for each conformational state $i = \{ss, ds\}$ of the nucleic acid and due to the linearity of thermophoretic depletion, the experimentally measured apparent S_T^{∞} is a linear superposition of the closed and melted state, showing a transition from $S_{T,ds}^{\infty}$ to $S_{T,ss}^{\infty}$ given by:

$$S_T^{\infty}(x) = x \cdot S_{T,ss}^{\infty} + (1-x) S_{T,ds}^{\infty}. \qquad (7)$$

The parameter x represents the fraction of molecules in the single-stranded state. $S_{T,ss}^{\infty}$ is the high temperature limit S_T^{∞} for single-stranded DNA, $S_{T,ds}^{\infty}$ for double-stranded DNA. The melting temperature T_m represents the temperature at which x x=0.5 holds (75).

For most melting experiments the melting process is interpreted as a two state process between an open and denatured state of the molecule. Such an interpretation ignores intermediate states (e.g. due to the unfolding of tertiary structures) but still is a good approximation for many DNA melting curves. Nevertheless, eq. 7 can also be expanded to a more complex unfolding behavior by introducing an additional intermediate state.

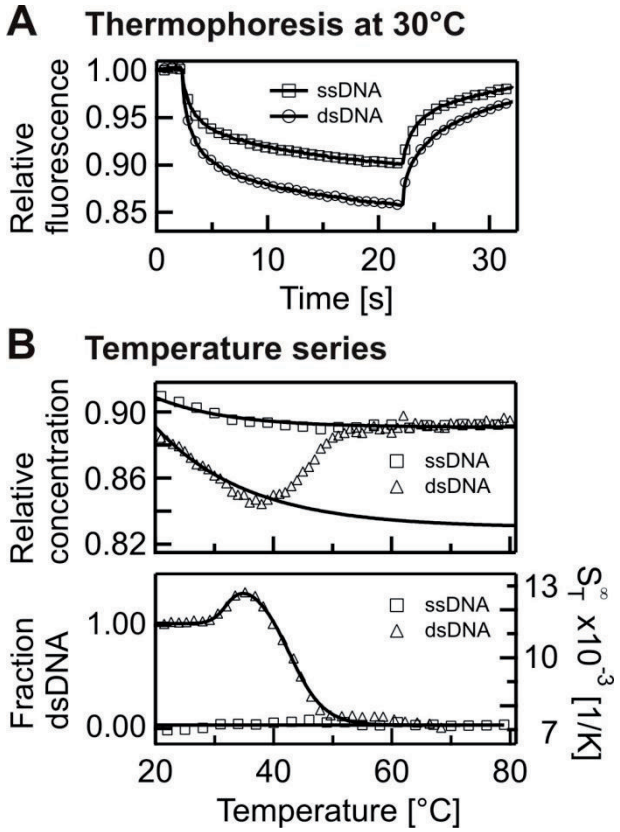

Figure 13 Thermophoretic melting curve assays. (a) *Single- and double-stranded DNA show different time series of the normalized fluorescence in the heated laser spot which is then converted to a relative concentration value.* ***(b)*** *When repeated for different temperatures, single-stranded DNA (ssDNA) as well as double-stranded DNA (dsDNA) shows a pronounced temperature dependence, which was fitted using eq. 6. Correcting the data for this temperature dependence, a typical DNA melting curve appears.*

Figure 13 shows the recording of a thermophoretic melting curve. The overall sample temperature is increased stepwise typically between 15°C and 95°C depending on the expected thermal transitions of the sample. At every temperature the Soret coefficient is analyzed (Figure 13A). The Soret coefficient is then plotted over the sample temperature yielding a distinct melting profile for the sample molecule (Figure 13B, top). To obtain the exact melting profile the additional heating by the IR laser must also be taken into account. By correcting this temperature series with the temperature dependence of the Soret coefficient according to eq. 6 a melting profile of the high temperature limit S_T^{∞} (Figure 13B, bottom) is obtained. From this the stability of the molecule can be derived and also possible additional intermediate states are observable.

In the following various nucleic acids are analyzed to demonstrate the limits and advantages of thermophoresis as a tool to quantify the stability of biomolecules. Control

experiments were performed with UV absorbance and calculations on the basis of a nearest neighbor thermodynamics were used to estimate the melting temperatures (76-79).

In Figure 14 a variety of melting experiments is shown demonstrating that thermophoresis is potent read-out technique to monitor melting transitions. The experiments show that most standard melting applications are accessible with thermophoresis (Figure 14). A

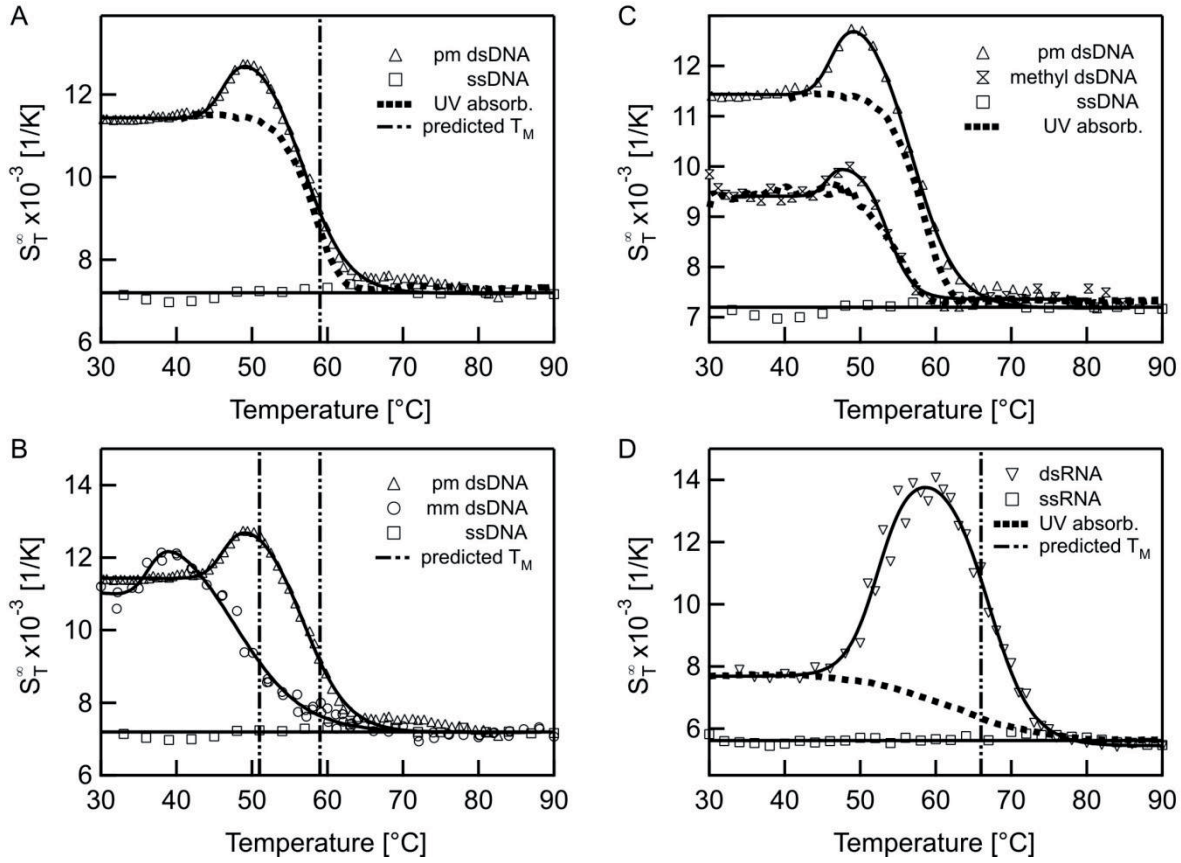

Figure 14 Nucleic Acids melting curves. ***(a)*** *The melting of a 22 bp long DNA oligonucleotide was analyzed with thermophoresis and UV absorbance and compared to thermodynamic calculations.* ***(b)*** *DNA containing a single base mismatch was compared to perfectly matching DNA. The mismatch showed a changed melting temperature Tm due to the lower thermal stability by the base mismatch.* ***(c)*** *The effect of methylated bases on the stability of DNA was analyzed with thermophoresis and compared to UV absorbance. Besides monitoring the melting of the two strands, the Soret coefficient at low temperatures showed a significant reduction in the thermophoretic amplitude resulting from the modified bases.* ***(d)*** *The melting of RNA showed a strong change in* S_T^∞ *before the actual melting occurs. This increase in* S_T^∞ *prior to melting for dsRNA was attributed to a partial melting of the double strand beginning at the ends of the RNA duplex. It was significantly larger for RNA as compared to DNA.*

single mismatch in a 22bp duplex can be easily distinguished from a perfectly matching duplex (Figure 14B) and the thermophoresis signal is highly sensitive to any change at the molecule. For example the methylation of adenosines in a 22bp strand leads to a strong difference in S_T^{∞} compared to normal DNA at low temperatures (Figure 14C). But even such small changes like a single mismatch have an effect on the Soret coefficient as DNA containing a single mismatch, for example, was found to have a 0.4×10^{-3} 1/K lower S_T^{∞} at low temperatures compared to perfectly matching DNA. Moreover, RNA molecules can be measured with the same accuracy as DNA molecules (Figure 14D). All control experiments - theoretically predicted melting temperatures and UV absorbance spectroscopy- yielded melting temperatures which are in very good agreement with the thermophoretic melting profiles.

The additional melting transitions observed in the thermophoresis signal were investigated in more detail. It seemed that they are a general process in the melting procedure like a partial unfolding of the duplex at the two ends (Figure 15A). The hypothesis was tested with DNA strands with dangling ends added to both sides of the duplex. Such modification should increase the thermophoretic amplitude as the surface of the DNA strand increases upon unfolding. Thermophoretic melting experiments were performed with dangling ends of varying composition and also for different duplex sequences (Figure 15B-C). It turned out that with increasing length of the dangling ends the amplitude of the first transition increased as it was expected from the partial unfolding hypothesis. Furthermore, it could be shown that the duplex sequence has no influence on the amplitude of the initial transition whereby tertiary structures of the duplex part could be ruled out. Last, the initial transition was also present for dangling ends of various compositions which demonstrated that the change in the Soret coefficient was not due to an internal structure of the dangling ends. It turned out that the initial transition was present in all duplex melting experiments giving further hints that the effect might be a general part of the unfolding process of double stranded DNA.

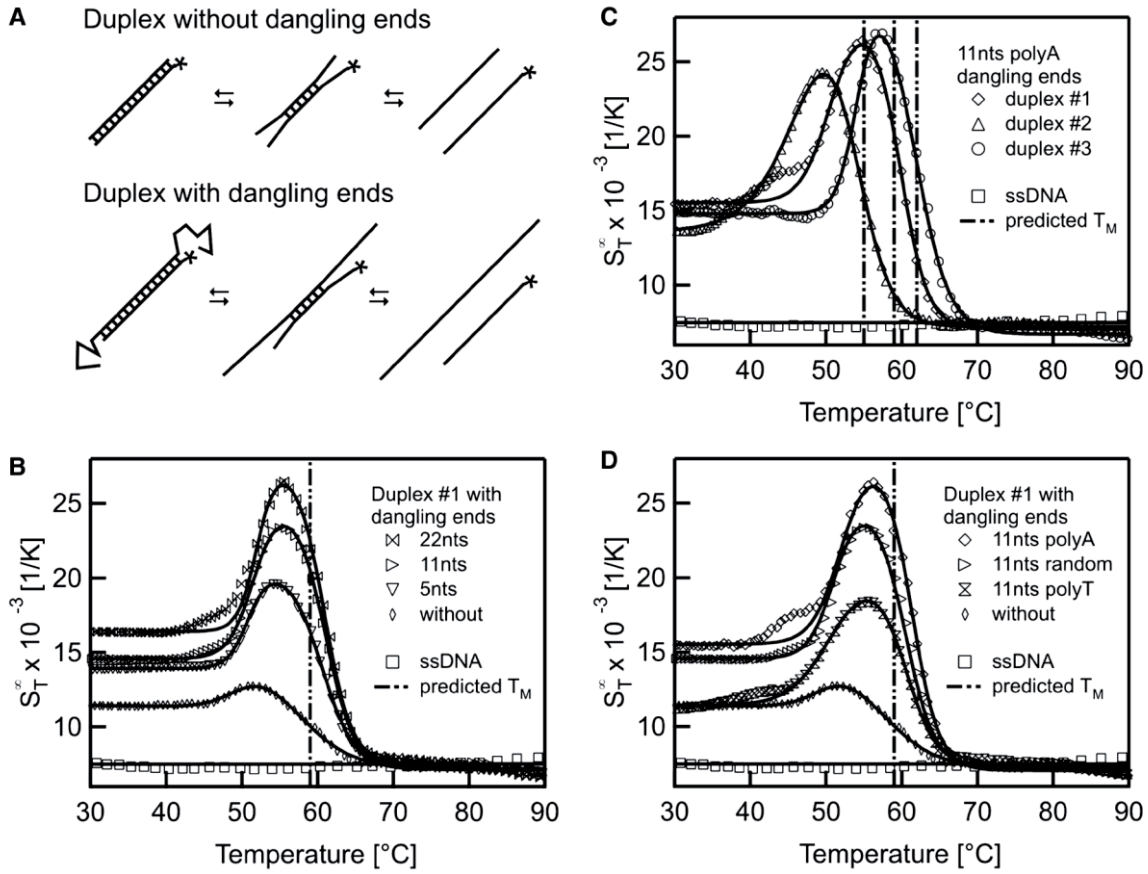

Figure 15 Effects of dangling ends. *The melting of DNA double strands with dangling ends was analyzed with thermophoresis.* ***(a)*** *As a hypothesis for the transition before the actual melting of the two DNA strands we propose an unbinding of the duplex-ends in a pre-melting transition. This 'end effects' should increase when adding overlapping DNA strands to both sides of one duplex strand.* ***(b)*** *The data for dangling ends of various lengths showed an increase of the Soret coefficient due to a change in the conformation before the actual melting transition. The final melting temperature matches the situation without dangling ends.* ***(c)*** *When changing the composition of the duplex forming sequence a shift in the melting temperature but also in the first transition was observed.* ***(d)*** *To rule out any potential structures of the dangling ends, duplex #1 was analyzed with 11 nt overhangs of random sequence and compared to dangling ends with polyA and polyT sequence. Irrespective of the dangling ends, the melting temperature remained constant.*

But the thermophoretic melting experiments are not limited to double stranded nucleic acids. Also purely tertiary structures like hairpin structures can be analyzed with thermophoresis. As an example the melting of a DNA hairpin forming a 6-7 bp double-stranded stem is measured. Here, again an initial transition before the actual unfolding into a single stranded structure is observed (Figure 16A). With UV absorbance measurements this transition is not accessible.

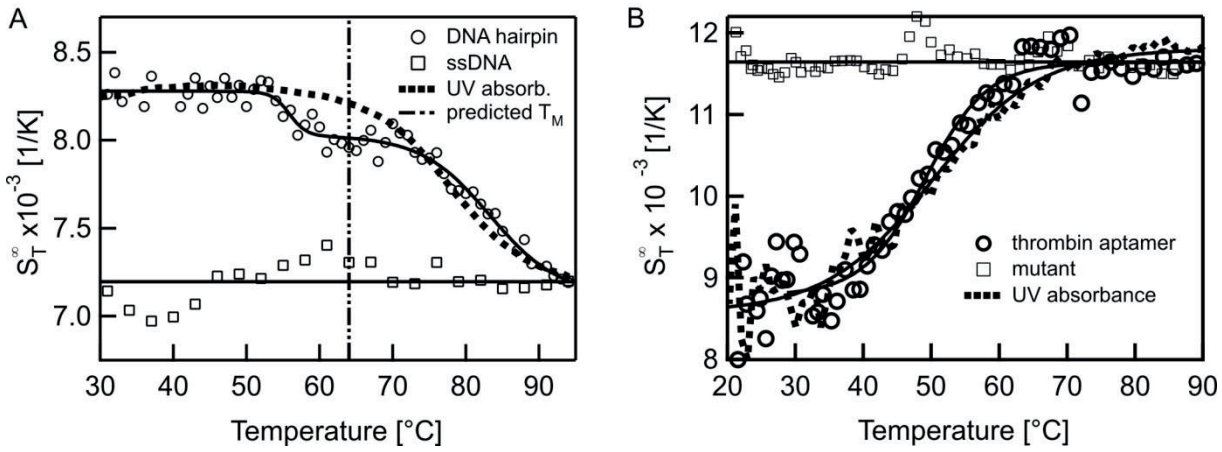

Figure 16 Structural information of DNA molecules. (a) *The change in conformation of a DNA hairpin was resolved by evaluating its thermophoretic behavior with temperature. We found a distinct deviation from a two-state behavior, attributed to a breakage or re-orientation of the duplex structure.* ***(b)*** *As an example for a pure conformational melting signal, a DNA aptamer which is known to form a G-quadruplex was analyzed with thermophoresis. It showed a clear transition without deviations from a two-state model.*

A tertiary structure without any double stranded sequence was investigated by analyzing a G-quadruplex structure formed by a single-stranded DNA molecule (Figure ***16***B) (80). The observed increase in the Soret coefficient could be expected as the DNA molecule forms in its G-quadruplex structure a more compact structure compared to the unfolded single strand and this increase in surface upon unfolding leads to a strong signal in the melting profile. Although in above cases no unbinding of a second molecule (e.g. the complementary DNA strand) and thus no change in mass or charge occurs the change in the thermophoretic properties is large enough to monitor the unfolding process with thermophoresis. This might be attributed to the sensitivity of the thermophoretic movement on changes in the surface area and hydrophobicity of molecules.

b. Conclusions

Thermophoresis showed to be a sensitive method for the analysis of the thermal stability of nucleic acids. Beside the standard melting temperature T_m, the data showed that additional information about conformational states is accessible. Such conformational information and the possibility to find potential tertiary motifs of nucleic acid are especially important for RNA, where functionality highly relies on the structure. With this thermophoresis may also help in the investigation of complex structures of nucleic acids and provide more detailed information about the molecular processes.

Due to low sample volumes per measurement at nanomolar concentrations expensive or rare samples can be used sparingly. Furthermore, no FRET pairs are necessary reducing the cost and complexity of mutation-specific analysis. The possibility to freely choose the buffer conditions of the experiment will also help to provide information closer to the *in vitro* situation. This would allow for example to test the thermal stability of biomolecules in biological liquids providing insights into interactions of partly denatured molecules with components of the biological matrix.

Recently, Mast et al. showed that the thermophoretic analysis of DNA is possible using intercalating fluorophores and that thermophoresis can be employed to quantify the length of PCR products (81). This indicates that also a thermophoretic thermal stability analysis is possible using intercalating dyes which would further decrease the costs and complexity of a melting experiment. Such an approach would combine a typical fluorescence melting curve with the advantage of thermophoresis to monitor the unfolding of tertiary structures.

In the presented experiments it could be shown that thermophoresis with its capability to resolve complex melting behaviors can provide more detailed insights into the interactions of nucleic acids. And furthermore, its sensitivity for conformational states thermophoresis provides a promising experimental approach for testing biological models and allows for a more detailed understanding of the melting behavior of biologically relevant nucleic acids.

VII. Outlook

The experiments presented in this thesis cover a broad variety of different applications of the fluorescence- and capillary-based thermophoresis setup. This setup allows gaining insight into the basic principles of thermophoresis; it is applicable to measure binding affinities of many different biomolecules and reveals information about the thermal stability of molecules. Still, all fields need further investigation to achieve a better understanding of the physical principles and to extend the applicability of the technique.

A better understanding of thermophoresis and of the influences of molecular properties is strongly needed. Though the theory presented inhere describes the movement of particles with a size larger than the Debye length very well, extensions of the theory to sizes comparable and smaller than Debye length are still sought after. Furthermore, extending the theoretical description to a radial capacitor model to describe the effect of ionic shielding should improve the correctness compared to the currently used plate condenser model. Also more information about the entropy of hydration and hydrophobic and hydrophilic effects is still needed. Especially in the case of interaction studies such details would allow deeper insights in molecular processes and, given a precise molecular dynamics calculation, would allow correlating the signal strength with binding to specific sites of the protein.

The label-free binding studies with thermophoresis demonstrate that it is possible to quantify protein interactions without an additional fluorescent dye. Still the experimental setup needs further improvement to enhance the reproducibility of the measurements. Here, especially the stability of the UV LED used to excite the protein fluorescence has the potential to increase the signal to noise ratio of the measurements. A further crucial point of the label-free approach is the search for feasible glass capillaries. Typically used borosilicate glass absorbs light below 300nm and thus cannot be used for acquiring tryptophan fluorescence. Therefore, capillaries have to be made of synthetic glass or quartz glass to provide sufficient optical transparency. Such capillaries are usually wrapped with a polyamide coating which has to be removed before usage. This process is currently done with an open flame and can lead to inhomogeneities in the capillary. Also residues from burned coating may disturb the measurements. Here, a better procedure or a new provider has to be found to further enhance the method's reproducibility. Moreover, the label-free approach so far needs very clean samples with only one binding partner fluorescent in the UV regime which constrains the applicability of the approach. Still, a determination of binding affinities should be possible even if both binding partners affect

the fluorescence. This would need a correction of the thermophoresis signal for the signal caused by the second binding partner.

Regarding the thermophoretic melting curve analysis it was shown that standard DNA and RNA melting experiments can be easily performed using thermophoresis. Even conformational changes like unfolding of a G-quadruplex or partial unfolding at the ends of DNA double strands were accessible with thermophoresis. Now this sensitivity can be combined with the usage of intrinsic protein fluorescence. This combination gives a new tool to study the thermal stability of proteins and to provide insights into the thermal unfolding behavior of biomolecules. Such experiments are typically performed using fluorescent dyes which bind to hydrophobic sites of the protein, but these dyes may have an influence on the stability of proteins and thus distort the melting profiles. Another possibility to quantify the thermal stability of proteins is differential scanning calorimetry (DSC). Calorimetry measures the change in heat capacity upon unfolding but requires large amounts of sample to monitor the slight changes during denaturing. Applying thermophoresis to monitor protein denaturing would allow to use little amounts of sample while still acquiring the melting profile with high sensitivity.

Furthermore, using the Soret coefficient as a read-out may help to provide direct access to thermodynamic parameters as it is the case for DSC. Using the thermodynamical description of thermophoresis relates the Soret coefficient to the entropy of the particle-solvent system and thus could be transferred into a heat capacity. This heat capacity should be related to the heat capacity measured with calorimetry and label-free thermophoresis measurements could work as some kind of “Optical DSC”.

To conclude, thermophoresis is a highly sensitive tool to analyze biomolecules and changes of molecular properties. It can be used for a broad range of applications in biotechnology and may aid in the complete chain of drug development. The fields of application range from screening projects for the identification of new potential drug candidates to high content interaction analyses which provide detailed information about the binding properties and possible influences of the biological matrix.

VIII. References

1. Ludwig, C. (1856) Diffusion zwischen ungleich erwärmten Orten gleich zusammengesetzter Lösungen. *Sitzungsber. Akad. Wiss. Wien: Math.-Naturwiss.*, **20**, 539.
2. Clusius,K. and Dickel,G. (1938) Neues Verfahren zur Gasentmischung und Isotopentrennung. *Naturwissenschaften*, **26**, 546.
3. Debye,P. (1939) Zur Theorie des Clusiusschen Trennverfahrens. *Annalen der Physik*, **36**, 284–294.
4. Baaske,P., Weinert,F.M., Duhr,S., Lemke,K.H., Russell,M.J. and Braun,D. (2007) Extreme Accumulation of Nucleotides in Simulated Hydrothermal Pore Systems. *Proc. Nat. Acad. Sci. USA*, **104**, 9346–9351.
5. Braun,D. and Libchaber,A. (2002) Trapping of DNA by Thermophoretic Depletion and Convection. *Phys. Rev. Lett.*, **89**, 188103.
6. Iacopini,S. and Piazza,R. (2003) Thermophoresis in protein solutions. *Europhys. Lett.*, **63**, 247-253.
7. Duhr,S. and Braun,D. (2006) Why molecules move along a temperature gradient. *Proc. Nat. Acad Sci. USA*, **103**, 19678–19682.
8. Rauch, J. & Köhler, W. (2002) Diffusion and thermal diffusion of semidilute to concentrated solutions of polystyrene in toluene in the vicinity of the glass transition. *Phys. Rev. Lett.*, **88**, 185901.
9. Wiegand, S. & Köhler, W. Thermal Nonequilibrium Phenomena in Fluid Mixtures (Springer, Berlin, 2002)
10. Piazza, R., Iacopini, S., Triulzi, B. (2004) Thermophoresis as a probe of particle-solvent interactions: The case of protein solutions. *Phys. Chem. Chem. Phys.*, **6**, 1616-1622.
11. Würger, A. (2007) Thermophoresis in Colloidal Suspensions Driven by Marangoni Forces, *Phys. Rev. Lett.*, **98**, 138301.
12. Dhont,J.K.G. (2004) Thermodiffusion of interacting colloids. I. A statistical thermodynamics approach, *J. Chem. Phys.*, **120**, 1632.
13. Dhont,J.K.G. (2004) Thermodiffusion of interacting colloids. II. A microscopic approach, *J. of Chem. Phys.*, **120**, 1642.
14. Dhont,J.K.G., Wiegand,S., Duhr,S. and Braun,D. (2007) Thermodiffusion of Charged Colloids: Single-Particle Diffusion. *Langmuir*, **23**, 1674-1683.

15. Wiegand, S. und W. Köhler, Measurement of Transport Coefficients by an optical grating technique, in Thermal Nonequilibrium Phenomena in *Fluid Mixtures*, Springer: Berlin, 2002, S. 189-210.
16. Köhler, W. (1993) Thermodiffusion in Polymer-Solutions as Observed by Forced Rayleigh-Scattering. *J. Chem. Phys.*, **98**, 660-668.
17. Rusconi, R., L. Isa, und R. Piazza (2004) Thermal-lensing measure ment of particle thermophoresis in aqueous dispersions. *J. Opt. Soc. Am. B*, **21**, 605-616.
18. Duhr,S. and Braun,D. (2006) Thermophoretic Depletion Follows Boltzmann Distribution, *Phys. Rev. Lett.*, **96**, 168301.
19. Putnam,S.A. and Cahill,D.G. (2005) Transport of Nanoscale Latex Spheres in a Temperature Gradient, *Langmuir*, **21**, 5317–5323.
20. Würger,A. (2008) Transport in charged colloids driven by thermoelectricity, *Phys. Rev. Lett.*, **101**, 108302.
21. Vigolo, D., Buzzaccaro, S. & Piazza, R. (2010) Thermophoresis and Thermoelectricity in Surfactant Solutions. *Langmuir* **26**, 7792-7801.
22. Weinert,F.M. and Braun,D. (2008) Observation of Slip Flow in Thermophoresis, *Phys. Rev. Lett.*, **101**, 168301.
23. Astumian,R.D. (2007) Coupled transport at the nanoscale: The unreasonable effectiveness of equilibrium theory, *Proc. Nat. Acad Sci. USA*, **104**, 3-4.
24. Astumian,R.D. (2007) Equilibrium theory for a particle pulled by a moving optical trap, *J. Chem. Phys.*, **126**, 111102.
25. Hill,N.E. (1969) Temperature dependence of the dielectric properties of water, *J. Phys C*, **3**, 238-239.
26. Ning,H., Buitenhuis,J., Dhont,J.K.G. and Wiegand,S. (2006) Thermal diffusion behavior of hard-sphere suspensions, *Journal of Chemical Physics*, **125**, 204911.
27. Dhont,J. K. G. and Briels,W. J. (2008) Single-particle thermal diffusion of charged colloids: Double-layer theory in a temperature gradient, *European Physical Journal E*, **25**, 61-76.
28. Piazza,R., Vigolo,D. and Braibanti,M. (2008) Does thermophoretic mobility depend on particle size?, *Physical Review Letters*, **100**, 108303.
29. Baaske,P., Duhr,S. and Braun,D. (2007) Melting curve analysis in a snapshot, *Applied Physics Letters*, **91**, 133901.
30. Cordero,M.L., Verneuil,E., Gallaire,F. and Baroud,C.N. (2009) Time-resolved temperature rise in a thin liquid film due to laser absorption, *Physical Review E*, **79**, 011201.

31. P. Reineck, C.J. Wienken, D. Braun (2010) Thermophoresis of Single Stranded DNA, *Electrophoresis*, **31**, 279.
32. Nkodo, A.E. et. al. (2001) Diffusion coefficients of DNA molecules during free solution electrophoresis, *Electrophoresis*, **22**, 2424-2432.
33. Tinland, B. et al. (1997) Persistence length of single stranded DNA, *Macromolecules*, **30**, 5764-5765.
34. Record,M. T., Anderson,C. F. and Lohman,T. M. (1978) Thermodynamic analysis of ion effects on the binding and conformational equilibria of proteins and nucleic acids: the roles of ion association or release, screening, and ion effects on water activity, *Quarterly Review of Biophysics*, **11**, 103−178.
35. Manning,G. S. (1978) The molecular theory of polyelectrolyte solutions with applications to the electrostatic properties of polynucleotides. *Quarterly Review of Biophysics*, **11**, 179-246.
36. L. C. Bock, L. C. Griffin, J. A. Latham, E. H. Vermaas, J. J. Toole, (1992) Selection of single-stranded-DNA molecules that bind and inhibit human thrombin. *Nature*, **355**, 564.
37. Schoenborn JR, Wilson CB. (2007) Regulation of interferon-gamma during innate and adaptive immune responses. *Adv. Immunol.* **96**, 41–101.
38. Rothbauer, U. et al. (2006) Targeting and tracing antigens in live cells with fluorescent nanobodies. *Nature Methods*, **3**, 887-889.
39. Wienken,C.J., Baaske,P., Rothbauer,U., Braun,D., Duhr,S. (2010) Protein Binding Assays in Biological Liquids using Microscale Thermophoresis. *Nature Communications*, **1**:100.
40. MacKenzie, C. R. et al. (1996) Analysis by Surface Plasmon Resonance of the Influence of Valence on the Ligand Binding Affinity and Kinetics of an Anti-Carbohydrate Antibody. *J. Bio. Chem.*, **271**, 1527-1533.
41. Chen, Y., Müller, J.D., Tetin, S.Y., Tyner, J.D. Gratton, E. (2000) Probing Ligand Protein Binding Equilibria with Fluorescence Fluctuation Spectroscopy. *Biophys. J.*, **79**, 1074-1084.
42. Jecklin, M.C., Schauer, S., Dumelin, C.E., Zenobi, R. (2009) Label-free determination of protein-ligand binding constants using mass spectrometry and validation using surface plasmon resonance and isothermal titration calorimetry. *J. Mol. Recognit.,* **22**, 319–329.

43. Walker, E.H. et al. (2000) Structural Determinants of Phosphoinositide 3-Kinase Inhibition by Wortmannin, LY294002, Quercetin, Myricetin, and Staurosporine. Molecular *Cell*, **6**, 909–919.
44. Hemmings, H.C. Protein Kinase and Phosphatase Inhibitors, Applications in Neuroscience, (Humana Press, New York, 1997).
45. Cheung, W.Y. (1980) Calmodulin plays a pivotal role in cellular regulation. *Science*, **207**, 19-27.
46. Project, E., Friedman, R., Nachliel, E., Gutman, M. (2006) A molecular dynamics study of the effect of Ca2+ removal on calmodulin structure. *Biophys. J.*, **90**, 3842-3850.
47. Tsuruta, H., Sano, T. (1990) A fluorescence temperature-jump study on Ca^{2+}-induced conformational changes in calmodulin. *Biophys. Chem.,* **35**, 75-84.
48. Mayer G. (2009) The Chemical Biology of Aptamers *Angew. Chem. Int. Ed.*, **48**, 2672.
49. Ellington, A. D., Szostak, J. W. (1990) Invitro selection of RNA molecules that bind specific ligands. *Nature*, **346**, 818.
50. Tuerk, C., Gold, L. (1990) Systematic evolution of ligands by exponential enrichment – RNA ligands to bacteriophage-T4-DNA-polymerase. *Science*, **249**, 505.
51. Robertson, D. L., Joyce, G. F. (1990) Selection invitro of an RNA enzyme that specifically cleaves single stranded DNA. *Nature*, **344**, 467.
52. Boese, B., Corbino, K., Breaker, R. (2008) In vitro selection and characterization of cellulose-binding RNA aptamers using isothermal amplification *Nucleosides, Nucleotides, Nucleic Acids*, **27**, 949.
53. Cho, E., Lee, J., Ellington, A. (2009) Applications of Aptamers as Sensors *Annu. Rev. Anal. Chem.*, **2**, 241.
54. Jhaveri, S., Kirby, R., Conrad, R., Maglott, E., Bowser, M., Kennedy, R., Glick, G., Ellington, A. (2000) Designed signaling aptamers that transduce molecular recognition to changes in fluorescence intensity *J. Am. Chem. Soc.*, **122**, 2469.
55. Xiao, Y., Lubin, A. A., Heeger, A. J., Plaxco, K. W. (2005) Label-Free Electronic Detection of Thrombin in Blood Serum by Using an Aptamer-Based Sensor. *Angew. Chem. Int. Ed.*, **44**, 5456.
56. Song, S., Wang, L., Li, J., Fan, C., Zhao, J. (2008) Aptamer-based biosensors. *Trends Anal. Chem.*, **27**, 108.

57. Ho, D., Falter, K., Severin, P., Gaub, H. E. (2009) DNA as a Force Sensor in an Aptamer-Based Biochip for Adenosine. *Anal. Chem.*, **81**, 3159.
58. Lin, C.H., Patel, D.J. (1997) Structural basis of DNA folding and recognition in an AMP-DNA aptamer complex: distinct architectures but common recognition motifs for DNA and RNA aptamers complexed to AMP. *Chem. Biol.*, **4**, 817-832.
59. Baaske, P., Wienken, C.J., Reineck, P., Duhr, S., & Braun, D. (2010) Optical Thermophoresis for Quantifying the Buffer Dependence of Aptamer Binding. *Angew. Chem. Int. Ed.*, **49**, 2238-2241.
60. Dufour, C., Dangles, O. (2005) Flavonoid–serum albumin complexation: determination of binding constants and binding sites by fluorescence spectroscopy. *Biochim. Biophys. Acta*, **1721**, 164–173.
61. Fägerstam, L.G. et al. (1990) Detection of antigen – antibody interactions by surface plasmon resonance. Application to Epitope Mapping. J. Mol. Recognit. **3**, 208-214.
62. Shankaran, D.R., Gobi, K. & Miura, N. (2007) Recent advancements in surface plasmon resonance immunosensors for detection of small molecules of biomedical, food and environmental interest. *Sensors and Actuators B: Chemical*, **21**, 158-177.
63. Bornhop, D.J. et al. (2007) Free-Solution, Label-Free Molecular Interactions Studied by Back-Scattering Interferometry. *Science*, **317**, 1732-1736.
64. Markov, D.A., Swinney, K. & Bornhop, D.J. (2004) Label-free molecular interaction determinations with nanoscale interferometry, *J. Am. Chem. Soc.*, **126**, 16659–16664.
65. Latham, J.C., Markov, D.A., Sorensen, H.S. & Bornhop, D.J. (2006) Photobiotin surface chemistry improves label-free interferometric sensing of biochemical interactions, *Angew. Chem. Int. Ed.*, **45**, 955–958.
66. Leavitt, S., Freire, E. (2001) Direct measurement of protein binding energetics by isothermal titration calorimetry. *Curr. Opin. Struct. Biol.*, 11, 560-566.
67. Doty,P. (1957) The physical chemistry of deoxyribonucleic acids. *J. Cell Comp. Physiol.*, **49**, 27.
68. Marmur,J., Doty,P. (1959) Heterogeneity in Deoxyribonucleic Acids: I. Dependence on Composition of the Configurational Stability of Deoxyribonucleic Acids. *Nature*, **183**, 1427-1429.
69. Marmur,J., Doty,P. (1962) Determination of the base composition of deoxyribonucleic acid from its thermal denaturation temperature. *J. Mol. Biol.* **5**, 109-118.

70. Ansevin,A.T, Vizard,D.L., Brown,B.W., McConathy,J. **(**1976) High-resolution thermal denaturation of DNA. I. Theoretical and practical considerations for the resolution of thermal subtransitions. *Biopolymers*, **15**, 153-174.
71. Mergny,J.L., and Maurizot,J.C. (2001) Fluorescence resonance transfer as a probe for G-quartet formation by a telomeric repeat. *ChemBioChem*, **2**, 124-132.
72. Reed,G.H., Kent,J.O., Wittwer,C.T. (2007) High-resolution DNA melting analysis for simple and efficient molecular diagnostics. *Pharmacogenomics*, **8**, 597-608.
73. Lyon,E. (2001) Mutation detection using fluorescent hybridization probes and melting curve analysis. *Expert Rev. Mol. Diagn.*, **1**, 92-101.
74. Iacopini,S., Rusconi,R., Piazza,R. (2004) The "macromolecular tourist": Universal temperature dependence of thermal diffusion in aqueous colloidal suspensions. *Phys. J. E*, **19**, 59-67.
75. Mergny,J. and Lacroix,L. (2003) Analysis of thermal melting curves. *Oligonucleotides*, **13**, 515-537.
76. Zuker,M. (2003) Mfold web server for nucleic acid folding and hybridization prediction. *Nucleic Acids Res.*, **31**, 3406.
77. SantaLucia,J. and Hicks,D. (2004) The thermodynamics of DNA structural motifs. Annu. Rev. *Biophys. Biomol. Struct*., **33**, 415–440.
78. Bommarito,S., Peyret,N., Santa Lucia,J. (2000) Thermodynamic parameters for DNA sequences with dangling ends. *Nucleic Acids Res.*, **28**, 1929–1934.
79. Allawi,H., SantaLucia,J. (1998) Nearest Neighbor Thermodynamic Parameters for Internal G-A Mismatches in DNA. *Biochemistry*, **36**, 10581-10594
80. Kankia,B.I. and Marky,L.A. (2001) Folding of the thrombin aptamer into a G-quadruplex with Sr(2+): stability, heat, and hydration. *J. Am. Chem. Soc.*, **123**, 10799-804.
81. Mast,C.B. and Braun,D. (2010) Thermal Trap for DNA Replication. *Phys. Rev. Lett.*, **104**, 188102.

IX. Acknowledgements

Die Arbeit in Dieters Gruppe war eine sehr schöne und vor allem inspirierende Erfahrung. Hier habe ich gelernt wie man wissenschaftliche Methoden entwickelt und wie man physikalische und biologische Fragestellungen richtig zu lösen vermag. Außerdem konnte ich, dank Dieters Unterstützung, ein breites Spektrum an wissenschaftlichen Methoden kennenlernen und einen tiefen Einblick in Wissenschaft erlangen. Vielen Dank Dieter!

Im Folgenden möchte ich mich bei allen bedanken, die mich in den letzten Jahren so tatkräftig unterstützt haben.

Philipp Baaske für die gemeinsame Arbeit, die Unterstützung bei physikalischen Fragen und für die gemeinsamen Kaffee-Pausen, die gemeinsamen Mess-Einsätze mit Fussball Live-Übertragungen und alle anderweitigen Abendbeschäftigungen.
Stefan Duhr für seine Hilfe bei biologischen und biochemischen Fragen und das gemeinsame Paper schreiben.
Philip Severin für die vielen Diskussionen und die Unterstützung in und außerhalb des Labors und für den legendären „Nur ein alkoholfreies Weißbier"-Abend mit Abschluss in der Vega Bar.
Franz Weinert für die vielen Newsbar Abende auf „nur ein Becks".
Christof, Hubert, Mario, Svenja und dem Rest des Braun Labs für die gute Stimmung und die netten Labkino-Abende.
Katja, Dominik, Jan und allen Anderen des Lehrstuhls Gaub, die kein eigenes Zuhause hatten. Danke für die vielen lustige gemeinsamen Abende und Nächte.
Ann und Dave für das Korrekturlesen all meiner englischen Schreibergüsse.
Ralf, Tom und Angelika für die Unterstützung im Chemielabor.
Petra für den super leckeren Kaffee.
Meinen beiden Brüdern Tobias und Jonas fürs einfach da sein.
Meinen Eltern, die mich immer unterstützt und an mich geglaubt haben. Meiner Oma für die immerwährende Unterstützung. Schön dass es Euch gibt!
Meiner Frau Uta, die mir immer zur Seite stand wenn es notwendig war und ohne die Alles nichts wäre. Ich liebe Dich!

X. Curriculum Vitae

Christoph Jens Wienken

Personal data

Address	Tannenstrasse 1 86438 Kissing Germany
E-Mail	christoph.wienken@gmx.de
Birth date	July, 27th, 1981 in München, Germany
Nationality	German

Education

03/2008-today	PhD student, Ludwig-Maximilians-University Munich, Germany
11/2006-11/2007	Diploma student, Ludwig-Maximilians-University Munich, Germany Topic: "*Thermophoresis on the Nanoscale – Optical and Electrical methods"*
10/2002-11/2007	Student physics, field biophysics, Ludwig-Maximilians-University Munich, Germany
06/2001	Abitur, Wernher-von-Braun Gymnasium Friedberg/Bay, Germany

Awards

07/2009	2nd place Munich Business Plan Competition with NanoTemper
05/2009	1st place "CyberOne 2009 Hightech Award" with NanoTemper

XI. Appendix A: Detailed description of the experimental setup

The schematic description in allows understanding the basic principle of a measurement of thermophoresis with a fluorescence microscope. A more detailed description of the components is now presented to facilitate the reproducibility of the experimental approach.

Microscope body. The thermophoresis setup is built on a modified AxioTech Vario fluorescence microscope from Zeiss AG in Oberkochen, Germany. An additional port for a camera or photomultiplier tube was added on top of the microscope to allow a usage of the setup for fluorescence measurements in the visible range as well as in the UV range below 300nm wavelength. The microscope was placed on a laser bench to reduce vibrations and distortions from the outside. The whole microscope is encapsulated in a box to avoid room light and thus minimize the fluorescence background. Typically, objectives with 40x magnification were used to image the sample (NA=1.2, Oil, Zeiss AG, Oberkochen, Germany and NA=0.8, Partec, Münster, Germany). The oil objective could only be used for experiments at room temperature as it would otherwise be in thermal contact with the sample, rendering a heating of the sample nearly impossible.

Temperature Control. The overall sample temperature can be controlled with a peltier element beneath the capillary, which allows to scan a broad range of sample temperatures with the precision of ±0.1 K. The used peltier elements were high power elements with a maximum ΔT of 68°C purchased from Telemeter Electronic GmbH (PC-128-10-05). They admitted a cycling of temperature and also a fast switching of temperature. The peltier elements were controlled by a EA-PS 3032-10B power supply (Elektro Automatik GmbH, Viersen, Germany) with a software control of the output current. The control was performed using two analog outputs of a NI-6229DAQmx measurement automation card (National Instruments, Austin, Texas). Furthermore, a sign switcher for the voltage used to drive the peltier element was build to allow a switching between cooling and heating via software. The circuit included a relay combined with a TTL output of the control computer. By setting the TTL to high or low the voltage for the peltier could be set to positive or negative voltage, respectively. On top of the peltier element a silicon waver of 525μm in height was placed to reduce the auto-fluorescence of the peltier surface especially in the blue to green emission regime. To keep the lower side of the peltier element at constant temperature the element was placed onto a copper block with an integrated tube for water cooling purposes. The copper block was kept at constant

temperature with a water bath (Ecoline RE207, Lauda Dr. R Wobser GmbH, Germany). To reduce vibrations due to the water flow through the copper block the pumping speed was reduced to the lowest possible value. As evaporated water condensed inside the peltier element and caused defects the elements were sealed with silicon rubber which had low thermal and electric conductivity.
The temperature of the peltier element was measured with a PT1000 temperature sensor. To read out the temperature a circuit was build to measure the resistance of the PT1000 without the disturbance of internal resistances of the measurement card. The linearity of the sensor was checked in the range from 5°C to 100°C. The temperature inside the capillaries was checked using the temperature dependence of the fluorescence intensity. Here, an offset of approximately 2°C between the temperature directly on top of the element and the temperature inside the capillary was found.

1d translation stage. A Misumi Translation stage was used to move the samples below the objective. This enabled a fully automated experiment measuring binding curves or multiple melting curves. The combined step-motor and stepper driver (PD2-110-42-232 PANdrive, Trinamic Motion Control GmbH, Hamburg, Germany) was addressed by Labview routines via RS232. The motor can resolve 200 steps per revolution and with a precision class positioning rail a positioning accuracy of 20 µm and a positioning repeatability of 3 µm was achieved. With this resolution an exact and reproducible positioning of the capillary in the focus of the microscope objective was possible which is essential for measurement automation.

Sample compartments. As measurement compartments various types of capillaries were used depending on the required conditions for the measurement. Experiments on the thermophoretic properties of molecules required a height as low as possible to reduce the induced convection. On the other hand the height has to be high enough to get enough fluorescence intensity of the labeled molecules. For most experiments a height between 50-200 µm was chosen. Typically, the capillaries are made of fused silica or borosilicate glass. For the analysis of single-stranded DNA molecules capillaries with a square cross-section and an inner diameter of 50 x 50 µm (Polymicro Technologies, Phoenix, USA) were used. For an automated measurement of the thermophoretic DNA properties over temperature borosilicate capillaries with a rectangular cross-section of 50 x 500 µm (Vitrotubes, Vitrocom, Mountain Lakes, USA) were used because it was not possible to repeatedly position the 50 x 50 µm capillaries in an automated manner.

An analysis of the thermophoretic parameters over temperature as it is necessary for thermophoretic melting curves, was performed in rectangular 100 x 1000 µm borosilicate capillaries (Vitrotubes, Vitrocom, Mountain Lakes, USA). These capillaries were chosen to reduce the effect of photobleaching as the sample is measured at one position multiple times. For melting experiments using the intrinsic fluorescence of tryptophan residues in proteins, capillaries with circular cross-section and an inner diameter of 200 µm (Vitrotubes, Vitrocom, Mountain Lakes, USA) were used. These capillaries were made of synthetic glass. This is essential as borosilicate tends to fluoresce when excited with UV radiation and the background fluorescence in the UV range needs to be reduced due to the low fluorescence intensity of the intrinsic protein fluorescence.

Measuring the change of the thermophoretic properties upon binding allows using higher capillaries as the relevant signal is a change relative to a measured unbound situation. For this kind of measurement capillaries of 100 µm inner diameter were used (Polymicro Technologies, Phoenix, USA). The sample consumption in such capillary formats is quite low as for example only 250 nl volume is needed to fill a 50 x 50 µm capillary of 10 cm length. Binding of molecules to the capillary surface is low and was tested by measuring residual fluorescence after rinsing the capillary with buffer.

Laser heating unit. The IR laser beam (Furukawa FOL1405-RTV-617-1480, 320 mW maximum power, AMS Technologies AG, Martinsried, Germany) enters the setup laterally between microscope body and objective and is deflected by a rotatable dichroic mirror (NT46-386, Edmund Optics, Barrington, USA) mounted in a Thorlabs cube. This way, highly local temperature gradients in solution can be generated as infrared radiation at a wavelength of 1480nm is strongly absorbed by water. The absorption length at 1480nm is around 320µm, the temperature profile shows a Gaussian profile with a $1/e^2$ diameter of 25 µm. The temperature profile was measured utilizing the temperature dependence of the fluorescent dye Cy5 in 1 x SSC (saline sodium citrate). Temperature differences in capillaries were reproducibly generated and measured with a precision of ±0.1 K. This error is estimated from the noise present in the spatially resolved fluorescence signal.

The peak temperatures of the Gaussian profile varied for the different applications. For analyzing the thermophoretic properties of ssDNA the temperature differences ranged between 2.3 K and 4.4 K. Here, the temperature gradients need to be only moderate to stay within the limits of our theory. For the acquisition of thermophoretic melting curves typically peak temperature differences of 6 - 15 K were applied to obtain a bigger change

in concentration and thus a better read-out. The effective sample temperature when plotting the temperature transition of a molecule was corrected for the additional temperature increase due to the laser heating. The same was done for analyzing biomolecular interactions were peak temperature differences of 2-6 K were used.

LED excitation and UV LED unit. Fluorescence was excited with Luxeon high-power LEDs (Luxeon V-star, cyan; Luxeon III-star, red; Luxeon, Calgary, Canada). The LEDs were built into a standard halogen lamp housing and driven at a current of 10–200 mA by a Thorlabs LDC210C constant current source, providing low illumination noise levels. For an excitation of intrinsic fluorescence a UV-LED (UVTOP UV LED, 285 nm, 0.8 mW, Thorlabs, Newton, New Jersey) driven by a LDC201CU (Thorlabs, Newton, New Jersey) was used. The LED was collimated with a UV grade lens and placed at the side of a Thorlabs cube with a dichroic mirror which reflects UV light below 310nm and is transparent for light of longer wavelength.

Fluorescence filter. The dichroic mirror was part of a standard Tryptophan filter set (F36-300) purchased by AHF Analysentechnik (Tübingen, Germany). The excitation filter was placed behind the UV grade lens to narrow the spectral broadness of the excitation light. The emission filter was placed in front of the photomultiplier tube. For standard fluorescence applications standard filtersets from AHF Analysentechnik were used (blue: F11-001, green: F46-003, red: F46-006)

Detection unit. Fluorescence images were recorded with a Sensicam QE CCD camera (PCO, Kelheim, Germany) in the visible spectral range and with photomultiplier tube (PMT) (P10PC, Electron Tubes, Uxbridge, UK) in case of the intrinsic fluorescence. Both camera and PMT were mounted on top of the microscope body with a 2-port switcher from Zeiss AG. This setup made 2-dimensional information accessible over the camera port which was used to position the laser and UV-LED but still provided access to the high sensitivity of a PMT for measuring the low light intensities typical for intrinsic fluorescence. Directly in front of the PMT, an aperture was installed which allowed to adjust the intensity of incoming light. With this an overexposure of the sensitive area of the PMT was prevented. To read out the counts from the PMT a NI measurement card (NI PCI-6602, National Instruments, Austin, Texas) was used which provided a sufficient rate to resolve the single photon voltage peaks of the PMT. A function generator (33220A,

Agilent Technologies Inc., Santa Clara, California) served as a time base for the PMT and allowed exact timing of the recorded intensity values.

XII. Appendix B: Measurement control using LabView

The graphical programming language LabView 8.2 (National Instruments, Austin, Texas) was used to control and read out all parts of the experimental setup. Depending on the detection unit (PMT or CCD) two different programs were created with control Vis for the NI counting card and the CCD camera, respectively. The front panels of both programs look quite similar and are exemplarily shown for the PMT detection in Figure 17. The functions are arranged in groups for the linear motor control, control of the PMT or CCD and control for the measurement periphery like IR laser, LED power or temperature of the peltier element.

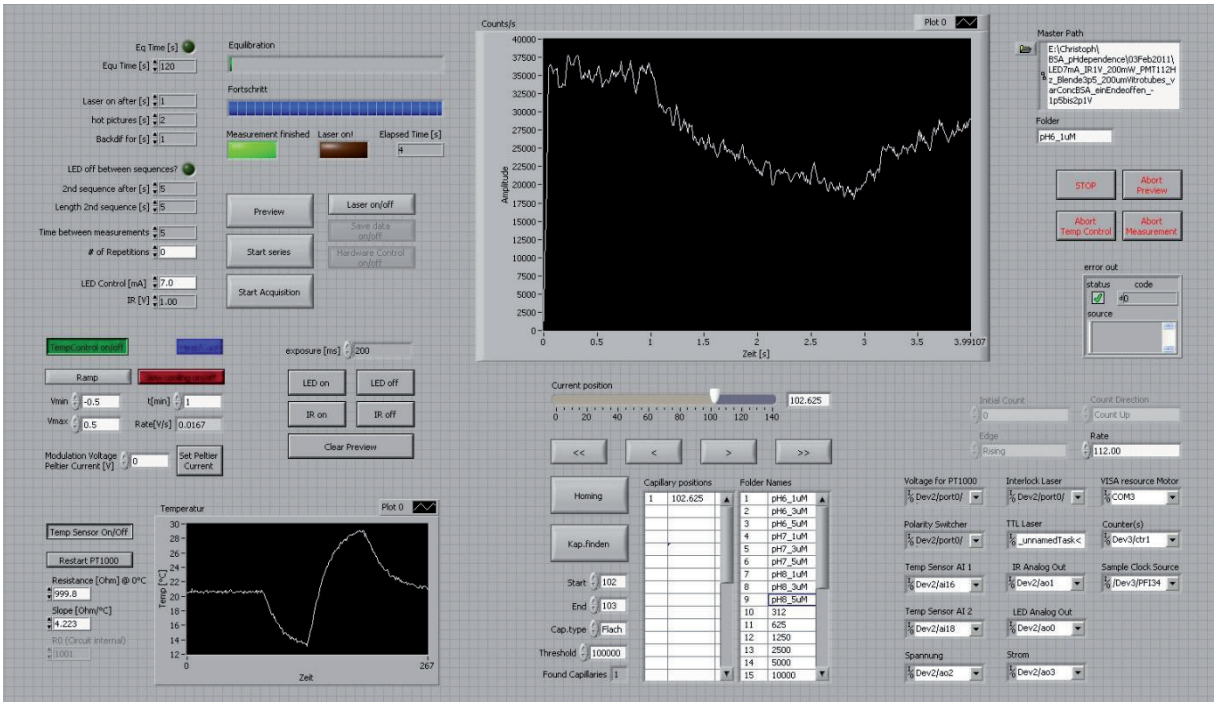

Figure 17 Overview Software for Measurement Control. *The frontpanel allows entering and changing all relevant measurement parameters and gives and direct response for the quality of the recorded data sets.*

Resources. In these fields the ports of the NI measurement cards are assigned to variables in the LabVIEW software (Figure 18). They are then used to control the devices automatically. If the software is migrated to another setup with comparable components the new physical ports can be connected to the existing software via this panel.

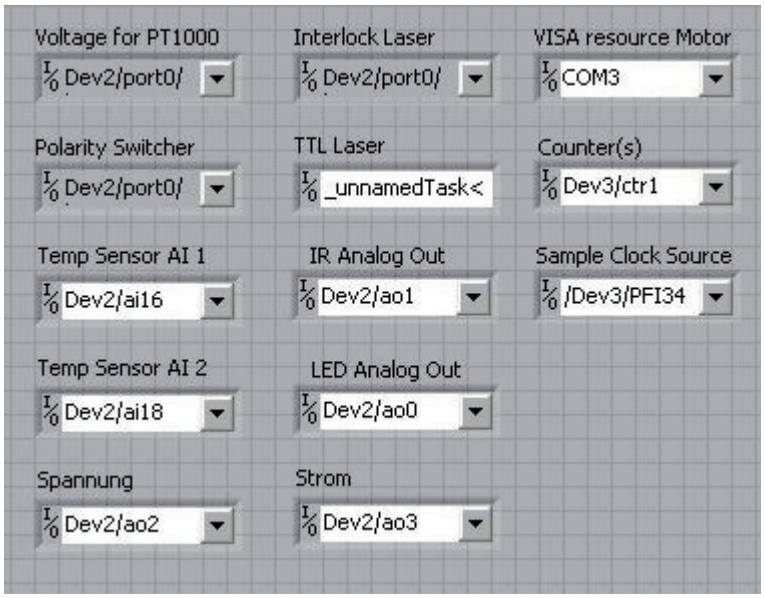

Figure 18 Resources. *All physical ports are connected to the LabVIEW software program over this interface.*

PMT control and CCD control. The parameters of the NI counting card have to be set correctly before starting to count the voltage peaks generated by the photomultiplier tube. Most of these attributes are set once before starting to operate except the attribute "rate" which needs to be set at the same frequency as the external clock (i.e. the function generator). The other properties must not be change and indicate at which value the counting should begin ("initial count"), in which direction the counting should run ("count direction") and if the rising or the falling edge of the voltage peak should be recognized (Figure 19).

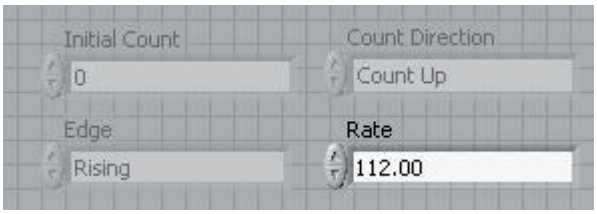

Figure 19 PMT parameters. *For control of the photomuliplier the software only needs the correct counting rate which is used to acquire the incoming light. The remaining properties (e.g. Count direction or which edge of the photon generated voltage pulse is detected) are fixed and deactivated.*

Figure 20 shows the panel for CCD settings. To assure that the CCD camera is working properly little more parameters have to be set correctly. First of all the kinetic cycle time

has to be set which tells you the acquisition rate. The unit is seconds so 0.2s means 5 images per second acquired. The corresponding exposure time is shown below which is shorter than the cycle time to ensure that the data is saved before taken the next image. To collect enough light per pixel typically 8x8 pixel are binned together. This can be set by choosing the parameter "Binning" with possible values from 1x1 to 8x8. It should be mentioned that with low binning values and short kinetic cycle times too large amounts of data have to be saved and the software may crash. But with typical settings for fluorescence recording the data acquisition works fine. Additionally, a gain can be set to increase the counts per photon measured by the CCD chip. This is typically set to 0. In the right panel "Parameters @ camera" the current settings are displayed. New parameters are written to the camera by pressing "Set Parameters". "Initialize Camera" restarts the camera in case of errors. Furthermore, it is possible to display the recorded images relatively to another image. The reference is taken by activating "Take Cold Image". Still when saving the recorded images the raw data is saved and not the relative values. By pressing "Remove Cold Image" the reference image is removed again.

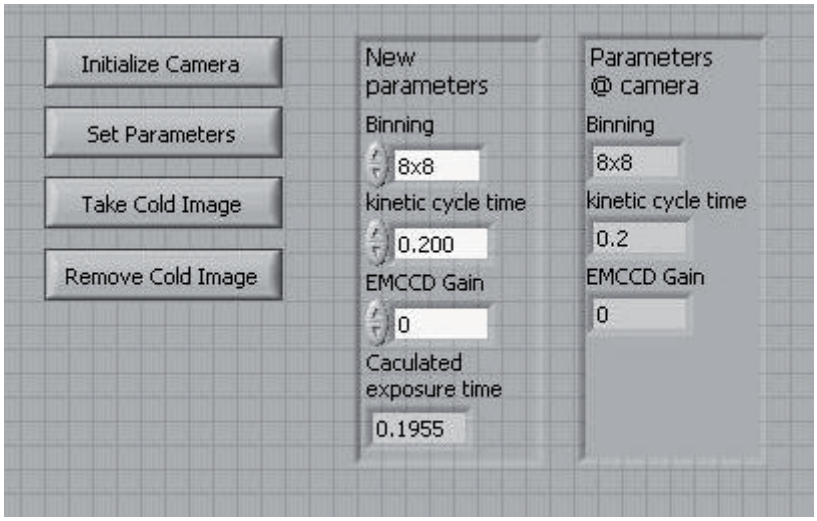

Figure 20 Parameters CCD camera. *This panel allows to adjust the most important properties of the CCD camera. If new parameters are entered in the "New parameters" window pressing "Set Parameters" sends the data to the camera. Furthermore, by "Take Cold Image" a reference image is taken and all images are then displayed relatively to this image.*

The images are displayed in an intensity graph were the lookup table can be manually adjusted. This intensity graph is shown in Figure 21. The values at the yellow cursor position are displayed in the indicator "Intensity @ cursor position". It further allows to mark the position of the IR laser by pressing "Set Cursor to Laserfocus". This is necessary

to position the capillary in such way that the heating occurs in the middle of the capillary. By activating "Set Cursor to Laserfocus" only the pixel with a radius of "Diameter Focus (Px)" around the cursor are used to measure the intensity when scanning for capillaries. By doing so errors in the positioning due to inhomogeneities in the illumination are reduced and the IR laser spot is placed in the middle of the capillary.

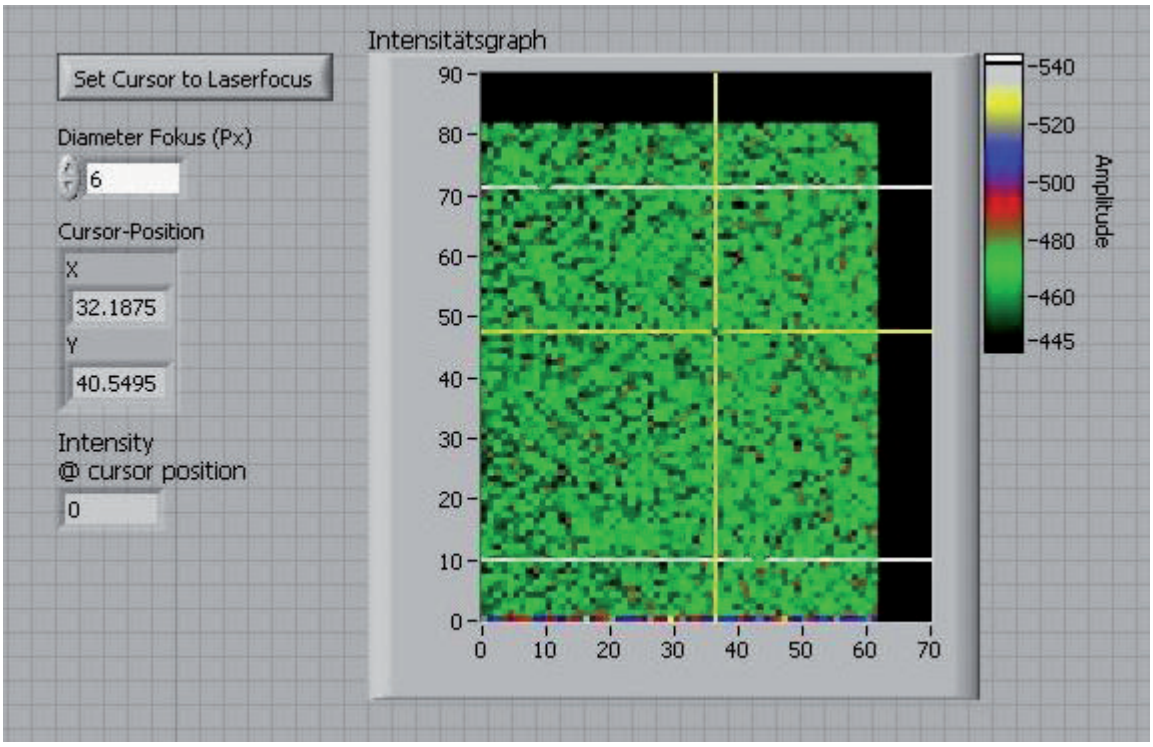

Figure 21 CCD camera image. *The image of the CCD camera is shown in an Intensity Graph. The intensity at the yellow cursor position is displayed. Furthermore, the yellow cursor has to be positioned at the laser focus and the button "Set Cursor to Laserfocus" has to be pressed. This is necessary for positioning the capillaries in such way that the laser focus is in the middle of the capillary.*

Parameters PT1000. The calibration parameters of the used PT1000 temperature sensor are entered here (Figure 22). PT1000 elements show a linear behavior of the resistance over temperature and thus the change in resistance can be converted into a temperature by the following formula:

$$R = Slope * T + R_{T@0°C} \qquad (5)$$

This temperature behavior was checked against a second commercial temperature sensor at 0°C in ice water and while heating up the water to 100°C. In the field "Parameters

PT1000" (Figure 22) the linear coefficients for the currently used PT1000 are set as standard. If the PT1000 element needs to be replaced the temperature calibration has to be performed again. It is also possible to switch on and off the readout of the sensor. Furthermore it is possible to restart the PT1000 if the sensor shows big fluctuations. This is sometimes the case as the PT1000 readout uses an internal 5V source which stays in an undefined state when the software crashes.

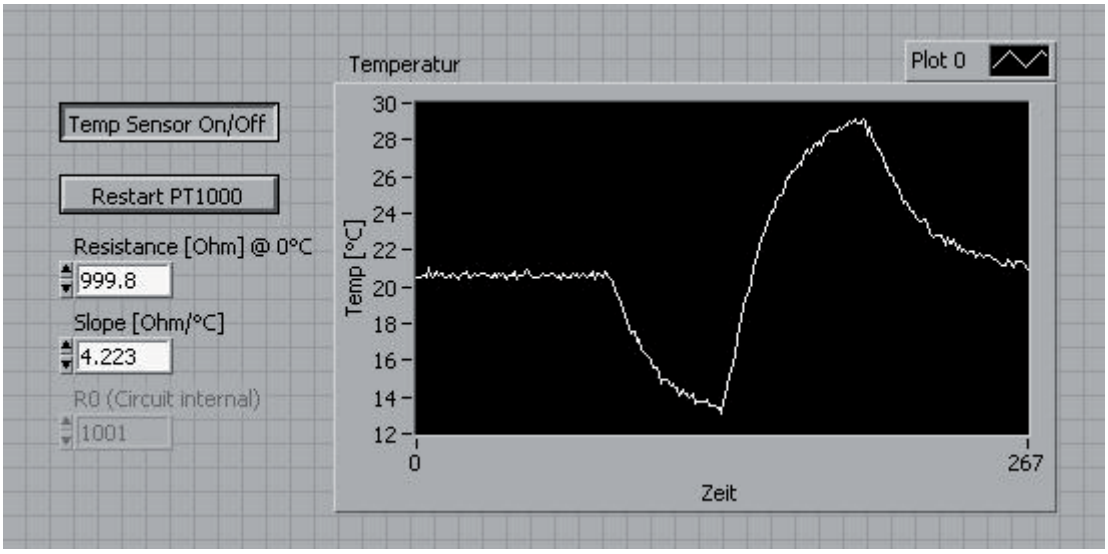

Figure 22 Temperature sensor. *A PT1000 temperature sensor is controlled by a NI card. It uses 5V output from a digital output which has to be set to a high value to enable the temperature readout. The level of the TTL can be changed by "Restart PT1000". The resistance at 0°C and the linear slope of the temperature behavior were adjusted by comparing the measured temperature against a calibrated thermometer.*

Peltier element control. The field "Peltier element control" (Figure 23, left) allows setting the temperature of the peltier stage. It is not possible to enter an actual temperature but just a voltage which is then applied to the power supply unit and there transferred into a current through the peltier element. The resulting temperature strongly depends on the temperature of the water bath below the peltier element and is difficult to be calculated in advance. With the button "Set Peltier Current" the voltage applied to the power supply to control the current through the peltier element is set to the value stated in "Modulation Voltage Peltier Current [V]". Negative values mean a switched polarity and result in cooling instead of heating. This also allows equilibrating the sample holder and also the samples at a given temperature before the actual measurement takes place. The current value through the peltier element is kept even when the software is switched off or crashes

which is necessary to keep the samples at a predetermined temperature and avoid any denaturing caused by an exposure to too high temperatures.

If a melting curve should be recorded it is possible to enter the minimum and maximum voltage which should be applied to the power supply unit. Furthermore, the duration of the ramp in minutes can be entered. The button ”Ramp” allows switching between a melting curve measurement and a measurement at constant temperature. Before starting a melting curve measurement the “Ramp” button needs to be activated. The “Slow cooling” button adds a slow cooling of the peltier element after the melting curve is completed to prevent a steaming up of the microscope objective. This is only necessary in an environment of high humidity. The button “heat/cool” indicates a heating or cooling by its color red or blue, respectively.

The CCD camera version of the Labview program also allows entering various voltage values in a table and also the corresponding temperatures (Figure 23, right). If this modus is chosen, the software sets the peltier current to the values in the table, equilibrates the system for the time stated in “Equilibrate before T-Step [min]” and then performs a measurement. When the measurement is finished it moves to the next value in the table and repeats the procedure. The data is saved in folders named after the temperature manually entered in the table. This modus of temperature control allows to measure the Soret coefficient at predetermined temperatures, but due to the equilibration time before each temperature step the duration of such a experiment is much longer than when performing a ramp heating where the temperature is monitored continuously.

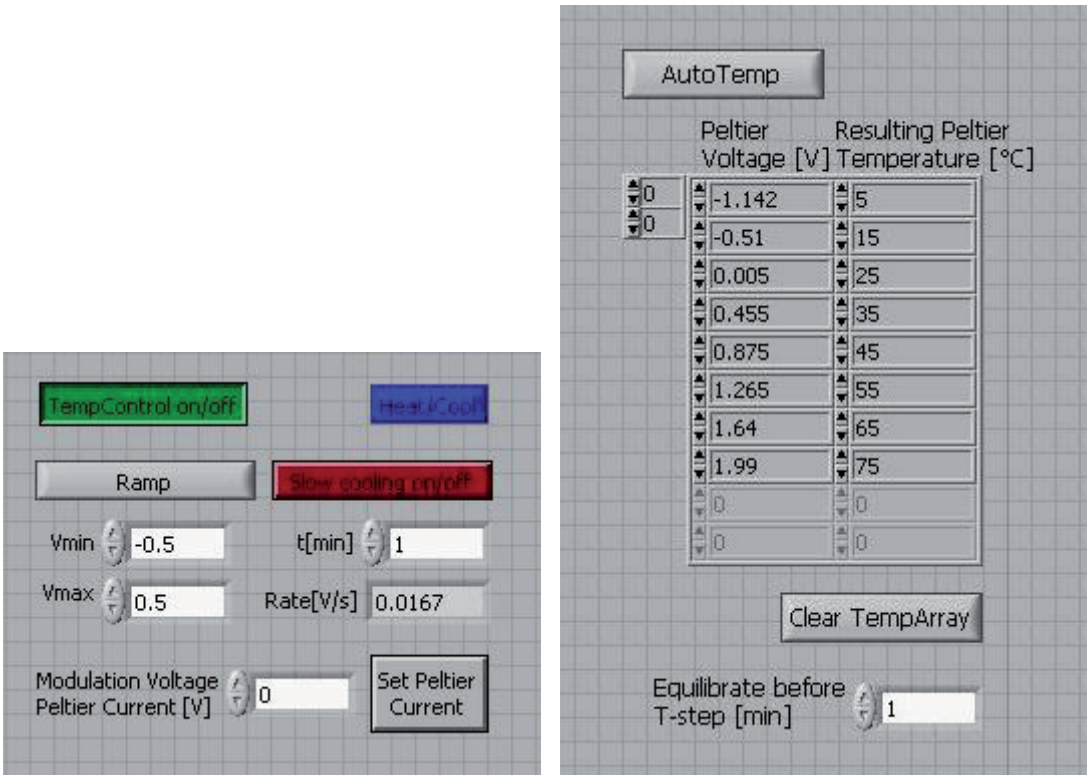

Figure 23 Temperature control. (LEFT) *The peltier elements below the sample can perform a heating ramp to measure the thermophoretic properties over temperature. Instead of a temperature range the minimum and maximum voltage to control the current source has to be entered, as the sample temperature highly depends on the temperature of the water bath below the peltier element. The control then ramps the control voltage from "Vmin" to "Vmax" in the time "t [min]". With "Set Peltier Current" the modulation voltage can be set to a distinct value. This is necessary to equilibrate the sample holder at a given temperature or to check for the sample temperature resulting from a given modulation voltage.* ***(RIGHT)*** *In the CCD camera software it is possible to measure the thermophoretic properties at predetermined modulation voltages. These voltages need to be entered in the left column of the table. In the right column the corresponding temperature can be entered. This temperature is used to save the data but the resulting temperature for a given modulation voltage has to be adjusted for every water bath temperature. Before measuring the samples at a determined temperature the sample needs to thermally equilibrate. This time is adjusted by varying the "Equilibrate before T-Step"-value.*

Preview. The preview modus allows recording the fluorescence data without any predetermined measurement routine (Figure 24). Pressing the "Preview" button starts the preview modus. The "exposure [ms]" sets the rate for data point acquisition in the preview

mode. “LED on” and “LED off” as well as “IR on” and “IR off” enable the LED or IR laser, respectively. The intensity for LED and IR laser are found under “Measurement parameters”. The button “Clear preview” clears the data shown in the “Counts/s” window and the preview starts recording at time zero again. The preview modus is necessary to adjust the focus of the microscope to the capillaries and also to identify the first and last capillary if a series of capillaries should be measured at once.

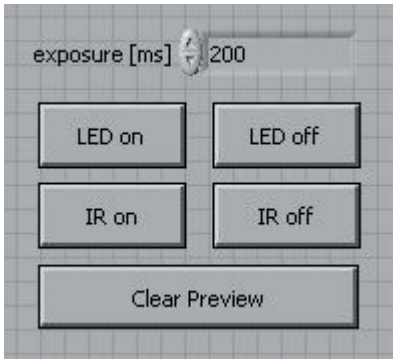

Figure 24 Preview control. *The preview modus allows monitoring the intensity of a sample and the LED and IR laser can be switched on manually. With this an estimate for the necessary LED intensity and for the temperature increase by the IR laser can be gained.*

Linear translation control. The position of the sample can be adjusted with a motorized 1d translation stage (Figure 25). Before using the motor a homing of the translation stage needs to be performed. By pressing ”Homing” the sample holder is moved to its maximum position which is then used as a reference. All positions used are then addressed relative to this home position which allows a much more exact positioning compared to an absolute positioning. With the arrow buttons the sample holder can be moved in both directions at two different speeds (two arrows: fast, one arrow: slow). By typing a position value into the box next to “current position” the motor stage moves to the entered position.

If more than one capillary should be measured it is necessary to identify the positions of these capillaries. Therefore, the capillaries should be in focus, and a position before the first capillary and after the last capillary should be entered in “Startpos.” and “Endpos.”, respectively. Furthermore the capillary type i.e. if round or rectangular capillaries are in use needs to be entered. The capillary type determines the algorithm to locate the capillary centers. In case of round capillary cross-sections a quadratic equation for each capillary is fitted into the intensity vs. position plot to identify the center positions of each capillary.

Rectangular capillaries require a threshold value and the center position is calculated as the mean between two following crossings of the intensity plot with the threshold line.
The positions of all identified capillaries are listed in the table “Capillary positions”. Here, it can be checked if the right number of capillaries was identified. In the table “Folder names” right next to the capillary positions a name for each found capillary can be entered. This name will be used later as the folder name to save the measurement data.

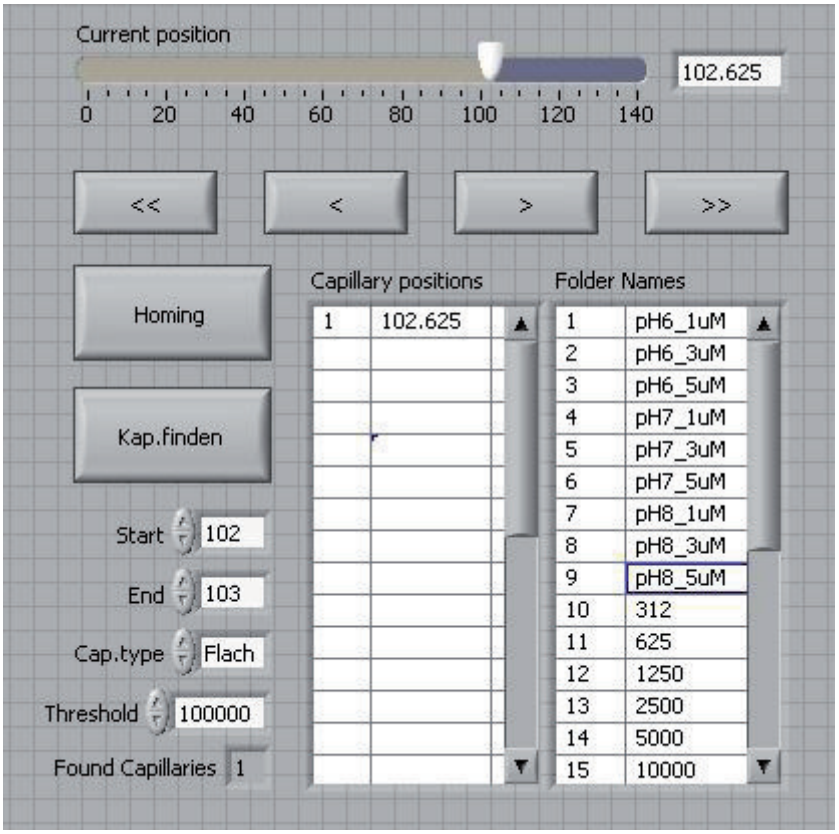

Figure 25 Linear translation control. *This panel controls and moves the translation stage of the sample holder. It also contains all necessary parameters to search for the capillary positions before a measurement and allows giving every capillary a distinct name for saving.*

Measurement parameters. The measurement parameters quantify the temporal sequence of the measurement periphery (Figure 26). A typical experiment consists of a period with LED excitation switched on but without laser heating (“Laser on after [s]”), followed by a period of powered LED and IR laser (“Hot pictures [s]”). When the used fluorophor shows strong bleaching the LED can be switched off for a given time to reduce photobleaching (“2nd sequence after [s]”). Thereafter, the LED is turned on again to monitor the change in fluorescence after the complete period of IR laser heating (“Length 2nd sequence [s]”).

Now the IR laser is turned off while the LED stays powered for a given duration ("Backdif for [s]"). This allows monitoring the backdiffusion after the temperature profile has collapsed. Before each measurement an equilibration can be performed ("Equ Time [s]"). When a melting curve should be recorded this equilibration needs to be switched off and the sample should be equilibrated manually before starting the measurement. If the "Series Acquisition" button is pressed to start the measurement an additional time between two measurements is inserted ("Time between measurements [s]"). This is important if there is too little time between two following measurement to ensure that the sample is again in an undisturbed homogenous molecule distribution. It is also possible to automatically repeat the complete series of measurements by changing the number of "# of repetitions". The repetitions are performed after all capillaries found during the capillary scan were measured or in case of a single acquisition directly after one measurement.

The current used to drive the LED is adjusted by "LED Control [mA]". Here, it is important, that the conversion of this value into a control voltage applied to the current controller is only correct for a 100mA current controller. For the 1A controller the

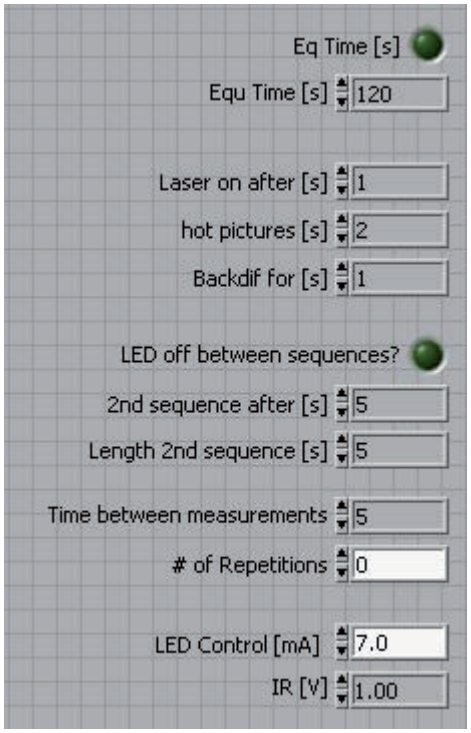

Figure 26 Measurement parameters. *This panel allows entering all relevant parameters to measure the thermophoretic properties of a sample. If the fluorescent dye experiences strong bleaching, the LED can be switched off during the measurement to reduce bleaching artifacts.*

conversion has to be adjusted. The IR power is controlled by applying 0-5V to the modulation port of the IR laser module. This voltage is adjusted via the "IR [V]" box. The laser diode starts lasing at around 0.5V control voltage and reaches its maximum of around 200mW (or 500mW, depending on the laser diode in use) at 5V.

Miscellaneous software functionalities. Beside above mentioned grouped functions the software contains additional panels to start or monitor the measurement (Figure 27). With "Preview", "Start series" and "Start Acquisition" the type of measurement can be selected. The "Start Acquisition" starts a measurement at the current position and does not use the automated 1d translation. "Start series" measures at every capillary position found in a preceding capillary scan. "Preview" allows monitor the intensity without any defined measurement sequence and can be used to focus the sample with the objective or to find any impurities of the capillaries or samples.

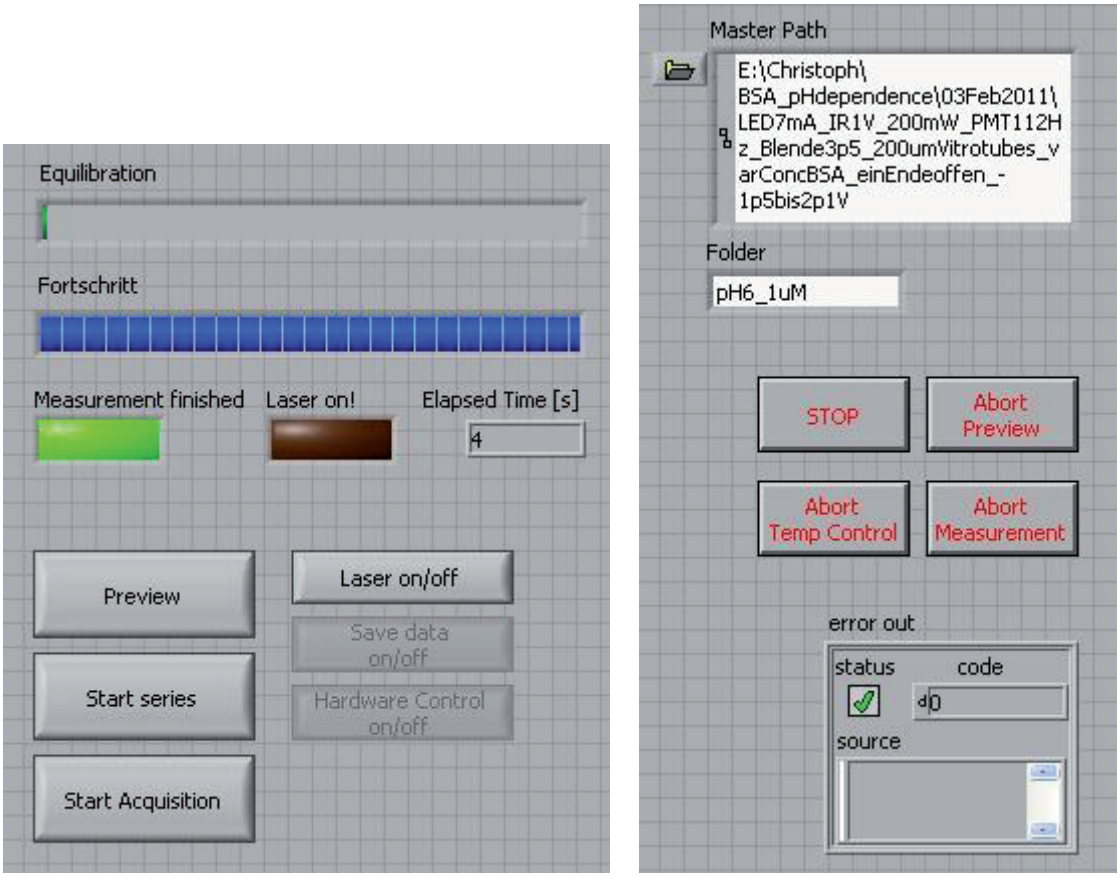

***Figure 27 Miscellaneous functions**. Further functions like progress bars, an error handler and switches to abort functions of the software provide access to most functionalities of the software. Further the path and folder for saving the data has to be entered here.*

Furthermore, the IR laser can be turned off with “Laser on/off”, as well as the saving procedure (“Save data”; this button is deactivated and only for testing purposes.) The software also contains progress bars for both the equilibration and the measurement. This is necessary to show the programs activity while it waits for reaching thermal equilibrium or while it records the measurement data. During the measurement, the data is not shown in a live preview to maintain correct timing.

The software also contains an error handler which helps debugging in case of software problems and Stop buttons to abort the various subroutines of the program. Furthermore, the “Master Path” used for saving the data has to be entered before a measurement. Additionally, a subfolder of this master path is created with the name “folder”. The data is then saved under \Master Path\Folder\ . In case of a series acquisition using capillary positions the “folder” names are automatically taken from the list entered next to the capillary positions.

XIII. Appendix C: Publications

Publications

1. Thermophoresis of single stranded DNA. Reineck, P., Wienken, C. J. & Braun, D. *Electrophoresis* **31**, 279–286 (2010).
2. Optical Thermophoresis quantifies Buffer dependence of Aptamer Binding, Philipp Baaske, P., Wienken, C.J., Reineck, P., Duhr, S., Braun, D. *Angew Chem Int Ed* **49**, 2238–2241 (2010).
3. Protein binding assays in biological liquids using microscale thermophoresis. Wienken, C.J., Baaske, P., Rothbauer, U., Braun, D., Duhr, S. *Nat Commun*, **1**:100 (2010) doi:10.1038/ncomms1093.
4. Thermophoretic melting curves quantify the conformation and stability of RNA and DNA. Wienken,C.J., Baaske,P., Duhr,S. and Braun,D. *Nucl Acids Res*, 1–10 (2011) doi:10.1093/nar/gkr035.
5. Peptide surfactants for cell-free production of functional G protein-coupled receptors. Wang, X., Corin, K., Baaske, P., Wienken, C.J., Jerabek-Willemsen, M., Duhr, S., Braun, D. and Zhang, S. *Proc Nat Acad. Sci. USA* (2011) doi:10.1073/pnas.1018185108

Patent Applications

1. Method and device for particle analysis using thermophoresis , Philipp Baaske, Stefan Duhr, Christoph J. Wienken, Dieter Braun, PCT/EP2009/056162 (2009).

Fast Track

Philipp Reineck
Christoph J. Wienken
Dieter Braun

Department of Physics, Systems Biophysics, Center for Nanoscience, Ludwig Maximilians Universität München, München, Germany

Received August 24, 2009
Revised October 16, 2009
Accepted October 16, 2009

Research Article

Thermophoresis of single stranded DNA

The manipulation and analysis of biomolecules in native bulk solution is highly desired; however, few methods are available. In thermophoresis, the thermal analog to electrophoresis, molecules are moved along a microscopic temperature gradient. Its theoretical foundation is still under debate, but practical applications for analytics in biology show considerable potential. Here we measured the thermophoresis of highly diluted single stranded DNA using an all-optical capillary approach. Temperature gradients were created locally by an infrared laser. The thermal depletion of oligonucleotides of between 5 and 50 bases in length were investigated by fluorescence at various salt concentrations. To a good approximation, the previously tested capacitor model describes thermophoresis: the Soret coefficient linearly depends on the Debye length and is proportional to the DNA length to the power of 0.35, dictated by the conformation-based size scaling of the diffusion coefficient. The results form the basis for quantitative DNA analytics using thermophoresis.

Keywords:
Capillary / Single stranded DNA / Thermophoresis
DOI 10.1002/elps.200900505

1 Introduction

Simple methods to analyze molecules in solution are rare but highly sought-after for molecular biology. For example, electrophoresis is still the backbone of most DNA sequencing approaches and is a reliable tool in molecular biology. Methods to analyze molecules in bulk solution are important since surface-based approaches often render proteins or even DNA disfunctional. Molecules move along a microscopically applied temperature difference of only a few Kelvin (Fig. 1A). This effect is termed thermophoresis, thermal diffusion or the Soret effect. Thermophoresis has only recently been pursued on the biological realm [1, 2, 3]. Based on these measurements, one can expect that thermophoresis reveals information about the native interface between molecule and solvent with high sensitivity, allowing the sensitive probing of biomolecule binding (Wienken, C. J. *et al.* and Baaske, P. *et al.*, submitted). In contrast to electrophoresis, the molecules are probed in physiological buffer, in the future possibly even in such complex fluids as, for example, blood serum.

Here we present measurements for single stranded DNA and describe the results with a microscopic theory without fitting parameters. The results allow the extrapolation of thermophoresis for similar biological molecules. Besides measuring the Soret coefficient, *i.e.* the strength of the thermophoretic effect, the diffusion coefficients of the molecules are also measured. Measurements are performed on the timescale of several minutes and are performed in sample volumes well below one microliter. We report on an optical, capillary-based technique which yields highly reproducible and sensitive results. Notably, the combination of thermophoresis and fluid flow also allows for a number of conditions in which molecules are strongly accumulated [4–8] and the thermophoretic effect is exponentially amplified.

1.1 Basics of thermophoresis

While thermophoresis bodes well for biomolecule analysis in minute sample volumes, the fundamental description of thermophoresis is the subject of a long standing debate with ongoing experimental efforts. Among others, our group has argued in the past that in the limit of diluted molecules, under interface-free optical conditions and the typically used moderate temperature gradients, the steady state of thermophoresis can be described by a local Boltzmann distribution of the particle density. In thermophoresis, unlike in electrophoresis, the particle movement is dominated by diffusion, not by the particle drift. An effective Peclet number P_e can be given by

$$P_e = a\frac{v}{D} = a\frac{D_T}{D}\nabla T = aS_T\nabla T \quad (1)$$

Correspondence: Professor Dieter Braun, Department of Physics, Systems Biophysics, Center for Nanoscience, Ludwig Maximilians Universität München, Amalienstr. 54, 80799 München, Germany
E-mail: dieter.braun@lmu.de
Fax: +49-89-2180-16558

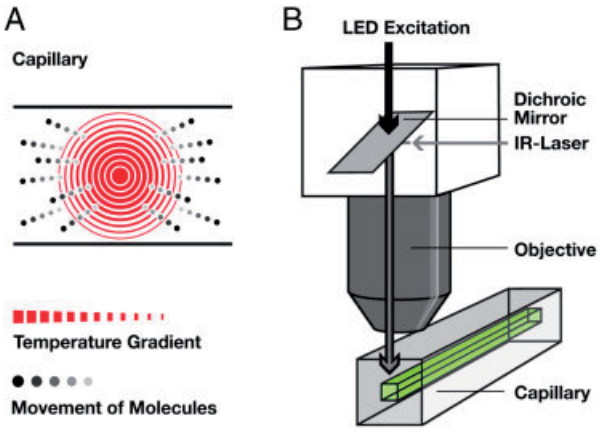

Figure 1. Thermophoresis and setup. (A) Molecules move in a temperature gradient, an effect termed thermophoresis. Typically, the movement in aqueous solutions is directed away from regions of elevated temperature. (B) We measure thermophoresis inside a rectangular capillary with a $50\,\mu m \times 50\,\mu m$ cross-section. The temperature gradient is applied locally on the micrometer scale by an infrared laser. The concentration of the molecules is monitored with a fluorescent tag on the molecule. The temperature distribution in the capillary is measured in a separate measurement utilizing a temperature-sensitive fluorescent dye.

with particle radius a, particle drift velocity v, diffusion coefficient D, thermophoretic mobility D_T, Soret coefficient S_T and the temperature gradient ∇T. The diffusive movement of single molecules allows the reversible equilibration between particle positions due to temperature differences in the Gibbs free enthalpy of the molecule-solvent complex [1, 9–13]. This results in a steady-state molecule distribution which is given by a linear thermophoretic drift $v = -D_T \nabla T$ and the backdiffusion flux $j = -D\nabla c$ with diffusion coefficient D. Only under the condition $P_e \gg 1$, which is experimentally challenging to achieve even for micrometer-sized particles, we could experimentally confirm a local fluid flow of solvent around the molecules [14]. The Soret coefficient is defined as the ratio $S_T = D_T/D$ and determines the magnitude of thermodiffusion in steady state. With above assumptions, it is given by the temperature derivative of the Gibbs free energy G of the molecule-solvent complex [1, 15]:

$$S_T = \frac{1}{k_B T}\frac{\partial G}{\partial T}. \qquad (2)$$

This approach was previously tested with polystyrene beads with varying particle size, salt concentration and temperature and for the case of double stranded DNA with varying length. The results were described quantitatively without fitting parameters [1]. Further confirmation of the approach was found from the study of quartz beads [16]. Extensions of the theory were reported in [17]. Subsequent experiments on polystyrene beads [18] came to different conclusions concerning the size dependence. Results obtained using an electrical heating grid remained inconclusive [19]. It should however be mentioned that the use of interfaces to apply the temperature gradient as used in [18, 19] could allow for to the buildup of electrical fields which in turn leads to the rather complex coupling of thermophoresis and electrophoresis [20]. On the other hand, we expect that optical application of the temperature difference used in our study (Fig. 1B) strongly reduces such buildup of "thermoelectrophoresis" due to the lack of an interface layer which can be charged. Test measurements were unable to confirm the influence of electrical fields in our experimental settings (unpublished results).

While it is difficult to precisely chemically modify the surface of polystyrene beads in a way that the modification is independent of particle size, DNA is a highly defined and characterized molecule. DNA is biologically highly relevant and gives us a defined length and molecule characteristics. We measured single stranded DNA from 5 to 50 bases in length. Double stranded DNA was measured previously in a length range above the persistence length of double stranded DNA, namely between 50 and 50000 base pairs. As before, we used a length range where the polymer length and diameter yields approximately a spherical molecule geometry. Previously, the measurements were restricted to comparably low salt concentrations due to indications of DNA sticking to the used planar chambers. The capillaries used here show considerably less surface interactions and well-defined washing steps after the measurement allow the precise quantification of sticking. Overall, the approach allowed us now to test theoretical predictions for polymers other than double stranded DNA.

The manuscript is structured as follows: we describe the capillary-based measurement procedure, check the validity of the used theoretical modeling of the measurement, report on the measured Soret and diffusion coefficients and describe the measurements with a microscopic theory of double layer energies.

2 Materials and methods

2.1 Setup and measurement chambers

A modified fluorescence microscope shown schematically in Fig. 1 has been utilized to obtain temperature and concentration distributions in solution. The IR laser enters the setup laterally between microscope body and objective, is deflected by a rotatable dichroic mirror and is focused in the sample plane by the objective. The cube containing the dichroic mirror is mounted on a AxioTech Vario fluorescence microscope (Zeiss, Oberkochen, Germany). Fluorescence excitation is provided by a high performance LED (Luxeon, Calgary, Canada). The emission light is recorded by a Sensicam QE CCD camera (PCO, Kehlheim, Germany). Capillaries are made of fused silica with a square cross-section and an inner diameter of $50 \times 50\,\mu m$ (Polymicro Technologies, Phoenix, AZ, USA) and used as microfluidic measurement chambers. Inner dimensions vary only by $\pm 0.5\,\mu m$ *per* 10 m capillary length which significantly

enhances the reproducibility of temperature profiles generated in solution. Capillaries were filled by placing the sample solution in a micro test tube on one end of the capillary while air pressure was reduced slightly at the other end using a syringe. Subsequently, both ends were sealed with mineral oil in order to prevent the sample from evaporating. Pressure differences are allowed to equilibrate for at least 30 s to reduce undesired drift in the capillary. Only 250 nL sample volume is needed to fill a capillary of 10 cm length. Binding of molecules to the capillary surface is low and was tested by measuring residual fluorescence after rinsing the capillary with buffer. Experimental error for S_T measurements is ± 0.0021/K due to noise of the fluorescence signal in addition to a relative error of ± 2.3 to $\pm 4\%$ which accounts for the precision of the temperature measurements. Diffusion constants are determined with an accuracy of ± 10 to $\pm 20\%$ since depletion kinetics of simulations match measured traces equally well within this range.

2.2 Infrared heating

Temperature gradients in solution were generated locally by the absorption of an infrared laser (Fibotec Fiberoptics Meiningen, Germany) at a wavelength of 1450 nm. At this wavelength water strongly absorbs with an absorption length of 320 μm. The collimated IR laser beam was focused in the sample plane by the microscope objective (Fig. 1). Temperature differences created in solution ranged between 2.3 and 4.4 K. These were measured utilizing the temperature dependence of the fluorescent dye Cy5 (carboxymethylindocyanine-*N*-dyroxysuccinimmidyl ester) in $1 \times$ SSC, which was determined independently. Temperature differences in capillaries were reproducibly generated and measured with a precision of ± 0.1 K. This error is estimated from the noise present in the spatially resolved fluorescence signal and from the precision with which the IR laser can be positioned in the center of the capillary.

2.3 Molecules

Single stranded DNA of 5, 10, 22 and 50 bases (Biomers, Ulm, Germany) were diluted to 1 μM and investigated at different salt concentrations. The following sequences were used:

5-mer: 5′- Hex–TA GTT–3′ 10-mer: 5′- Hex–TA GTT CTA AT–3′; 22-mer: 5′- Hex–AT TGA GAT ACA CAT TAG AAC TA–3′ 50-mer: 5′- Hex–ATAATCTGTAGTACTGCAGA AAACTTGTGGGTTACTGTTTACTATGGGGT–3′.

The solution was buffered with 1 mM Tris at pH 7.6. The Debye length was titrated with KCl according to

$$\lambda_{DH} = \sqrt{\frac{\varepsilon_0 \varepsilon_r k_B T}{2 N_A e^2 (c_S + c_T)}} \quad (3)$$

where ε_0 is permittivity of free space, ε_r the dielectric constant of water, $k_B T$ the thermal energy, N_A is Avogadro's number, e the elementary charge and c_S and c_T are concentration of KCl and Tris, respectively. All oligonucleotides were labeled with HEX (-carboxy-2′,4,4′,5′,7,7′-hexachlorofluorescein) at the 5′ end.

2.4 Measurements

Under typical measurement conditions, DNA moves against temperature gradients in solution. Therefore, in a region of elevated temperature, the DNA concentration decreases. If the molecules are fluorescently labeled this can be imaged by a local decrease in fluorescence intensity (Fig. 2). As shown in Fig. 3, this signal is evaluated over time in the heating center for a typical measurement: the infrared laser is turned on at time $t = 10\,s$ and turned off again after 240 s. During this time the temperature distribution in the solution is in steady state. As the molecules move away

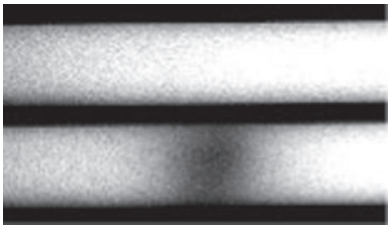

Figure 2. Microscopy of capillary fluorescence. Fluorescence images of the capillary containing labeled DNA before (top) and after (below) the temperature gradient is applied. Fluorescence decreases due to particles moving away from the hot spot.

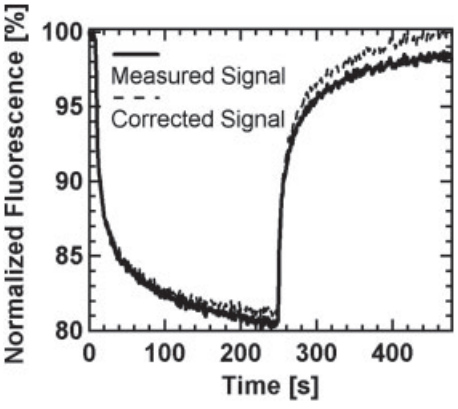

Figure 3. Time trace and bleaching. Normalized fluorescence in the heating center evaluated over time. At time $t = 10$ s a temperature gradient is applied and molecules move away from the hot spot as seen from the decrease of the fluorescence signal. Molecules diffuse back after the IR laser is turned off at $t = 250$ s. The signal does not fully recover due to bleaching (solid line). This artifact can be corrected for with high precision (dashed line).

from the hot spot, the concentration initially decreases exponentially. As soon as the IR laser is turned off, molecules freely diffuse back to a uniform concentration distribution. Due to low excitation intensities, bleaching artifacts are small and can be corrected precisely by fitting the change in fluorescence intensity from unheated regions of the capillary. Two quantities can be obtained from a measurement over time. The Stokes–Einstein diffusion constant D from the kinetics of the depletion dynamics and the Soret coefficient S_T from the magnitude of the depleted concentration.

2.5 Analyzing the measurements

1-D, 2-D and 3-D models of the measurement geometry and timing were created and evaluated utilizing finite element simulations (Femlab, Comsol, Stockholm, Sweden). The 1-D model represents a radially symmetric, two dimensional circular plane with a diameter of 800 μm in which the heating center and the center of the circle coincide. The 2-D and 3-D model are 800 μm in length as well but respect the capillary boundaries and are 50 μm wide (2-D and 3-D) and 50 μm in height (3-D). This way the influence of capillary geometry and convection (only 3-D) on the temporal evolution of diffusion processes were investigated. Heat transport through the capillary walls was included by the measured temperature profile. For numerical reasons, the concentration was held constant at the long ends of the capillary. Due to its distance to the heating center, back diffusion from the boundary did not affect the simulation. The flux equation accounting for diffusion and thermodiffusion is $\vec{j} = -D_T c \nabla T - D\nabla c$. We apply the continuity equation and add the term $\nabla(\vec{v}c)$ to introduce convection for the case of the 3-D simulation. The fluid velocity $\vec{v}$ is obtained by solving the Navier–Stokes equation. Therefore, we solved the time dependent partial differential equation $\partial c/\partial t = \nabla(D_T c \nabla T + D\nabla c) - \nabla(\vec{v}c)$. The temperature profile T was turned on and off instantaneously with heavy-side functions $\boldsymbol{\Theta}(t) = \boldsymbol{\Theta}_1(t - t_1)\boldsymbol{\Theta}_2(t_2 - t)$ due to the negligible thermal relaxation time in the millisecond regime. As the temperature is turned on at t_1 and turned off at t_2 the whole measurement procedure was simulated.

To compare different simulation models, we idealized a typical temperature distribution by a Gaussian profile with a width of $\sigma = 27$ μm and a peak temperature difference of 2.3 K. Other constants were chosen typical for the largest measured 50-mer single stranded DNA molecule with $D = 56\ \mu m^2/s$ and $D_T = 5.6\ \mu m^2/sK$ where measurement artifacts from thermal convection are expected to be maximal. The simulated time lines are shown in Fig. 4A. To probe thermal convection, the 3-D simulation was executed with and without gravity acting on the fluid. Maximum convection velocities emerged in the proximity of the focused IR laser $v_X = 77$ nm/s and $v_Z = 131$ nm/s (Fig. 4B) and were found to have no significant influence on the thermophoretic concentration depletion in steady state (<0.57%).

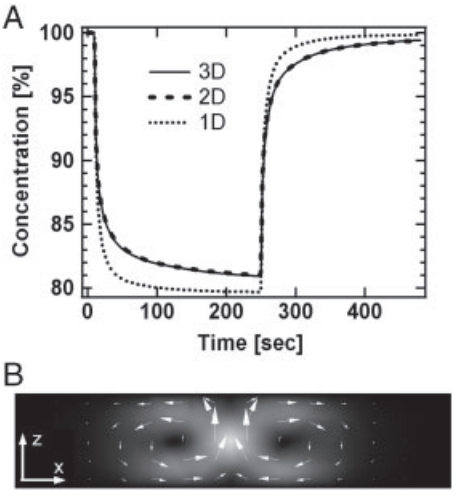

Figure 4. Simulation of thermophoretic depletion. (A) Simulation of the measurement process for the different model geometries, evaluated in the heating center. The 1-D model deviates from the 2-D and 3-D models significantly. (B) Side view of the 3-D simulation of the capillary. Maximum convection velocities occur in the heating center (center of the image) are $v_X = 77$ nm/s and $v_Z = 131$ nm/s and are indicated by the arrows. Results of the 2-D and 3D models are hardly distinguishable and show that the influence of convection is negligible.

To understand this deviation, we calculated the Peclet number $P_e = L \cdot u/D$, now applied on the scale of the measurement chamber. Its value determines whether a fluid system is dominated by diffusion or by the movement of the fluid. Here, $L = 27$ μm is the characteristic length of the system, $u = 130$ nm/s the velocity of the fluid due to convection and D the diffusion constant of the solved particles. For the slowest diffusing particle in our experiments, 50-mer single stranded DNA molecules, the Peclet number is calculated to $P_e = 0.063$. Since the convection flow is antiparallel to the thermophoretic outward drift at the chamber bottom and parallel at its top, deviations are likely to perturb the concentration profile in second order of the convection velocity. Indeed, the squared Peclet number ($P_e^2 = 0.40\%$) comes close the simulated deviations (0.57%). Overall, this indicates a clear domination of diffusive transport over the convective fluid flow.

However, the effect of the restricted capillary geometry on the temporal evolution of the model is significant and shown in Fig. 4A. Even though diffusion constants are identical, depletion kinetics in the spatially unrestricted 1-D model are much faster and the diffusion and the thermodiffusion fluxes almost fully equilibrate, *i.e.* at $t = 240$ s the 1-D simulation is very close to steady state while the concentration in the other models still decreases. Since the 2-D and 3-D simulations show rather small deviations of the depleted concentration, the 2-D model was chosen as the basis for the evaluation of measurements.

For comparison, we also evaluated analytical solutions to the diffusion equation. According to [21, 22] the axial diffusion equation under a Gaussian perturbation shows a central

concentration over time which can be approximated by

$$c(t,\tau,c_0,c_\infty) = c_\infty + c_0\left(1-\sum_{i=0}^{\infty}\frac{(-K)^i}{i![(2t/\tau+1)i+1]}\right) \approx \frac{c_0+c_\infty(t/\tau)}{1+t/\tau} \quad (4)$$

with the starting concentration c_0, the final concentration c_∞ and the diffusive relaxation time $\tau = \sigma^2/D$ with the width σ of the Gaussian temperature profile and diffusion coefficient D. For the series expansion, the constant K is defined by the zero of $(1-e^{-K})/K = c_\infty/c_0$. We use the formula for both the thermophoretic depletion and the backdiffusion by choosing appropriate starting and final conditions c_0 and c_∞. Due to the symmetry between thermal and mass diffusion, the heating and cooling kinetics can be modeled by the same equation according to $c \to T$ with a thermal relaxation time $\tau \to \tau_{\text{thermal}}$, approximated to $\tau_{\text{thermal}} = d^2/\kappa$ with the thermal diffusivity κ and the chamber thickness d. We can infer the fluorescence signal using the bleaching correction with time constant τ_{bleach}, the temperature dependence of the dye $\alpha = \partial F/\partial T$ and both the heating and cooling time points t_H, t_C. The laser is switched on with a step function $h(t) = \theta(t-t_H) * \theta(t_C - t)$, backdiffusion is timed by $b(t) = \theta(t-t_C)$ and the initial time before depletion switched on with $i(t) = \theta(t_H - t)$ where $\theta(t)$ defines Heavy-side functions. The depletion dynamics of concentration is given by $c_{\text{DEPL}}(t) = c(t-t_H,\tau,1,e^{-s_T\nabla T})$ with a temperature sensitive fluorescence given by the thermal relaxation $T_{\text{HEAT}}(t-t_H,\tau_{\text{thermal}},1,1+\alpha\Delta T)$. Likewise the back diffusion dynamics is modeled by $c_{\text{DIFF}}(t) = c \times (t-t_C,\tau,c_{\text{DEPL}}(t_C-t_H),1)$ under a cooling dynamics of $T_{\text{COOL}}(t-t_C\tau_{\text{thermal}},1+\alpha\Delta T,1)$. Since thermal diffusivity is typically 100–1000 times faster, we can assume $\tau \gg \tau_{\text{thermal}}$ and superpose the thermal and mass diffusion dynamics by separating the time scales. With the initial fluorescence F_0 and the bleaching dynamics, the measured fluorescence then becomes:

$$F(t) = [c_{\text{DEPL}}(t)T_{\text{HEAT}}(t)h(t) + c_{\text{DIFF}}(t)T_{\text{COOL}}(t)b(t) + i(t)]F_0 e^{t/\tau_{\text{bleach}}}. \quad (5)$$

As expected, the analytical solution does not differ from the one-dimensional finite element solution under Gaussian heating. However, the common deviations of the thermal profile from the Gaussian shape render the above analytical treatment only an approximation. Also, it is restricted to the dynamics in the heating center, not the fluorescence surrounding of the heated spot which is often used to check the details of the diffusion dynamics. Notably, the same criticism concerning the applicability of the 1-D finite element solution in confined capillary geometries applies (Fig. 4A). However for fast fitting purposes, the approach has its validity.

The real temperature profile as measured by fluorescence is neither exactly Gaussian nor Lorentzian. Hence, it was important to independently quantify the temperature distribution with a spacial resolution below 1.5 μm (Section 2). The profile is incorporated into the model as a fitted polynomial of the order of 15, which allowed sufficient precision (<1%) to describe the temperature profile in both shape and magnitude.

The recorded fluorescence images were analyzed by Labview routines (National Instruments, Austin, TX, USA). All images were normalized to the first ten images where no temperature gradient is present. The resulting signal is thereby corrected against minor illumination inhomogeneities of the microscope. The temperature dependence of the fluorescence of the dye is determined in independent measurements using the temperature controlled Peltier stage and was found to be small (0.0%/*K*–0.24%/*K*). This value varies for different DNA length and salt concentrations and affects the measurement only slightly; however, it was determined independently for every measurement condition. We correct for this by subtracting the temperature dependence on a pixel-by-pixel basis according to the temperature distribution present in solution. This is carried out 100 ms after the IR laser is turned on since simulations have shown that at this time the temperature gradient is equilibrated throughout the capillary while the thermophoresis of the temperature dye itself is not yet significant [23, 24]. Photobleaching results in an exponential decay of fluorescence signal over time and is accounted for by dividing the signal by $\exp(t/\tau)$, where t is time and τ is the characteristic timescale of bleaching which is fitted. As a result, we can infer the DNA concentration from the fluorescence intensity. This trace of DNA concentration over time can be directly compared with simulated time traces.

Numerical evaluation of the model was carried out on the basis of Matlab (MathWorks, Natick, MA, USA). The model structure, together with the solving algorithms, for the differential equations was provided by Femlab. Simulated and measured time lines were compared using a Labview program. Here, the traces of DNA concentration over time obtained from the fluorescence signal were compared with theoretical time traces from FEMLab simulations using sample specific parameters provided by the Labview routine. The only fitted parameters were the Soret coefficient S_T and the diffusion constant D. By varying both, the simulated time lines were fitted to the measured time lines. In Fig. 5A the result of this process is shown for time lines obtained for different positions along the capillary, starting at the heating center, going outward parallel to the capillary walls. Simulated and measured temporal evolutions of relative concentration of DNA at different positions in the capillary are in good agreement. As would be expected, the thermophoretic depletion is strongest in proximity of the heating center ($x = 3$ μm) and becomes smaller as distance increases ($x = 20$ μm). The temporary increase in concentration at large distances from the center ($x = 60$ μm) originates from molecules moving away from the hot spot, an effect which is more prominent in the confined capillary geometry as compared with previously used two dimensional fluid films [1, 11]. Likewise, the evaluation of the concentration distributions along the capillary axis at given times shows good agreement between theory and measurement (Fig. 5B). Besides selected spatial and

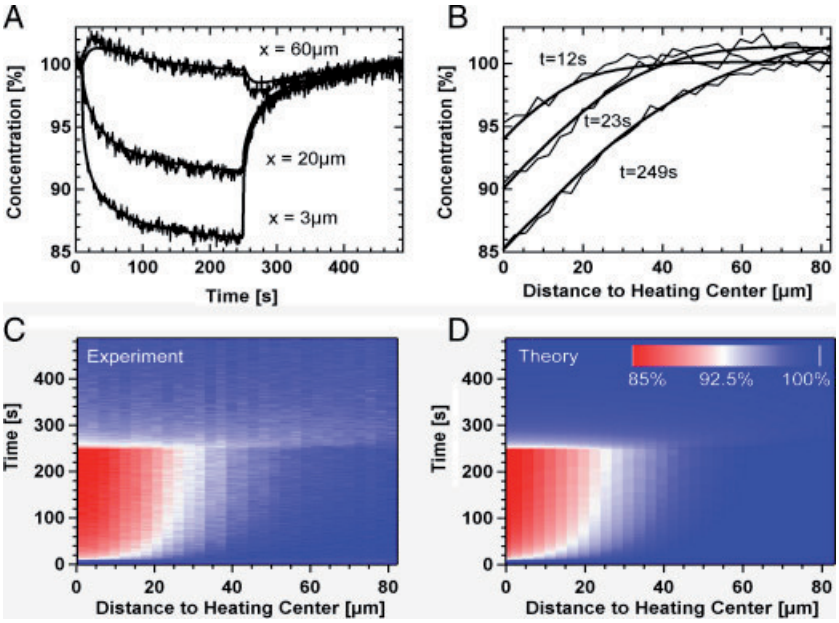

Figure 5. Thermophoresis in experiment and theory. Comparison of measurements and simulations for a 50-base Single stranded DNA molecule at a Debye length of $\lambda_{DH} = 3.7$ nm. (A) Change of the concentration over time is evaluated at different positions along the capillary. (B) Concentration profiles parallel to the capillary at its center at specific times are well described by the simulated concentration profiles using the 2-D model. (C, D) The concentration in a space–time plot of the thermophoretic depletion is represented by colors. The experimental space–time (C) is well described by the theoretical space–time (D). Note that the information represented in (A) and (B) are vertical and horizontal cross sections of the space–time plot at fixed values of distance or time, respectively.

temporal cross sections, we can also visualize the concentration in a space–time graph, demonstrating the fine agreement between measurements (Fig. 5C) and simulations (Fig. 5D) for all measured times and distances.

3 Results and discussion

The Soret coefficient of single stranded DNA molecules of 5, 10, 22 and 50 bases length, diluted to a concentration of 1 µM, was measured in solution as a function of salt concentration. The Debye shielding length is inversely proportional to the square root of salt concentration. The solution was buffered with 1 mM Tris at pH 7.6. Salt concentrations in the range between 2 and 500 mM KCl were investigated. This range corresponds to Debye shielding lengths of 5.6 and 0.43 nm, respectively. Values for D and S_T were obtained by fitting the measured data in a spacial-temporal manner as shown in Fig. 5. Soret coefficients scale linearly with Debye length for all molecules with a small intercept at $\lambda_{DH} = 0$ (Fig. 6A). The diffusion constant decreases with increasing oligonucleotide length and is well fitted by a power law $D \sim (\text{bases})^{-0.45}$ (Fig. 6B).

The Soret coefficient of double stranded DNA down to a length of 50 bases has been previously derived as

$$S_T = \frac{A}{k_B T} \frac{\beta \sigma_{eff}^2}{4\varepsilon\varepsilon_0 T} \lambda_{DH} + S_T^{Off} \qquad (6)$$

without free parameters [1]. Here, $\sigma_{eff} = Q_{eff}/A$ is the effective charge *per* surface area and ε and ε_0 the permittivity of water and free space, respectively. The parameter β contains the temperature dependence of both the permittivity of water [25] and the Debye length: $\beta = 1(T/\varepsilon)(d\varepsilon/dT)$. The central term is the entropy of ionic shielding and is calculated from the temperature derivative of the Gibbs Free Enthalpy of the ionic shielding for thin Debye layers $G_{ionic} = Q_{eff}^2 \lambda_{DH}/2(\varepsilon\varepsilon_0 A)$. In a simplified picture, this contribution can be interpreted as electrical energy stored in a capacitor consisting of the molecule's surface charges on the one side, separated against the shielding ions in solution on the other side.

The offset value S_T^{Off} will be fixed when evaluating the experiments. It includes from a theoretical perspective a size independent "ideal gas" contribution $S_T^B = 1/T$ that stems from work against the osmotic pressure [11]. However, its contribution is rather small ($S_T^B = 0.0034\ K^{-1}$) and should contribute only significantly for small molecules measured at large salt concentrations. Another contribution to the offset is the hydrophobic interaction with water. It is expected to be salt independent for the comparably low salt concentrations in our experiments and is modeled by $-A\, s_{hyd}/k_B T$ where s_{hyd} is the hydration entropy *per* molecule surface area A and $k_B T$ the thermal energy. It accounts for the change in water structure due to the presence of the single stranded DNA molecules, including, for example, the creation of the water cavity for the molecule and the hydrophobic interactions at its interface. In principle, we could separate the "ideal gas" contribution from contributions stemming from s_{hyd} by size dependent measurements of the offset in a $S_T(\lambda_{DH})$ plots. However experimental errors prevent such analysis at least in the measurements presented here.

Based on electrophoresis measurements, the effective charge of single stranded DNA is about 0.5e/base [26–28], considerably higher than the value for double stranded DNA. The theory of counterion condensation predicts an effective

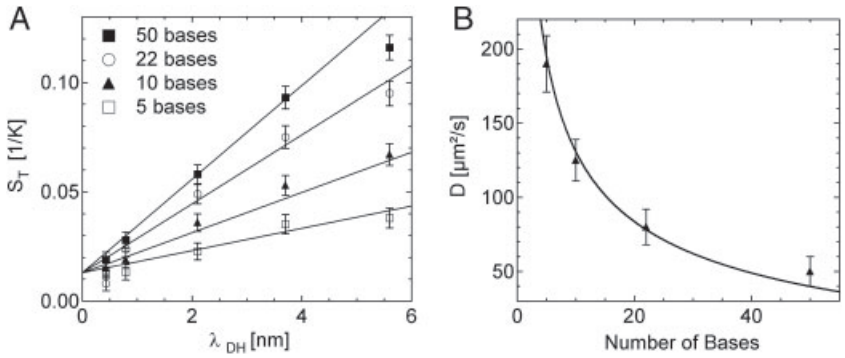

Figure 6. Salt dependence. (A) The Soret coefficient S_T *versus* Debye length for single stranded DNA ranging from 5 to 50 bases in length. The linear increase is quantitatively described by Eq. (6) with $Q_{eff} = 0.5e$/base without fitting parameters other than the comparably small offset at zero Debye length. (B) Diffusion coefficients for the DNA molecules obtained from the same measurement. Values are well fitted with a power law $D \sim \text{bases}^{-0.45}$.

charge of $0.6e$/base for single stranded DNA [29, 30]. These values do not depend on salt concentration in the range investigated here and were shown to be largely temperature insensitive. The surface area of the molecules was approximated to be spherical with a radius inferred from the measured diffusion coefficients according to the Stokes–Einstein relation $r = k_B T/(6\pi\eta D)$. Measurements performed on longer single stranded DNA fragments (280-5386 bases) yields a persistence length ranging from 1 to 5 nm for salt concentrations in the 10^{-1} to the 10^{-3} M regime [31, 32]. Assuming a polymer length of 1.5 nm for the 5-mer, the persistence length is longer than polymer length for most measurements. But given a width of about 1 nm for single stranded DNA, a spherical approximation is still feasible. One should note that for the measurements under low salt and short DNA, we are at the boundary of the applicable range of Eq. (6), working rather in the regime $R \geq \lambda_{DH}$ than strictly under $R \gg \lambda_{DH}$ necessary for the capacity model. Nevertheless, the theory describes the behavior of short Single stranded DNA molecules quite well.

As shown in Fig. 6A, the linear increase of S_T for single stranded DNA is described well by Eq. (6). Besides an offset of $S_T^{Off} = 0.013K^{-1}$, no fitting parameters were used and the Soret coefficients were described microscopically from first principles. The offset is comparably small and probably of complex origin and nature. For single stranded DNA, a free fit of the offset shows no systematic dependence on the DNA length. In previous experiments using polystyrene beads with considerably larger Soret coefficients, a similar offset was found which however scaled – within experimental errors – with the particle surface [1]. For each measurement point, the measured diffusion coefficient was used to infer the molecule size. Similar to polystyrene beads, the linear dependence on the Debye thickness is not only confirmed but also predicted quantitatively from a microscopic picture of charge screening.

The change of the salt concentration did not systematically change the size of the ssDNA molecules in the measured salt range and allowed the direct linear plot of the Soret coefficient based on Eq. (6). The measured diffusion coefficients are shown in Fig. 6B and are in fair agreement with literature values [31, 32] considering that for short single stranded DNA the fluorescent label cannot be neglected and will result in a slightly reduced diffusion coefficient. Diffusion constants are fitted with a power function. Including a minor offset we find D proportional to $L^{-0.45}$ with L denoting the number of bases.

It follows from the results of Fig. 6A that the length dependence of the thermophoresis of single stranded DNA should be predictable as well. Starting with a fixed offset $S_T^{Off} = 0.013K^{-1}$ and interpolating the diffusion coefficient from the power law fit of Fig. 6B, we can directly infer the length dependence of the Soret coefficient without introducing additional external parameters (Fig. 7). We see that the measured Soret coefficients are fairly well predicted by Eq. (6) as a function of DNA length at various salt concentrations.

To demonstrate the potential of thermophoresis for highly sensitive length discrimination, let us consider the difference between a 25-mer and a 26-mer of single stranded DNA. The difference in their respective Soret coefficients ΔS_T can be approximated from the total differential of Eq. (6). By using the dependence $A \propto D^{-2}$ and $Q_{eff} = A\sigma_{eff}$ together with differences in the charge ΔQ_{eff} and the diffusion coefficient ΔD we get:

$$\Delta S_T/S_T = 2\Delta Q_{eff}/Q_{eff} + 2\Delta D/D. \quad (7)$$

With a change $\Delta D/D = -0.028$ inferred from Fig. 6B and $\Delta Q_{eff}/Q_{eff} = 1/25$ we can expect a relative change of the Soret coefficient of $\Delta S_T/S_T = 0.024$. Measurements of the Soret coefficient with a comparably low error can be achieved. Single nucleotide resolution was shown utilizing a calibration curve approach (Wienken, C. J. *et al.*, submitted). High-resolution thermophoresis was also used to monitor the binding of a single ATP to the DNA (Baaske, P. *et al.*, submitted). We expect applications of the technique where an exact length determination of short DNA molecules is sought-after, *e.g.* for detecting short tandem repeats or single nucleotide polymorphisms in DNA analytics.

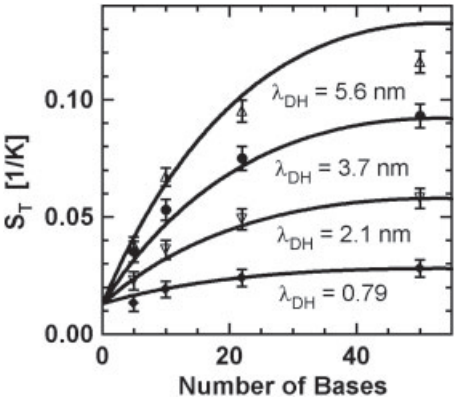

Figure 7. Length dependence. The Soret coefficient as a function of DNA length calculated from Eq. (6) with the interpolated diffusion coefficient obtained from Fig. 6B. The measured S_T values match well the theoretical expectations for various salt concentrations, indicated by the respective Debye lengths.

4 Concluding remarks

Capillaries are found to be highly reliable and non-sticky microfluidic environments for the optical investigation of thermophoresis in solution. Only small sample volumes (<250 nL) are required while the experiments are highly reproducible due to the well-defined chamber geometry of the capillaries. The thermophoretic depletion of single stranded DNA, driven by a local increase in temperature of only a few Kelvins, is monitored by fluorescence in detail and well described by 2-D simulations. As a side effect diffusion coefficients of the molecules are obtained from the experiments. Interestingly, the microscopic theory of thermophoresis based on a local thermodynamic equilibrium describes the thermophoresis of single stranded DNA – besides a small and expected offset – without fitting parameters. We find the expected linear dependence of the Soret coefficient on the Debye length without free parameters. At all considered salt concentrations the dependence of the Soret coefficient on DNA length is highly predictable.

The authors thank Ricky Dunbar and Franz Weinert for proofreading the manuscript and Inga Tegtmeier for creating Figs. 1A and B. Further we thank NanoTemper Technologies GmbH for fruitful discussions concerning the experimental setup. We also thank for the support from the Emmy-Noether Program of the Deutsche Forschungsgemeinschaft, the LMU Innovative Initiative on Functional NanoSystems (FUNS), the Excellence Cluster NanoSystems Initiative Munich (NIM) and the Center for Nanoscience (CeNS).

The authors have declared no conflict of interest.

5 References

[1] Duhr, S., Braun, D., *Proc. Natl. Acad. Sci. USA* 2006, *103*, 19678–19682.

[2] Braun, D., Libchaber, A., *Phys. Rev. Lett.* 2002, *89*, 188103.

[3] Iacopini, S., Piazza, R., *Europhys. Lett.* 2003, *63*, 247–253.

[4] Clusius, K., Dickel, G., *Naturwissenschaften* 1938, *26*, 546.

[5] Debye, P., *Ann. Phys.* 1939, *36*, 284–294.

[6] Braun, D., Libchaber, A., *Phys. Rev. Lett.* 2002, *89*, 188103.

[7] Duhr, S., Braun, D., *Phys. Rev. Lett.* 2006, *97*, 038103.

[8] Baaske, P., Weinert, F. M., Duhr, S., Lemke, K. H., Russell, M. J., Braun, D., *Proc. Natl. Acad. Sci.* USA 2007, *104*, 9346–9351.

[9] Dhont, J. K. G., *J. Chem. Phys.* 2004, *120*, 1632.

[10] Dhont, J. K. G., *J. Chem. Phys.* 2004, *120*, 1642.

[11] Dhont, J. K. G., Wiegand, S., Duhr, S., Braun, D., *Langmuir* 2007, *23*, 1674–1683.

[12] Astumian, R. D., *Proc. Natl. Acad. Sci. USA* 2007, *104*, 3–4.

[13] Astumian, R. D., *J. Chem. Phys.* 2007, *126*, 111102.

[14] Weinert, F. M., Braun, D., *Phys. Rev. Lett.* 2008, *101*, 164501.

[15] Duhr, S., Braun, D., *Phys. Rev. Lett.* 2006, *96*, 168301.

[16] Ning, H., Buitenhuis, J., Dhont, J. K. G., Wiegand, S., *J. Chem. Phys.* 2006, *125*, 204911.

[17] Dhont, J. K. G., Briels, W. J., *Eur. Phys. J.* 2008, *25*, 61–76.

[18] Piazza, R., Vigolo, D., Braibanti, M., *Phys. Rev. Lett.* 2008, *100*, 108303.

[19] Putnam, S. A., Cahill, D. G., *Langmuir* 2005, *21*, 5317–5323.

[20] Würger, A., *Phys. Rev. Lett.* 2008, *101*, 108302.

[21] Yguerabide, J., Schmidt, J. A., Yguerabide, E. E., *Biophys. J.* 1982, *39*, 69–75.

[22] Axelrod, D., Koppel, D. E., Schlessinger, J., Elson, E., Webb, A. W., *Biophys. J.* 1976, *16*, 1055–1069.

[23] Baaske, P., Duhr, S., Braun, D., *Appl. Phys. Lett.* 2007, *91*, 133901.

[24] Cordero, M. L., Verneuil, E., Gallaire, F., Baroud, C. N., *Phys. Rev. E* 2009, *79*, 011201.

[25] Hill, N. E., *J. Phys. C* 1969, *3*, 238–239.

[26] Michalet, X., *Nano Lett.* 2001, *1*, 341–343.

[27] Shen, G., Tercero, N., Gaspar, M. A., Varughese, B., Shepard, K., Levicky, R., *J. Am. Chem. Soc.* 2006, *128*, 8427–8433.

[28] Stigter, D., *Biophys. J.* 1995, *69*, 380–388.

[29] Record, M. T., Anderson, C. F., Lohman, T. M., *Quart. Rev. Biophys.* 1978, *11*, 103178.

[30] Manning, G. S., *Q. Rev. Biophys.* 1978, *11*, 179–246.

[31] Nkodo, A. E., Garnier, J. M., Tinland, B., Ren, H. J., Desruisseaux, C., McCormick, L. C., Drouin, G., Slater, G. W., *Electrophoresis* 2001, *22*, 2424–2432.

[32] Tinland, B., Pluen, A., Sturm, J., Weill, G., *Macromolecules* 1997, *30*, 5763–5765.

Bioanalytical Chemistry

DOI: 10.1002/anie.200903998

Optical Thermophoresis for Quantifying the Buffer Dependence of Aptamer Binding**

Philipp Baaske, Christoph J. Wienken, Philipp Reineck, Stefan Duhr, and Dieter Braun*

Quantification of biomolecular binding reactions in their native environment is crucial for biology and medicine. However, reliable methods are rare. We have developed a new immobilization-free method in which thermophoresis, the movement of molecules in a thermal gradient, is used to determine binding curves; this method can be used to study binding in various buffers as well as in human blood serum. The assay does not rely on surface contact and requires only an unspecific fluorescence marker on one of the binding partners.

Aptamers are nucleic acid ligands selected in vitro for their ability to bind to specific molecular targets.[1–4] They are promising candidates for diagnostic applications because of their affinity and specificity—comparable to that of antibodies—and the ease with which novel aptamers can be designed.[5] Aptamers have been implemented in a variety of sensing technologies[6] including optical approaches like "aptamer beacons",[7] electronic-sensing strategies,[8] and techniques based on changes in mass[9] or force.[10]

In most aptamer-based binding assays, the signal transduction mechanism depends on the molecular recognition mechanism. As a result the aptamers must be designed not only to adopt an appropriate conformation to bind to a target (recognition) but also to undergo a binding-induced conformational change, which affects the fluorescence of a dye[8] or the electron transfer[9] of a redox tag to an electrode (signal transduction). This linkage between target recognition and signal transduction sets obstacles for the design of aptamers. Often aptamers must be modified with two labels, which results in reduced binding affinity or even complete suppression of binding.[11] These restrictions can be reduced by separating the molecular recognition from the signal transduction by using additional competitor oligonucleotides, complementary to the aptamer, as signal transduction elements.[12]

[*] P. Baaske, C. J. Wienken, P. Reineck, Prof. D. Braun
Ludwig-Maximilians-Universität München
Systems Biophysics, Department of Physics
Center for NanoScience (CeNS), 80799 Munich, (Germany)
P. Baaske, S. Duhr
NanoTemper Technologies GmbH
Amalienstrasse 54, 80799 Munich (Germany)
Fax: (+49) 89-21801-6558
E-mail: philipp.baaske@nanotemper.de
Homepage: http://www.nanotemper.de

[**] We thank the LMU Innovative Initiative Functional NanoSystem (FUNS) and the Excellence Cluster NanoSystems Initiative Munich (NIM) for financial support.

Supporting information for this article is available on the WWW under http://dx.doi.org/10.1002/anie.200903998.

Herein we describe a novel approach for the quantification of aptamer–target interactions which separate molecular recognition from signal transduction and require an aptamer with only one unspecific tag. In this way binding can be probed under physiological conditions, under diffusion in complex biological fluids.

The approach is based on the directed movement of molecules along temperature gradients, an effect termed thermophoresis.[13–16] A temperature difference in space ΔT leads to a depletion of the solvated biomolecule in the region of elevated temperature, quantified by the Soret coefficient S_T [Eq. (1)].

$$c_{hot}/c_{cold} = \exp(-S_T \Delta T) \quad (1)$$

Thermophoresis depends on the interface between molecule and solvent. Under constant buffer conditions, thermophoresis depends on the size, charge, and solvation entropy of the molecules[15,16] and is not dependent on the concentration of the probed molecule unless millimolar concentrations are reached.[17,18] The thermophoresis of an aptamer A typically differs significantly from that of an aptamer–target complex AT because of changes in size, charge, or solvation energy. We used this difference in the molecule's thermophoresis to quantify the binding of a 5.6 kDa aptamer to the protein thrombin (37 kDa) as well as the binding of a 8.3 kDa aptamer to AMP (0.3 kDa) and ATP (0.6 kDa) in titration experiments under constant buffer conditions. We found that binding affinities depend on the buffer conditions and that the binding constants determined in 10% and 50% serum differ significantly from those measured in buffer solution.

The thermophoretic movement of the fluorescently end-labeled aptamer is measured by monitoring the fluorescence distribution F inside a glass capillary, which contains 500 nL of sample, with an epifluorescence microscope (Figure 1a). The microscopic temperature gradient is generated by an IR laser (1480 nm); the light is focused into the capillary and strongly absorbed by water.[15,16,19] The temperature of the aqueous solution in the laser spot is raised by $\Delta T = 8$ K. Before the IR laser is switched on, a homogeneous fluorescence distribution F_{cold} is measured inside the capillary (Figure 1b). When the IR laser is switched on, two effects, on different timescales, contribute to the new fluorescence distribution F_{hot}. The thermal relaxation time is fast (roughly 50 ms) and induces a drop in fluorescence of the dye owing to its intrinsic temperature dependence. On the slower timescale of diffusion (roughly 10 s), the aptamers move from the locally heated region to the outer cold regions.[16,20] The local concentration of aptamers decrease in the heated region until it reaches a steady-state distribution (Figure 1b).

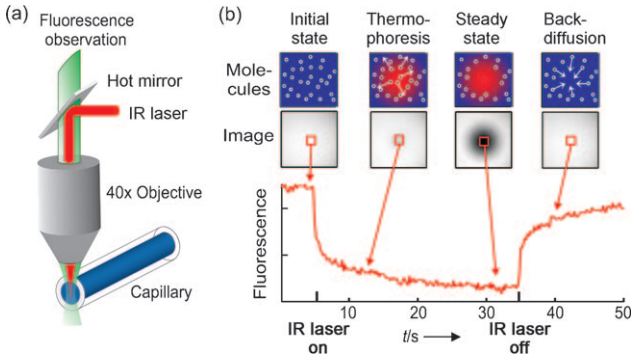

Figure 1. Thermophoresis assay. a) The blood serum inside the capillary is locally heated with a focused IR laser, which is coupled into an epifluorescence microscope using a heat-reflecting "hot" mirror. b) The fluorescence inside the capillary is imaged with a CCD camera, and the normalized fluorescence in the heated spot is plotted against time. The IR laser is switched on at $t = 5$ s, the fluorescence decreases as the temperature increases, and the labeled aptamers move away from the heated spot because of thermophoresis. When the IR laser is switched off, the molecules diffuse back.

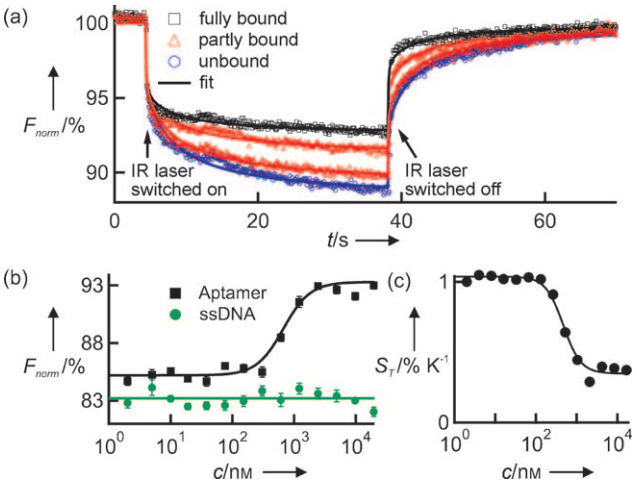

Figure 2. Aptamer–thrombin binding in 10% human serum. a) The thermophoretic depletion of unbound aptamer is about twice that of aptamers bound to thrombin. b) The normalized fluorescence F_{norm} at $t = 30$ s is plotted for different concentrations of thrombin (black). The thermophoresis of random 25-mer ssDNA (green) shows no dependence on thrombin concentration. c) The Soret coefficient S_T also reflects the binding; S_T was determined based on an analytical model of thermophoresis.[16]

While the molecular diffusion D dictates the kinetics of depletion, the Soret coefficient S_T describes the concentration ratio under steady-state conditions $c_{hot}/c_{cold} = \exp(-S_T \Delta T) \approx 1 - S_T \Delta T$ for a temperature increase ΔT.[15,16] The normalized fluorescence $F_{norm} = F_{hot}/F_{cold}$ measures mainly this concentration ratio, in addition to the temperature dependence of the dye fluorescence $\partial F/\partial T$. In the linear approximation we find: $F_{norm} = 1 + (\partial F/\partial T - S_T)\Delta T$.[16] Because of the linearity of the fluorescence intensity and the thermophoretic depletion, the normalized fluorescence from the unbound aptamer $F_{norm}(A)$ and the bound complex $F_{norm}(AT)$ superpose linearly. If x is used to denote the fraction of aptamers bound to targets, the changing fluorescence signal during the titration of target T can be given by Equation (2).

$$F_{norm} = (1-x)\,F_{norm}(A) + x\,F_{norm}(AT) \qquad (2)$$

Based on the capacitor model of thermophoresis,[15,21] confirmed for thin Debye layers in experiments using polystyrene beads,[15] double-stranded DNA,[15] single-stranded DNA,[16] and Ludox silica particles,[22] we can discuss the change in S_T expected from changes in charge Q_{eff} or hydrodynamic radius R upon binding. Assuming negligible offsets from non-ionic contributions, we find $S_T \propto (Q_{eff}/R)^2$. Under linear approximation, S_T changes by $\Delta S_T/S_T = 2(\Delta Q_{eff}/Q_{eff} - \Delta R/R)$. Only for the unlikely case that Q_{eff} is directly proportional to R would no change in S_T be expected. However, neglected contributions from solvation entropy[15] could contribute to binding even under these conditions.

We measured the thermophoresis of 100 nM thrombin aptamer labeled at the 5′ end with the fluorophore Cy5 [23] in 10% human serum (Figure 2). The concentration of thrombin ranges from 0 nM to 19500 nM. The low concentrations ensure that the serum and buffer do not change upon addition of thrombin and keep the thermophoresis of the aptamer constant. The observed time traces of the pure aptamer differ significantly from the traces of aptamers bound to thrombin (Figure 2a). Plotting the normalized fluorescence F_{norm} at a given time t against the thrombin concentration results in a binding curve (Figure 2b) with an EC_{50} value of 680 ± 80 nM and a Hill coefficient of 2. Control experiments with a randomly chosen sequence of ssDNA show no thrombin-dependent changes in either the thermophoretic signal (Figure 2b) or the absolute fluorescence, in either 10% or 50% serum. This indicates that neither interactions of thrombin with the Cy5 label, nor unspecific interactions of thrombin with ssDNA are present.

As detailed previously,[16] we used a two-dimensional finite element simulation to infer from the time traces the Soret coefficient S_T, the diffusion coefficient D, and the temperature dependence of the fluorescence $\partial F/\partial T$. The binding of the aptamer to thrombin mostly leads to a change in S_T, which decreases from 1.05% K^{-1} to 0.35% K^{-1} (Figure 2c). Owing to their linear relationship, F_{norm} and the S_T both report the binding (Figure 2b,c). Neither the temperature-dependent fluorescence change $\partial F/\partial T$ nor the diffusion coefficient D changed during the titration. Notably the determination of D is likely to be hampered by fitting crosstalk with $\partial F/\partial T$.

The thermophoretic perturbation creates a direct fluorescence ratio signal F_{norm} that reveals changes in the observed molecule that stem from changes in size, charge, or solvation entropy of the molecule. It does not rely on the notoriously difficult task of observing binding-induced size changes by measuring small changes in the diffusion coefficient D as, for example, in fluorescence correlation spectroscopy (FCS). As shown in Figure 3a, the approach can be used in buffers and equally well in complex biological liquids like blood serum without significantly loss of sensitivity or specificity as is the case with surface-based technologies such as surface plasmon resonance (SPR).

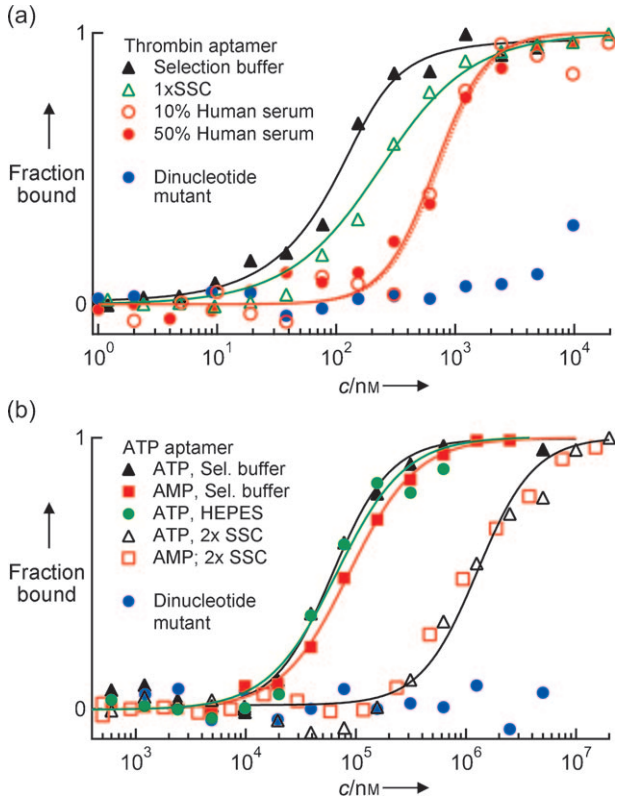

Figure 3. Binding curves in various buffers. a) Aptamer–thrombin binding in selection buffer, 1×SSC (sodium citrate) and in 10% and 50% untreated human serum. b) Aptamer binding to ATP and AMP in selection buffer, HEPES, and 2×SSC. The fraction of bound aptamers is derived according to Equation (2).

To further show the broad applicability of the thermophoretic quantification of binding, we also measured the binding of an aptamer to ATP and AMP[24] (Figure 3b) in different buffers. In all cases, binding was reported with a high signal-to-noise ratio (SNR), even in 50% human serum. For example, SNR = 93 was found for the binding of an aptamer to 0.3 kDa AMP in selection buffer, and SNR = 23 was found for the binding to thrombin in 50% human serum (see the Supporting Information). As control oligonucleotides we used DNA sequences that differed from the respective aptamer sequences in only two nucleotide mutations (Figure 3a,b "Dinucleotide mutant").

The dissociation constant $K_D = 30 \pm 19$ nM obtained for the aptamer–thrombin binding (Figure 3a) in selection buffer is in good agreement with the reported $K_D = 25 \pm 25$ nM[23] measured in the same buffer. However, Buff et al.[25] also reported slightly reduced binding affinity resulting from 5′-extensions of the thrombin–aptamer. In SSC buffer the dissociation constant increases to $K_D = 190 \pm 20$ nM and in 50% (10%) human serum the binding was best fitted with the Hill equation, yielding $EC_{50} = 720 \pm 100$ nM (670 ± 80 nM) and a cooperativity of $n = 2$.

The aptamer–ATP/AMP binding (Figure 3b) shows the cooperative binding of more than one ATP or AMP per aptamer, which is consistent with literature reports.[7,26] In the selection buffer, the EC_{50} values for ATP ($EC_{50} = 60 \pm 4$ μM) and AMP ($EC_{50} = 87 \pm 5$ μM) agree well with the reported values.[7,12] Measurements of the ATP binding in HEPES buffer ($EC_{50} = 67 \pm 8$ μM) confirm these results. In all cases the Hill coefficient was $n = 1.4$. Interestingly, in 2×SSC buffer, the EC_{50} values of the ATP/AMP–aptamer binding were both strongly shifted to lower affinities, resulting in $EC_{50} = 1100 \pm 100$ μM. Note that the ATP solutions were cooled to prevent hydrolysis of ATP.

As stated by Cho and Ellington,[6] the aptamer–target binding depends strongly on the chosen buffer: The binding of the aptamers in the respective selection buffers always showed the highest affinity (Figure 3). For aptamer–thrombin binding in human serum, the shift to lower affinities (EC_{50} = 720 nM) and enhanced cooperativity ($n = 1.5$) may be because of interactions of the thrombin with components of the blood serum. For ATP–aptamer binding the unexpected significant shift to lower affinities in the SSC buffer is likely an effect of a competing interaction of the strongly negative citrate^{3-} ion of the SSC buffer with the Mg^{2+} ions, as the latter are essential for aptamer–ATP/AMP binding.

In conclusion, we have developed a purely optical analytical method based on the thermophoresis of solvated molecules for the study of aptamer–target interactions in bulk solution. The sample volume is very low: 500 nL of which only 2 nL is probed. The signal transduction of binding is separated from the molecular recognition, which provides more freedom in the design of aptamers. The assay is robust and simple as no secondary reactions for detection are required. The dynamic range of the thermophoresis binding assay extends from nM to mM target concentrations, and the binding to low-mass targets such as AMP can also be quantified. The measurement can be performed in complex liquids such as blood and in simple standard buffers equally well. As a result, the approach will enable the determination of the affinity of aptamer-based drug candidates, for example spiegelmers,[27] in biological liquids under close to physiological conditions. The method is also applicable for screening new aptamers since the binding of unlabeled aptamers to a labeled target can also be quantified by thermophoresis.

Experimental Section

For imaging, we used a Zeiss Axiotech Vario microscope with a 40x Plan Fluar oil objective, numerical aperture 1.3. The fluorescence was excited with a red high-power LED Luxeon III (LXHL-LD3C). Fluorescence filters for Cy5 (F36–523) were purchased from AHF-Analysentechnik (Tübingen, Germany). Detection was provided with the Sensicam EM CCD camera from PCO AG (Kelheim, Germany). Fused-silica capillaries from Polymicro Technologies (Phoenix, USA) with an inner diameter of 100 μm and a volume of about 500 nL were used for the measurements.

The temperature gradients were created with an IR laser diode (Furukawa FOL1405-RTV-617-1480, $\lambda = 1480$ nm, $\kappa = 320$ μm for water, 320 mW maximum power) purchased from AMS Technologies AG (Munich, Germany). The IR laser beam was coupled into the path of fluorescence light with a heat-reflecting "hot" mirror (NT46-386) from Edmund Optics (Barrington, USA) and is focused into the fluid with the microscope objective. The temperature inside the capillary was measured by the known temperature-dependent fluorescence of the TAMRA dye.[19] The temperature in the solution

was increased by 8 K in the beam center with a $1/e^2$ diameter of 25 μm. All measurements were performed at room temperature.

The changes in fluorescence were analyzed in a region around the center of heating with a diameter of about 50 μm. The images were corrected for background and bleaching of the fluorescence.[16,20]

The human α-thrombin was purchased from Haematologic Technologies Inc. (Essex Junction, USA; specific activity 3593 U mg^{-1}; MW = 36.7 kDa). Human serum, AMP, and ATP were purchased from Sigma Aldrich (Munich, Germany).

The labeled DNA oligonucleotides were synthesized by Metabion (Martinsried, Germany). The sequences of the oligonucleotides, with mutations as small letters, are: Thrombin aptamer: 5′-Cy5-TGGTTGGTGTGGTTGGT-3′; thrombin dinucleotide mutant: 5′-Cy5-TGGTTGtTGTGGTTtGT-3′; ATP aptamer: 5′-Cy5-CCTGGGGGAGTATTGCGGAGGAAGG-3′; ATP aptamer dinucleotide mutant: 5′-Cy5-CCTtGGGGAGTATTGCGGAtGAAGG-3′; ssDNA: 5′-Cy5-TAGTTCTAATGTGTATCTCAATTTT-3′.

Measurements were conducted in the following buffers: Thrombin–aptamer: Selection buffer:[23] 20 mM Tris-HCl pH 7.4, 150 mM NaCl, 5 mM KCl, 1 mM $CaCl_2$, 1 mM $MgCl_2$, 0.01 % TWEEN20, 4 % BSA. For the human serum measurements this buffer was mixed 1:1 with 100 % human serum. 1 × SSC: 15 mM sodium citrate, pH 7.4, 150 mM NaCl, 5 mM KCl, 1 mM $CaCl_2$, 1 mM $MgCl_2$, 0.01 % TWEEN20, 4 % BSA. ATP–aptamer: Selection buffer:[24] 20 mM Tris-HCl pH 7.6, 300 mM NaCl, 5 mM $MgCl_2$ and 0.01 % TWEEN20. 2 × SSC: 30 mM sodium citrate, pH 7.4, 300 mM NaCl, 5 mM $MgCL_2$, 0.01 % TWEEN20. HEPES: 20 mM HEPES pH 7.5, 300 mM NaCl, 5 mM $MgCl_2$, and 0.01 % TWEEN20. For ATP the pH of the buffers was measured for different ATP concentrations with the pH-sensitive dye BCECF (see the Supporting Information).

The aptamer and the mutant concentrations were maintained at 100 nM (thrombin–aptamer) and 500 nM (ATP–aptamer) during all experiments. The aptamers were denatured and renatured prior the experiments to ensure that they reached their active conformation. The solutions were incubated for 2 h after the oligonucleotides had been mixed with the different target molecules.

The K_D values for thrombin were obtained by fitting the fraction of bound aptamers to the quadratic solution of the binding reaction equilibrium, derived from the law of mass action, with K_D as single free parameter.[11] The EC_{50} values were obtained from fitting the binding curves with the Hill equation (see the Supporting Information).

Received: July 20, 2009
Published online: ■■ ■■, 2010

Keywords: aptamers · DNA · drug discovery · immobilization-free methods · proteins

[1] G. Mayer, *Angew. Chem.* **2009**, *121*, 2710 – 2727; *Angew. Chem. Int. Ed.* **2009**, *48*, 2672 – 2689.
[2] A. D. Ellington, J. W. Szostak, *Nature* **1990**, *346*, 818 – 822.
[3] C. Tuerk, L. Gold, *Science* **1990**, *249*, 505 – 510.
[4] D. L. Robertson, G. F. Joyce, *Nature* **1990**, *344*, 467 – 468.
[5] B. Boese, K. Corbino, R. Breaker, *Nucleosides Nucleotides Nucleic Acids* **2008**, *27*, 949 – 966.
[6] E. Cho, J. Lee, A. Ellington, *Annu. Rev. Anal. Chem.* **2009**, *2*, 241 – 264.
[7] S. Jhaveri, R. Kirby, R. Conrad, E. Maglott, M. Bowser, R. Kennedy, G. Glick, A. Ellington, *J. Am. Chem. Soc.* **2000**, *122*, 2469 – 2473.
[8] Y. Xiao, A. A. Lubin, A. J. Heeger, K. W. Plaxco, *Angew. Chem.* **2005**, *117*, 5592 – 5595; *Angew. Chem. Int. Ed.* **2005**, *44*, 5456 – 5459.
[9] S. Song, L. Wang, J. Li, C. Fan, J. Zhao, *TrAC Trends Anal. Chem.* **2008**, *27*, 108 – 117.
[10] D. Ho, K. Falter, P. Severin, H. E. Gaub, *Anal. Chem.* **2009**, *81*, 3159 – 3164.
[11] S. Beyer, W. Dittmer, F. Simmel, *J. Biomed. Nanotechnol.* **2005**, *1*, 96 – 101.
[12] N. Li, C. M. Ho, *J. Am. Chem. Soc.* **2008**, *130*, 2380 – 2381.
[13] C. Ludwig, *Sitzungsber. Akad. Wiss. Wien Math.-Naturwiss. Kl.* **1856**, *20*, 539.
[14] S. Iacopini, R. Piazza, *Europhys. Lett.* **2003**, *63*, 247 – 253.
[15] S. Duhr, D. Braun, *Proc. Natl. Acad. Sci. USA* **2006**, *103*, 19678 – 19682.
[16] P. Reineck, C. J. Wienken, D. Braun, *Electrophoresis* **2010**, *31*, 279 – 286.
[17] J. K. G. Dhont, *J. Chem. Phys.* **2004**, *120*, 1632 – 1641.
[18] J. Rauch, W. Köhler, *J. Chem. Phys.* **2003**, *119*, 11977 – 11988.
[19] P. Baaske, S. Duhr, D. Braun, *Appl. Phys. Lett.* **2007**, *91*, 133901.
[20] S. Duhr, S. Arduini, D. Braun, *Eur. Phys. J. E* **2004**, *15*, 277 – 286.
[21] J. K. G. Dhont, S. Wiegand, S. Duhr, D. Braun, *Langmuir* **2007**, *23*, 1674 – 1683.
[22] H. Ning, J. K. G. Dhont, S. Wiegand, *Langmuir* **2008**, *24*, 2426 – 2432.
[23] L. C. Bock, L. C. Griffin, J. A. Latham, E. H. Vermaas, J. J. Toole, *Nature* **1992**, *355*, 564 – 566.
[24] D. E. Huizenga, J. W. Szostak, *Biochemistry* **1995**, *34*, 656 – 665.
[25] M. C. R. Buff, F. Schäfer, B. Wulffen, J. Müller, B. Pötzsch, A. Heckel, G. Mayer, *Nucleic Acids Res.* **2009**, DOI: 10.1093/nar/gkp1148.
[26] C. H. Lin, D. J. Patel, *Chem. Biol.* **1997**, *4*, 817 – 832.
[27] C. Maasch, K. Buchner, D. Eulberg, S. Vonhoff, S. Klussmann, *Nucleic Acids Symp. Ser.* **2008**, *52*, 61 – 62.

Communications

Bioanalytical Chemistry

P. Baaske,* C. J. Wienken, P. Reineck, S. Duhr, D. Braun ——— ■■■■–■■■■

Optical Thermophoresis for Quantifying the Buffer Dependence of Aptamer Binding

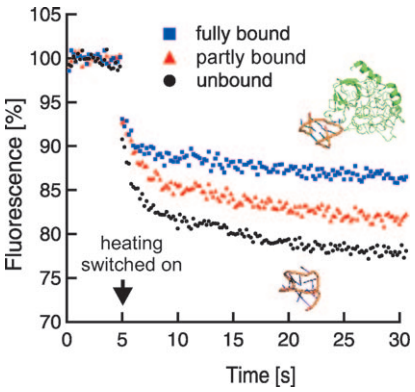

Some like it hot: A robust and fast method for characterizing aptamers relies on the distinct thermophoretic movements of molecules in microscopic temperature gradients (see diagram). The binding properties of proteins and even small molecules can be measured within seconds, and less than 1 μL of sample is required. Notably, the technique works well in complex liquids such as human serum.

nature COMMUNICATIONS

ARTICLE

Received 10 May 2010 | Accepted 20 Sep 2010 | Published 19 Oct 2010

DOI: 10.1038/ncomms1093

Protein-binding assays in biological liquids using microscale thermophoresis

Christoph J. Wienken[1], Philipp Baaske[1,2], Ulrich Rothbauer[3], Dieter Braun[1] & Stefan Duhr[1,2]

Protein interactions inside the human body are expected to differ from the situation *in vitro*. This is crucial when investigating protein functions or developing new drugs. In this study, we present a sample-efficient, free-solution method, termed microscale thermophoresis, that is capable of analysing interactions of proteins or small molecules in biological liquids such as blood serum or cell lysate. The technique is based on the thermophoresis of molecules, which provides information about molecule size, charge and hydration shell. We validated the method using immunologically relevant systems including human interferon gamma and the interaction of calmodulin with calcium. The affinity of the small-molecule inhibitor quercetin to its kinase PKA was determined in buffer and human serum, revealing a 400-fold reduced affinity in serum. This information about the influence of the biological matrix may allow to make more reliable conclusions on protein functionality, and may facilitate more efficient drug development.

[1] Department of Physics and Center for NanoScience (CeNS), Ludwig-Maximilians-Universität München, Amalienstrasse 54, Munich 80799, Germany. [2] NanoTemper Technologies GmbH, Amalienstrasse 54, Munich 80799, Germany. [3] Biocenter at the Department of Biology II, Ludwig-Maximilians-Universität München, Grosshaderner Strasse 2, Martinsried 82152, Germany. Correspondence and requests for materials should be addressed to S.D. (email: Stefan.Duhr@physik.uni-muenchen.de).

Methods to analyse proteins and their interactions with other biomolecules or low-molecular-weight compounds are of great importance for the evaluation of cellular functions and for the development of pharmaceuticals. Potential drug candidates range from specifically designed antibodies to low-molecular-weight compounds that inhibit or activate cellular processes. Although there is a variety of *in vitro* approaches that can address particular interactions, there is a constant need for new techniques. In particular, the analysis of binding processes of small molecules and the general complications of making measurements in biological liquids remain significant challenges in modern bioanalytics.

Recent technological advances have indicated that thermophoresis could provide the means for such interaction analyses. Thermophoresis is the directed motion of molecules induced by temperature gradients. It was first discovered by Ludwig[1] and since then has been a subject of research mostly using inorganic molecules or polymer blends[2,3]. Braun and Libchaber[4], as well as Piazza[5], measured the thermophoresis of biomolecules to understand the intricacies of the effect[6–8]. Recently, Baaske *et al.*[9] showed that thermophoresis is capable of analysing DNA aptamer interactions with thrombin and ATP. Although these experiments demonstrate that it is possible to quantify interactions using thermophoresis, DNA aptamers are known for a strong thermophoretic effect due to their high charge[10]. Hence, the binding of the large protein thrombin or the highly charged ATP results in a strong thermophoretic response.

In this study, we introduce microscale thermophoresis (MST) as a tool to characterize protein and small-molecule interactions in buffers and biological liquids. Such analyses are usually difficult as the thermophoresis of proteins is generally weak. In addition, low-molecular-weight binders often do not significantly change the charge or size of a molecule, but only induce weak conformational changes on binding. Hence, the analysis of potential drug candidates is far more challenging. The results presented in this study, however, demonstrate that MST is highly suitable for these kinds of interaction studies. In contrast to existing techniques, MST works in free-solution and with low consumption of sample. It is an entirely optical method, which is contact-free and therefore minimizes contamination of the sample. A simple Mix&Read protocol renders complex preparations unnecessary. To show the wide applicability of MST, we quantified the dissociation constants of various protein interactions both in buffer and in solutions similar to the protein's native environment, namely, blood serum or cell lysate.

Results

Experimental approach. The experimental setup consists of an infrared laser coupled into the path of fluorescent excitation/emission using an infrared dichroic mirror (Fig. 1a). The laser is focused onto the sample through the same objective that is used for fluorescence detection. This allows the observation of thermohoresis in various microfluidic sample compartments such as capillaries or microfluidic channels. High reproducibility and low sample consumption are achieved using 100-µm-diameter glass capillaries with a total volume of about 500 nl. The infrared-laser creates a spatial temperature distribution on the length scale of 25 µm. The temperature increase scales linearly with the laser power. After 150 ms, laser heating and heat dissipation reach equilibrium, and a steady-state temperature increase of typically 2–6 K is obtained. This temperature rise induces a spatial concentration distribution that is visualized by a fluorescent dye covalently attached to one of the binding partners. Typically, one primary amine per protein is labelled and thus the position of the dye is statistically distributed. Given the number of lysines on a typical protein, the chance that the label interferes with the binding is very low. The majority of proteins are labelled far from the binding site, disturbing the interaction only minimally. To measure thermophoresis of proteins, the change

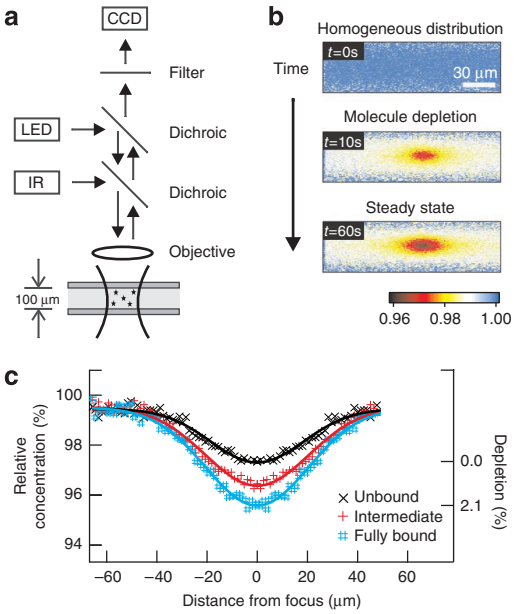

Figure 1 | Setup and principle of MST. (**a**) Experimental approach. With an additional dichroic mirror inserted into an epifluorescence microscope, a heating infrared-laser is focused into a fused silica capillary with an inner diameter of 100 µm. The sample fluorescence is imaged with a CCD camera. (**b**) Fluorescence images. Fluorescence images are acquired over time. Initially, fluorescently labelled molecules are distributed evenly. After switching on the heating with a focused infrared-laser, the molecules experience the thermophoretic force in the temperature gradient and typically move out of the heated spot. In the steady state, this molecule flow is counterbalanced by ordinary mass diffusion and a steady-state concentration profile is established. The colour code indicates the relative fluorescence in the sample. (**c**) Steady-state profiles. The steady-state profiles of human interferon-γ are plotted for various concentrations of a binding antibody (black ×: 0.1 nM, red plus sign: 80 nM, blue number sign: 500 nM). The depletion directly reflects the fraction of bound complex.

in concentration between the initial state and the steady state is measured. Therefore, two images of the sample are required: one image of the initial state before laser heating, showing a homogenous distribution of molecules, and a second image acquired after a few seconds of infrared-laser heating (Fig. 1b). This short measurement time is sufficient because of the fast mass diffusion over the small dimension of the temperature distribution. Even if the diffusion is slow and no steady state is reached within the measurement time, the concentration profiles are typically distinguishable after several seconds. Switching off the infrared-laser leads to a re-establishment of the initial homogeneous concentration profile by ordinary diffusion, providing information about the diffusion coefficient of the molecules[11].

To analyse binding events, the measurement is performed at various concentration ratios of the binding partners. Typically, the fluorescent binding partner is kept at a constant concentration and the unlabelled molecule is titrated until a saturation of all binding sites is obtained. Figure 1c shows the steady-state profiles of human interferon gamma (hIFN-γ) at various concentrations of a specific antibody. At low antibody concentrations, the profile reflects the thermophoresis of the unbound protein, whereas at high concentrations it indicates that of the complex. For intermediate concentrations, the measured depletion is a linear superposition of the bound and unbound states:

$$\Delta c_{\text{measured}} = f \cdot \Delta c_{\text{bound}} + (1-f) \cdot \Delta c_{\text{unbound}} \qquad (1)$$

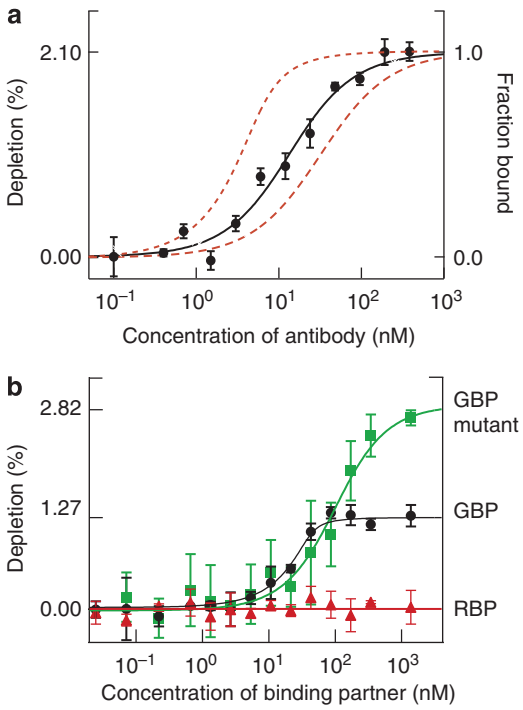

Figure 2 | Protein–protein interactions measured with MST. To determine the affinity of a binding reaction, a titration series of one binding partner is performed while the fluorescent binding partner is kept at a constant concentration. (**a**) The binding of fluorescently labelled hIFN-γ to a specific antibody is analysed with MST (black circles). The antibody is titrated from 100 pM to 700 nM. The change in the thermophoretic signal leads to a $K_d = 10 \pm 2$ nM. For comparison, the dashed lines show binding curves for 1 and 30 nM. (**b**) The interaction of the intrinsic fluorescent protein GFP with binders of varying affinities is measured. The GBP shows a high affinity of 2.3±2.1 nM (black circles), which is confirmed by a reference experiment on an Attana quartz crystal microbalance device. To ensure that the measured interaction truly represents specific binding, a GBP mutant (R37A) and non-binding RBP are further analysed with MST. The exchange of the arginine at the binding interface reduces the affinity to 80±38 nM (green squares), while the RBP shows the expected baseline (red triangles). The error bars represent the s.d. of each data point calculated from three independent thermophoresis measurements.

In Equation (1) $\Delta c_{measured}$ is the measured depletion, Δc_{bound} and $\Delta c_{unbound}$ represent depletion of the bound and unbound states, respectively, and f is the fraction of molecules in the bound state. The concentration change in the focal area can be directly transferred into a binding curve when plotted against the concentration of the added binding partner. From these data, the equilibrium dissociation constant K_d and a potential cooperativity can be determined.

Protein interactions. Specific interactions between proteins have a fundamental role in cellular functions and are important for biotechnological applications and antibody-based assays. In the following, we apply MST in several typical experiments to show its feasibility for use in interaction studies in the course of drug development or pharmaceutical research.

First, we determined the affinity of an antibody for its antigen analysing the interaction of an anti-IFN-γ antibody (120 kDa) with its antigen, hIFN-γ (17 kDa). hIFN-γ is a dimerized soluble cytokine that is crucial for immunity against intracellular pathogens and also for tumour control[12]. The hIFN-γ was labelled with AlexaFluor 647 and kept at a constant concentration of 5 nM in 1× phosphate-buffered saline (PBS) buffer at 5 °C. The antibody was titrated from 0.1 to 700 nM. On binding of the antibody, the thermophoretic concentration signal of hIFN-γ ranged from 2.14% for the unbound hIFN-γ to 4.24% for the bound complex, resulting in a differential depletion of 2.1% for the binding reaction. The level of depletion, as compared with the unbound state, versus the antibody concentration is plotted in Figure 2a. As discussed in the previous section, the depletion can be interpreted as a binding curve with the fraction of hIFN-γ in complex with its antibody plotted on the right axis. Fitting the data according to Equation (4) results in a dissociation constant of $K_d = 10 \pm 2$ nM. To show the high resolution of MST, we plotted the expected binding behaviour for $K_d = 1$ and 30 nM.

We further analysed a recently described interaction between green fluorescent protein (GFP) and a small antibody fragment known as GFP-binding protein (GBP)[13], which is derived from a single domain antibody of a Llama Alpaca (Fig. 2b). It was previously shown that GBP efficiently binds its antigen (GFP) in living cells as well as in immune-precipitation assays[13]. As GFP is intrinsically fluorescent, no fluorescent label was necessary to monitor the interaction. We prepared a titration series with a constant GFP concentration of 40 nM and varying amounts of GBP. The dissociation coefficient was determined to be $K_d = 2.3 \pm 2.1$ nM, which is 25-fold lower than the concentration of GFP. Still, determination was possible with fair accuracy by accounting for ligand depletion.

We directly compared the obtained K_d with affinity studies carried out on an Attana surface sensor instrument using a quartz crystal microbalance sensor (QCM). For this experiment, GBP was immobilized on the QCM surface and the on- and off-rates of GFP were determined, resulting in a dissociation constant of 0.63 nM. From a comparison of various interaction techniques, it is known that surface-based methods tend to overestimate the affinity of an interaction[14]. With this in mind, the affinities determined with MST and QCM are in good agreement. To determine whether the measured MST response represents specific binding, we analysed the interaction of a GBP carrying a mutation at its binding site. At position 37, an arginine was replaced by an alanine, which is known to reduce the binding affinity (see Supplementary Information). Furthermore, a non-binding protein, the red fluorescent protein (RFP)-binding protein (RBP), was analysed to exclude non-specific contributions. We found a binding affinity of 80±38 nM for the GBP mutant and no binding for RBP. Interestingly, the depletion changed from 1.27 to 2.82% for GBP and the GBP mutant (R37A), respectively. This is due to the fact that the thermophoretic amplitude not only depends on the size of the complex but also contains contributions from both charge and structure. By replacing a charged arginine by a structurally different and uncharged alanine, a resulting influence on the complex is very likely and can be observed in the thermophoretic amplitude.

Low-molecular-weight binding. The high sensitivity of thermophoresis for the binding of low-molecular-weight ligands is demonstrated by measuring the interaction of calmodulin (CaM, 16.7 kDa) with Ca^{2+} ions (Fig. 3a). CaM is the primary receptor for calcium ions in human cells, acting as a mediator of calcium functions and regulating many cellular processes[15]. Depending on its conformational state, CaM binds or regulates a multitude of protein targets. On binding to calcium, CaM undergoes a conformational change, rearranging more than 35 water molecules per CaM[16], which leads to a significant change in the thermophoretic properties. For analysing the binding behaviour, we performed a titration series from 1 nM to 50 μM Ca^{2+} ions, with 150 nM CaM kept constant throughout the series. We infer a dissociation constant of 2.8±0.2 μM and a cooperativity of 1.97±0.2. This value is in good agreement with the reported K_d values for CaM–Ca^{2+} in the affinity range from 1 to 10 μM[17]. As a control for specificity of the thermophoretic signal, a similar experiment was performed with Mg^{2+} ions instead of Ca^{2+} ions. Both ion species are equal in charge and similar in size. As no change in depletion was observed as a function of changing Mg^{2+}

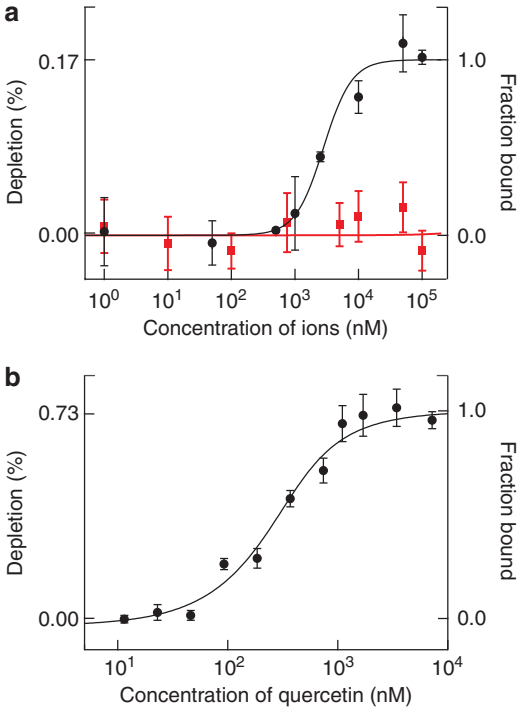

Figure 3 | Analysis of the binding of ions and small molecules. (**a**) Binding of Ca^{2+} ions to fluorescently labelled CaM is quantified in PBS buffer. The concentration of calcium ions was varied from 1 nM to 100 μM, while the concentration of the protein CaM was kept constant at 150 nM. To test for specificity of the interaction, the same titration series was performed with magnesium ions. For Ca^{2+}, we found a dissociation constant of $K_d = 2.8 \pm 0.2$ μM (black circles), whereas no binding was observed for Mg^{2+} ions (red squares). (**b**) The binding of the small, uncharged inhibitor quercetin to the cAMP-dependent kinase PKA is measured with MST (black circles). The titration of quercetin ranged from 11.5 nM to 50 μM with a constant concentration of the labelled kinase at 300 nM. Despite the small changes in the molecule's mass, a signal-to-noise ratio of 12.5 allows an accurate determination of the interaction strength. The affinity is determined to be 130 ± 30 nM, in good agreement with reported values. The error bars represent the s.d. of each data point calculated from three independent thermophoresis measurements.

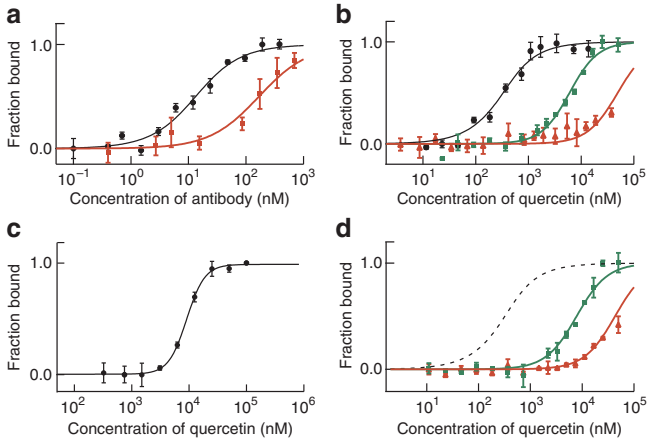

Figure 4 | Thermophoretic analysis of interactions in biological liquids. (**a**) The interaction of hIFN-γ with a specific antibody is analysed in buffer and compared with the same interaction in crude *E. coli* cell lysate. The affinity is shifted from 10 ± 2 nM in buffer (black circles) to 165 ± 26 nM in cell lysate (red squares). (**b**) The binding of the inhibitor quercetin to the cAMP-dependent kinase PKA is analysed in human serum. There, the apparent dissociation constant K_d changes from 0.13 ± 0.04 μM (black circles) to 6 ± 0.4 μM in 5% human serum (green squares) and to 50 ± 7 μM in 30% human serum (red triangles). (**c**) The binding of quercetin to the blood protein HSA is quantified using MST (black circles). The data yield a dissociation constant $K_d = 9.3 \pm 0.5$ μM and a cooperativity of 2.75 ± 0.2. (**d**) When using HSA concentrations corresponding to 5 and 30% human serum, a result comparable to the situation in real human serum was obtained. At a concentration of 32 μM HSA, the apparent affinity shifted to $K_d = 7.8 \pm 0.6$ μM (green squares), while at 190 μM HSA $K_d = 43 \pm 6$ μM (red triangles). The black dashed line represents the binding of quercetin to PKA in buffer. The error bars represent the s.d. of each data point calculated from three independent thermophoresis measurements.

concentration, non-specific binding was excluded and the specificity of calcium ion binding to CaM was confirmed.

The binding of an uncharged low-molecular-weight inhibitor to its target can also be analysed with MST. The cAMP-dependent kinase (PKA, 38 kDa) was analysed against the inhibitor quercetin (0.34 kDa; Fig. 3b). The kinase was fluorescently labelled and kept at a concentration of 300 nM. The inhibitor quercetin was titrated up to 50 μM in 50 mM HEPES buffer and 5% dimethyl sulphoxide (DMSO). We found an affinity of 130 ± 35 nM, which is in good agreement with the literature, where affinities of quercetin for various kinases are reported in the nanomolar to micromolar range[18,19]. In this experiment, the thermophoretic concentration signal changed from 3.8% for the unbound state to 4.53% for the bound state, showing a 19% relative change on binding of quercetin. As the mass of the bound complex differed by only 1% and charge contributions are unlikely, we attribute the large signal to changes in the hydration shell originating from water molecules that are either displaced from the binding pocket or reorganized when the protein undergoes conformational changes.

The experiments presented in this study demonstrate that MST is suitable for the analysis of low-molecular-weight binders. Owing to the high precision when analysing the thermophoretic signal, ion binding is still detectable with a signal-to-noise ratio of 5. In the case of quercetin binding, a signal-to-noise ratio of 12.5 was achieved, demonstrating that even minor changes are detectable with MST.

Competitive binding in cell lysate and serum. Today, analyses of protein interactions are typically performed in buffered salt solutions, which mimic natural conditions. However, these solutions lack many components that are present in the original biological liquid and that can have significant effects on the binding behaviour. An analysis in these artificial systems cannot provide precise information about the binding behaviour inside the human body and may lead to wrong decisions when developing drug candidates.

As shown below, MST can analyse interactions of proteins and small molecules in complex biological liquids, gathering information on binding under conditions close to the *in vivo* situation. By using a red-fluorescent label, we avoided background fluorescence caused by the intrinsic fluorescence of proteins in crude cell extract or blood serum. We found that, in cell extracts, binding was dramatically shifted to lower affinities (Fig. 4a). For hIFN-γ, the apparent dissociation constant was determined to be 165 ± 26 nM in the cell extract, compared with 10 ± 2 nM in PBS buffer. Affinities of biomolecules seem to be highly dependent on the composition of the surrounding matrix. Such significant affinity reduction might be caused by competitive interactions with components of the biological liquid or could also be due to differences in viscosity, pH or ionic strength[9]. Using only microliter volumes, MST might be able to measure the affinity of unpurified, expressed antibodies directly in the supernatant of a cell suspension, opening novel ways for fast antibody selection.

Low-molecular-weight binders such as those discussed in the previous section are often likely candidates for new drugs. With MST, small-molecule interactions can also be quantified in complex biological liquids. We performed the quercetin titration series in the presence of 5 and 30% blood serum. The resulting apparent dissociation constants were determined to be $K_d = 6 \pm 0.4$ and $50 \pm 7\,\mu M$, respectively (Fig. 4b). Both experiments were fitted using a cooperativity of 1.5. To understand the cause of this strong shift in affinity, we analysed the effect of the most abundant blood protein, human serum albumin (HSA), on the binding of quercetin to PKA. Owing to its hydrophobic binding pockets, this protein is a universal transport protein for a wide range of molecules and is known to bind, among others, to flavonoids such as quercetin[20]. If adsorption of quercetin to a blood protein occurs, the free concentration of the small molecule available for a binding to PKA is reduced, resulting in a shift of the apparent binding constant. To test whether HSA can cause the observed shift in the apparent affinity of PKA to quercetin, we analysed the binding of quercetin to HSA (Fig. 4c). HSA was labelled with a fluorescent dye, and a titration series of quercetin was prepared (0.5 to 90 µM). The thermophoretic depletion showed a sigmoidal binding curve, which was best fitted using Hill's equation. From the data, we inferred a dissociation coefficient of $9.3 \pm 0.5\,\mu M$ with a Hill coefficient of $h = 2.75 \pm 0.2$, which is in good agreement with literature values[20]. This experiment shows that quercetin binds to HSA and thus is expected to influence the apparent affinity of PKA for quercetin in human serum.

To prove that the effect of the shifted affinities in human serum is due to the presence of HSA, we performed a PKA–quercetin binding experiment in 50 mM HEPES buffer and added HSA at concentrations corresponding to 5 and 30% human serum (Fig. 4d). At 32 µM HSA, which corresponds to 5% human serum, we observed a $K_d = 7.8 \pm 0.6\,\mu M$. At 190 µM HSA, which is the equivalent of 30% human serum, we measured a $K_d = 43 \pm 6\,\mu M$. The observed shift in the apparent dissociation constant differed only by about 20% from those obtained in serum. As in these experiments buffer, ionic strength and viscosity were constant, the reduced apparent affinity in serum is most likely a result of the binding of quercetin to HSA.

This ability of MST to quantify binding near *in vivo* conditions is of high importance as MST can resolve either shifted affinities or competing interactions in biological matrices. This is of importance as information on adverse binding behaviour is typically obtained through clinical studies involving intense efforts and the risk of possible harm for the volunteers.

Discussion

Today, most antibody affinities are determined by surface-based methods such as surface plasmon resonance[21,22]. This technique requires the immobilization of either the antigen or the antibody on a solid surface, potentially raising issues of steric hindrance or molecular activity. Even though surface-based methods are very sensitive, high-affinity interactions are often not accessible for measurement owing to mass transport effects, and transient binders are in most cases difficult to quantify[23]. To analyse interactions in the solution phase, techniques such as fluorescence correlation spectroscopy (FCS)[24], back-scattering interferometry[25–27] and isothermal titration calorimetry[28] are often used. FCS is based on highly sensitive fluorescence microscopy, but relies on a significant change in the diffusion constant upon binding[24]. For this reason, FCS is only applicable to a limited number of biomolecular interactions. The other two methods are label-free and allow monitoring of interactions without disturbance by a label or surfacing; however, these techniques still suffer from limitations. Isothermal titration calorimetry, for example, has a low throughput and exceptionally high sample consumption. Back-scattering interferometry typically suffers from a refractive index background arising from a non-reacted ligand, particularly at high concentrations. In addition, temperature-induced changes of the refractive index may interfere with the binding signal and render the interpretation difficult.

The results we presented suggest that MST is suitable for the quantification of protein–protein affinities and low-molecular-weight binders. Both are of great importance in current basic and pharmaceutical research. Interactions between two proteins of approximately the same molecular weight can be analysed with the same sensitivity as interactions of small molecules or even ions. We attribute this broad range of detectable binding events to the fact that thermophoresis is highly sensitive to changes in the size, charge and hydration shell of molecules. Furthermore, we demonstrate that interaction measurements can be performed in complex biological liquids. Such biological matrices have a strong influence on the binding behaviour. Their analysis provides additional information on the properties and efficacies of the molecules within the human body. Additional work is required to understand the intricacies of MST in more detail. Future work will show how exactly the amplitude of the MST signal reflects changes in the protein conformation or in its hydration shell (for example, release of water molecules from binding sites). The amplitude could give additional information on the binding location of the small molecule and, for example, could detect binding of a small molecule to a deep hydrophobic binding pocket or to the protein surface. In addition, we envisage label-free approaches using the intrinsic fluorescence of proteins in the ultraviolet regime to avoid possible effects of the fluorescent label on the binding. However, label-free approaches will complicate measurements in biological liquids owing to their inherent background signals.

In conclusion, we show that MST provides a fast analysis of interactions with low sample consumption. The measurements equally cover highly affine interactions, as well as interactions of low affinity. We analysed the binding of a broad variety of biologically relevant proteins and found a good signal-to-noise ratio, even for binders that have a low molecular weight. Additionally, the quantification of binding works equally well in biological liquids, where considerable shifts towards lower effective affinities are found. Such information is crucial for studying biomolecule interactions in biology and in drug development.

Methods

Theoretical background of thermophoresis. When an aqueous solution is heated locally, molecules start moving along the temperature gradient. This molecular flow is opposed by mass diffusion. In the steady state, both effects balance, resulting in a stationary spatial concentration distribution[29,30]:

$$c/c_0 = \exp[-S_T^*(T - T_0)] \quad (2)$$

The relative concentration depends solely on Soret coefficient S_T of the molecule and the temperature rise $\Delta T = T - T_0$ at the respective position. Soret coefficient is a measure of the strength of the thermophoretic molecule flow compared with ordinary diffusion. Although the theory of thermophoresis is still under debate, all theoretical descriptions agree that the molecular size and various surface parameters, such as charge and hydrophobicity, have an influence on Soret coefficient S_T. Recent theoretical approaches also include the influence of the Seebeck effect: ions in the buffer move along a thermal gradient and give rise to an electric field, which in turn moves the molecules by electrophoresis[31–33]. As the buffer systems throughout this work used NaCl to set the ionic strength, the resulting Seebeck contribution was suggested to be small[33]. To illustrate the influence of biomolecular parameters on the thermophoretic effect, we have chosen a local thermodynamic description[7]. Experiments suggest that the Soret coefficient can be expressed by[34]

$$S_T = \frac{A}{kT}\left(-\Delta s_{hyd}(T) + \frac{\beta \sigma_{eff}^2}{4\varepsilon\varepsilon_0 T} \times \lambda_{DH}\right) \quad (3)$$

with A being the molecule's surface area, σ_{eff} the effective charge and Δs_{hyd} the hydration entropy of the molecule–solution interface . In addition, Soret coefficient depends on the Debye–Hueckel screening length λ_{DH}, the dielectric constant ε and its temperature derivative β.

As a result, thermophoresis is a measure for the state of a protein, and on binding we expect a change in the thermophoretic signal. A protein–protein

interaction, for example, may change the surface area A, the hydration entropy Δs_{hyd} and the effective charge σ_{eff}, whereas an ion binding to a protein will mainly affect the effective charge. The binding of an uncharged small molecule may change the hydration entropy, as water molecules on the protein surface are released or rearranged. It has already been shown that small conformational changes can affect several of the above parameters. Of note, any change in the thermophoretic parameters on binding allows MST to quantify a binding affinity.

Fluorescence imaging and bleaching correction. We used a Zeiss AxioScope A1 Vario microscope with a 40× Plan Fluar oil objective (Numerical aperture NA = 1.3, Zeiss), excited with Luxeon high-power LEDs (cyan, red). The LEDs were built into a standard halogen lamp housing and driven at a current of 10–200 mA by an ILX Lightwave LD-3565 constant current source, providing low illumination noise levels. Fluorescence filters were from AHF-Analysentechnik for HEX (F36-542) and AlexaFluor647 (F36-523). Detection was provided with a 12-bit PCO Sensicam uv camera (PCO AG) with a pixel size of 8 µm×8 µm, a maximum quantum efficiency of 65%, and typically 8×8 pixel binning. Exposure times ranged between 100 and 500 ms.

Infrared laser heating. Temperature gradients were created with an infrared laser diode (Furukawa FOL1405-RTV-617-1480, 1480 nm, 320 mW maximum power) purchased from AMS Technologies AG. The infrared-laser beam couples into the path of light with a dichroic mirror (NT46-386) from Edmund Optics and is focused into the fluid with the microscope objective also used for fluorescence imaging. Typically, the temperature in the solution was raised by 5 K in the beam center, with a $1/e^2$ diameter of 25 µm. All measurements were performed at a room temperature of approximately 20 °C, except for the binding of hIFN-γ, which was performed at 5 °C to avoid proteolysis.

Microfluidic chambers. We used fused silica capillaries (Polymicro Technologies) with an inner diameter of about 100 µm and an outer diameter of 370 µm. Inner dimensions varied only by ±0.5 µm per 10 m capillary length. The well-defined thickness allowed for good control and repeatability of the temperature. Binding of molecules to the capillary surface was low and was tested by measuring residual fluorescence after rinsing the capillary with buffer. The sample volume was about 500 nl.

Data analysis. The change in concentration was averaged over a rectangular region around the center of heating. We corrected the fluorescence signal for the temperature dependency of the fluorescence emission[35]. Generally, the fluorescence was independent of the binding state. This correction did not include possible binding-dependent changes in the temperature response of the molecule. Slow conformational variations were recently reported by Ebbinghaus *et al.*[36] and can lead to an uncertainty when determining the exact depletion, but does not effect the precision of the analysis. The relative change in concentration was normalized to the saturation value, at which all molecules were in the bound state. The binding of ligands to a specific receptor is characterized by K_d and the total concentration of binding sites, $[B_0]$. The determination of these two parameters can be achieved using saturation-binding curves obtained at equilibrium[37]. $[L_0]$ equals the amount of added ligand at each data point and [BL] is the concentration of formed complexes between the binding sites, [B], and the ligand, [L]. The fitting function is derived from the law of mass action:

$$\frac{[BL]}{[B_0]} = \frac{([L_0]+[B_0]+K_d) - \sqrt{(([L_0]+[B_0]+K_d)^2 - 4\cdot[L_0]\cdot[B_0])}}{2[B_0]} \quad (4)$$

For reactions with more than one ligand binding to one binding partner or in case of cooperativity on binding, the data were fitted using Hill's equation:

$$\frac{[BL]}{[B_0]} = \frac{1}{1+K_d/([L])^h} \quad (5)$$

with h being Hill coefficient, K_d the dissociation constant and [L] the concentration of ligand. Equation (5) was only used when the free concentration of the ligand was not altered by the formation of the complex and $[L] = [L_0]$ was approximately true.

Proteins. hIFN-γ (product PHP050) and its anti-IFN-γ antibody (product HCA043) were gifts from AbD Serotec. The antibody is a bivalent human recombinant Fab selected from the HuCAL GOLD phage display library and dimerized via a helix–turn–helix motif. The antibody was labelled with AlexaFluor 647 (Invitrogen) and used at a constant antibody concentration of 5 nM. Human IFN-γ was titrated from 0.1 to 700 nM. The experiments were performed in a standard PBS (1× PBS) solution. To prevent proteolysis, measurements in either buffer or *E. coli* extract were performed at 5 °C. The buffer conditions were 1× PBS with 5% bovine serum albumin and 0.01% Tween20. Before the measurement, samples were incubated for 1 h on ice. Chromotek GmbH provided the GFP, GBP, GBP mutant (GBP R37A) and RBP. GFP is a 28-kDa protein with intrinsic fluorescence. The GBP is a small 14.1-kDa protein originally isolated from the lymphocytes of a Llama Alpaca (Llama Pacos) immunized with purified GFP[12]. RBP is an RFP-binding protein with a molecular weight of 15 kDa and was used as a negative control. The measurements were performed in 1× PBS using 40 nM GFP and by titrating from 0.1 nM to 4 µM of GBP. CaM was purchased from AbD Serotec and labelled with AlexaFluor 647. The analysis was performed in 1× PBS. All CaM solutions contained a small amount of EDTA to bind any free Ca^{2+} ions before mixing with the desired concentration of calcium ions. For the interaction analysis in serum, Crelux GmbH provided the protein kinase A and the inhibitor quercetin. The kinase was labelled with AlexaFluor 647 and was used at a final concentration of 300 nM. The binding was measured in 50 mM HEPES at pH 7.5 containing 100 mM NaCl and 5% DMSO. Quercetin was titrated from 11.5 nM to 50 µM, close to the solubility limit of the substance. After mixing the protein with quercetin, the serum was added and incubated for 1 h at room temperature. For the analysis of HSA with quercetin, HSA was labelled with AlexaFluor 647 and used at a final concentration of 50 nM. The titration series of quercetin ranged from 0.5 to 90 µM. The interaction was analysed in 50 mM HEPES buffer at pH 7.5 containing 100 mM NaCl.

Labelling procedure. The labelling was performed with reactive dyes using N-Hydroxysuccinimide (NHS)–ester chemistry, which reacts efficiently with the primary amines of proteins to form highly stable dye–protein conjugates. The labelling step requires that the protein be dissolved in a suitable labelling buffer at the correct pH. For protein labelling, the protein concentration was adjusted to 2–20 µM using the labelling buffer. Lower concentrations may result in loss of coupling efficiency. The solid fluorescent dye was dissolved in 100% DMSO at a concentration of about 1.3 mM and mixed thoroughly. Before mixing the protein and the dye, the concentration of the dye was adjusted to 2–3-fold concentration of the protein using the labelling buffer. Then, the protein and the fluorescent dye solutions were mixed in 1:1 ratio and incubated for 30 min at room temperature in the dark.

Unreacted 'free' dye was eliminated by gelfiltration columns (Sephadex G25, GE Healthcare). The purity was monitored by measuring the ratio of protein to dye (for example, spectroscopically by measuring absorption at 280 nm for protein and 650 nm for the dye; molar absorbance: 250,000 $M^{-1}cm^{-1}$) after the clean-up procedure.

References

1. Ludwig, C. Diffusion zwischen ungleich erwärmten Orten gleich zusammengesetzter Lösungen. *Sitzungsber. Akad. Wiss. Wien Math.-Naturwiss.* **20,** 539 (1856).
2. Rauch, J. & Köhler, W. Diffusion and thermal diffusion of semidilute to concentrated solutions of polystyrene in toluene in the vicinity of the glass transition. *Phys. Rev. Lett.* **88,** 185901 (2002).
3. Wiegand, S. & Köhler, W. *Thermal Nonequilibrium Phenomena in Fluid Mixtures* (Springer, 2002).
4. Braun, D. & Libchaber, A. Trapping of DNA by thermophoretic depletion and convection. *Phys. Rev. Lett.* **89,** 188103 (2002).
5. Iacopini, S. & Piazza, R. Thermophoresis in protein solutions. *Europhys. Lett.* **63,** 247–253 (2003).
6. Piazza, R., Iacopini, S. & Triulzi, B. Thermophoresis as a probe of particle-solvent interactions: the case of protein solutions. *Phys. Chem. Chem. Phys.* **6,** 1616–1622 (2004).
7. Dhont, J. K. G., Wiegand, S., Duhr, S. & Braun, D. Thermodiffusion of charged colloids: single-particle diffusion. *Langmuir* **23,** 1674–1683 (2007).
8. Würger, A. Thermophoresis in colloidal suspensions driven by Marangoni forces. *Phys. Rev. Lett.* **98,** 138301 (2007).
9. Baaske, P., Wienken, C. J., Reineck, P., Duhr, S. & Braun, D. Optical thermophoresis for quantifying the buffer dependence of aptamer binding. *Angew. Chem. Int. Ed.* **49,** 2238–2241 (2010).
10. Reineck, P., Wienken, C. J. & Braun, D. Thermophoresis of single stranded DNA. *Electrophoresis* **31,** 279–286 (2010).
11. Sperling, R. *et al.* Size determination of (bio)conjugated water-soluble colloidal nanoparticles: a comparison of different techniques. *J. Phys. Chem. C* **111,** 11552–11559 (2007).
12. Schoenborn, J. R. & Wilson, C. B. Regulation of interferon-gamma during innate and adaptive immune responses. *Adv. Immunol.* **96,** 41–101 (2007).
13. Rothbauer, U. *et al.* Targeting and tracing antigens in live cells with fluorescent nanobodies. *Nat. Methods* **3,** 887–889 (2006).
14. Jecklin, M. C., Schauer, S., Dumelin, C. E. & Zenobi, R. Label-free determination of protein-ligand binding constants using mass spectrometry and validation using surface plasmon resonance and isothermal titration calorimetry. *J. Mol. Recognit.* **22,** 319–329 (2009).
15. Cheung, W. Y. Calmodulin plays a pivotal role in cellular regulation. *Science* **207,** 19–27 (1980).
16. Project, E., Friedman, R., Nachliel, E. & Gutman, M. A molecular dynamics study of the effect of Ca2+ removal on calmodulin structure. *Biophys. J.* **90,** 3842–3850 (2006).

17. Tsuruta, H. & Sano, T. A fluorescence temperature-jump study on Ca^{2+}-induced conformational changes in calmodulin. *Biophys. Chem.* **35,** 75–84 (1990).
18. Walker, E. H. *et al.* Structural determinants of phosphoinositide 3-kinase inhibition by wortmannin, LY294002, quercetin, myricetin, and staurosporine. *Mol. Cell* **6,** 909–919 (2000).
19. Hemmings, H. C. *Protein Kinase and Phosphatase Inhibitors, Applications in Neuroscience* (Humana, 1997).
20. Dufour, C. & Dangles, O. Flavonoid–serum albumin complexation: determination of binding constants and binding sites by fluorescence spectroscopy. *Biochim. Biophys. Acta* **1721,** 164–173 (2005).
21. Fägerstam, L. G. *et al.* Detection of antigen—antibody interactions by surface plasmon resonance. Application to epitope mapping. *J. Mol. Recognit.* **3,** 208–214 (1990).
22. Shankaran, D. R., Gobi, K. & Miura, N. Recent advancements in surface plasmon resonance immunosensors for detection of small molecules of biomedical, food and environmental interest. *Sens. Actuators B Chem.* **21,** 158–177 (2007).
23. MacKenzie, C. R. *et al.* Analysis by surface plasmon resonance of the influence of valence on the ligand binding affinity and kinetics of an anti-carbohydrate antibody. *J. Biol. Chem.* **271,** 1527–1533 (1996).
24. Chen, Y., Müller, J. D., Tetin, S. Y., Tyner, J. D. & Gratton, E. Probing ligand protein binding equilibria with fluorescence fluctuation spectroscopy. *Biophys. J.* **79,** 1074–1084 (2000).
25. Bornhop, D. J. *et al.* Free-solution, label-free molecular interactions studied by back-scattering interferometry. *Science* **317,** 1732–1736 (2007).
26. Markov, D. A., Swinney, K. & Bornhop, D. J. Label-free molecular interaction determinations with nanoscale interferometry. *J. Am. Chem. Soc.* **126,** 16659–16664 (2004).
27. Latham, J. C., Markov, D. A., Sorensen, H. S. & Bornhop, D. J. Photobiotin surface chemistry improves label-free interferometric sensing of biochemical interactions. *Angew. Chem. Int. Ed.* **45,** 955–958 (2006).
28. Leavitt, S. & Freire, E. Direct measurement of protein binding energetics by isothermal titration calorimetry. *Curr. Opin. Struct. Biol.* **11,** 560–566 (2001).
29. Duhr, S. & Braun, D. Thermophoretic depletion follows Boltzmann distribution. *Phys. Rev. Lett.* **96,** 168301 (2006).
30. de Groot, S. R. & Mazur, P. *Non-Equilibrium Thermodynamics* (North Holland, 1962).
31. Putnam, S. A. & Cahill, D. G. Transport of nanoscale latex spheres in a temperature gradient. *Langmuir* **21,** 5317–5323 (2005).
32. Wurger, A. Transport in charged colloids driven by thermoelectricity. *Phys. Rev. Lett.* **101,** 108302 (2008).
33. Vigolo, D., Buzzaccaro, S. & Piazza, R. Thermophoresis and thermoelectricity in surfactant solutions. *Langmuir* **26,** 7792–7801 (2010).
34. Duhr, S. & Braun, D. Why molecules move along a temperature gradient. *Proc. Natl Acad. Sci. USA* **103,** 19678–19682 (2006).
35. Duhr, S., Arduini, S. & Braun, D. Thermophoresis of DNA determined by microfluidic fluorescence. *Eur. Phys. J. E* **15,** 277–286 (2004).
36. Ebbinghaus, S., Dhar, A., McDonald, J. D. & Gruebele, M. Protein folding stability and dynamics in a living cell. *Nat. Methods* **7,** 319–323 (2010).
37. Swillens, S. Interpretation of binding curves obtained with high receptor concentrations: practical aid for computer analysis. *Mol. Pharmacol.* **47,** 1197–1203 (1995).

Acknowledgments

We thank Moran Jerabek-Willemsen, Uta Steinbach, David Smith, Paul Andreassen and Philipp Mertins for comments on the paper and many thoughtful discussions. We gratefully acknowledge financial support from the Functional NanoSystems Initiative (FuNS), the Excellence Cluster NanoSystems Initiative Munich (NIM) and express our gratitude to the Center for Nanoscience (CeNS). We thank Crelux GmbH (Martinsried, Germany) for providing the kinase PKA and the small-molecule inhibitor quercetin, and Dr Achim Knappik (AbD Serotec, A Division of MorphoSys, Martinsried, Germany) for the IFN-γ and the corresponding antibody.

Author contributions

S.D. and C.J.W. designed and performed the experiments, analysed the data and wrote the paper; P.B. performed the experiments and analysed the data; U.R. provided the reagents and performed the experiments; D.B. analysed the data and wrote the paper.

Additional information

Supplementary Information accompanies this paper on http://www.nature.com/naturecommunications

Competing financial interests: Stefan Duhr and Philipp Baaske are founders of the LMU spin out company NanoTemper Technologies GmbH, which provides services and devices based on thermophoresis.

Reprints and permission information is available online at http://npg.nature.com/reprintsandpermissions/

How to cite this article: Wienken, C. J. *et al.* Protein binding assays in biological liquids using microscale thermophoresis. *Nat. Commun.* 1:100 doi: 10.1038/ncomms1093 (2010).

Published online 4 February 2011

Nucleic Acids Research, 2011, Vol. 39, No. 8 ***e52***
doi:10.1093/nar/gkr035

Thermophoretic melting curves quantify the conformation and stability of RNA and DNA

Christoph J. Wienken[1], Philipp Baaske[1,2], Stefan Duhr[1,2] and Dieter Braun[1,*]

[1]Systems Biophysics, Physics Department and Center for NanoScience, Ludwig-Maximilians-Universität München and [2]NanoTemper Technologies GmbH, Amalienstrasse 54, 80799 München, Germany

Received September 8, 2010; Revised January 12, 2011; Accepted January 13, 2011

ABSTRACT

Measuring parameters such as stability and conformation of biomolecules, especially of nucleic acids, is important in the field of biology, medical diagnostics and biotechnology. We present a thermophoretic method to analyse the conformation and thermal stability of nucleic acids. It relies on the directed movement of molecules in a temperature gradient that depends on surface characteristics of the molecule, such as size, charge and hydrophobicity. By measuring thermophoresis of nucleic acids over temperature, we find clear melting transitions and resolve intermediate conformational states. These intermediate states are indicated by an additional peak in the thermophoretic signal preceding most melting transitions. We analysed single nucleotide polymorphisms, DNA modifications, conformational states of DNA hairpins and microRNA duplexes. The method is validated successfully against calculated melting temperatures and UV absorbance measurements. Interestingly, the methylation of DNA is detected by the thermophoretic amplitude even if it does not affect the melting temperature. In the described setup, thermophoresis is measured all-optical in a simple setup using a reproducible capillary format with only 250 nl probe consumption. The thermophoretic analysis of nucleic acids shows the technique's versatility for the investigation of nucleic acids relevant in cellular processes like RNA interference or gene silencing.

INTRODUCTION

Nucleic acids play a fundamental role in cellular processes and are the subject of intense biological research. Short non-coding RNA is expected to be an especially versatile target for new drugs or pharmaceuticals. Measuring the stability of these nucleic acids is especially important and typically measured with melting curve analysis. In such experiments, the sample is heated through a range of temperatures, while typically fluorescence or UV absorbance is continuously collected (1–4). Although well established, UV absorption measurements of melting curves require a considerable amount of DNA sample. As a result fluorescence approaches have gained momentum (5–7). However, these techniques often suffer from the missing sequence specificity of the fluorescence signal and are less sensitive to detect transitions which do not change the number of closed base pairs. This is due to the use of an intercalating fluorescent dye, which predominantly reflects the amount of double-stranded DNA in the sample. Thus, an analysis of purely tertiary DNA structures like for example G-quadruplexes are difficult to access. These restrictions can be reduced by separating the molecular recognition from the signal transduction, which is achieved using specially designed primers like scorpion primers or probes with fluorophore-acceptor pairs (8). However, these primers are complex in design and dramatically increase the cost for a melting curve analysis.

Another approach that measures the stability of nucleic acids or proteins is thermal gradient electrophoresis (9,10). It uses standard gel electrophoresis with an additionally applied thermal gradient perpendicular to the electric field. According to the position in the temperature gradient, the molecules experience different temperatures. When the molecules melt, they show a change in size or effective charge and thus show a different movement in the gel matrix. The advantage of this technique is that it records the motion of the molecules at all temperatures at once and can thus reduce the time to record a melting curve. On the other hand, the gel matrix does not represent the molecules' native environment and gel preparation is time-consuming.

When using thermophoresis to monitor the melting of molecules, the sample is heated through a range of temperatures as it is the case for UV and fluorescence melting curves. But the information about the melting of the probe is provided by the movement of molecules and not by a

*To whom correspondence should be addressed. Tel: +49 89 2180 2317; Fax: +49 89 2180 16558; Email: dieter.braun@lmu.de

change in absorbance or fluorescence. Hence, the thermophoretic approach requires only one unspecific tag to monitor the melting behaviour. The movement of particles in a temperature gradient (11) known as thermophoresis, or Soret effect depends on the size of a molecule, its charge and other surface properties such as ionic shielding and the hydration shell of the molecule (12,13). Thus, when one property of the monitored particles changes, for example, by changing its conformation or interacting with another molecule, the Soret coefficient changes. Recently, it was confirmed that binding events can be monitored with thermophoresis (14,15). Since the hybridization of DNA strands dramatically alters the molecular properties of the labelled primer, thermophoresis measurements are suitable for monitoring the melting of nucleic acids.

EXPERIMENTAL SECTION

Basics of thermophoresis

When an aqueous solution is locally heated, particles start to move in the given temperature gradient ∇T. The resulting movement is described by a linear thermophoretic drift $v = -D_T \nabla T$ which is then counteracted by a diffusive backflow $j = -D\nabla c$ with diffusion coefficient D and the concentration gradient ∇c. These two fluxes lead to a steady state molecule distribution, which is characterized by the Soret coefficient. The Soret coefficient is defined as the ratio $S_T = D_T/D$ and determines the magnitude of the change in concentration. In steady state, a temperature difference ΔT results in a change in concentration Δc, which can be derived from the following Equation (16).

$$\frac{c}{c_0} = \exp(-S_T \Delta T) \approx 1 - S_T \Delta T \quad (1)$$

The concentration in the heated region c is normalized against the initial concentration c_0 before applying the temperature gradient. In our experiments, the depletion is small ($S_T \Delta T << 1$) and thus, a linear function of the temperature increase. While the microscopic basis of thermophoresis is still under debate, experiments indicate that interfacial properties such as size, charge and hydrophobicity affect the Soret coefficient (12,13).

Temperature dependence of thermophoresis

Iacopini *et al.* (17) investigated the temperature dependence of the Soret effect through measuring the thermophoretic properties of various biomolecules. They found a characteristic dependence, which is described well with an empirical fitting function:

$$S_{T,i}(T) = S_{T,i}^{\infty}\left[1 - \exp\left(\frac{T^* - T}{T_{0,i}}\right)\right] \quad (2)$$

Here S_T^{∞} represents the thermophoretic limit for high temperatures T, while T^* is the temperature where S_T switches its sign and T_0 is a rate of exponential growth that embodies the strength of the temperature effect. Our experiments showed that the temperature dependence differs for double- and single-stranded molecules, which is reflected in the index *i*. In previous experiments (12) the sign switching temperature T^* was found to be at $\sim$4°C for DNA strands of different length. The following analysis confirmed this finding, and we fixed $T^* = 277$ K throughout the analysis.

Analysis of thermophoretic melting curves

To determine the melting temperatures from the Soret coefficient, we corrected for the temperature dependence of $S_{T,i}(T)$ and used Equation (2) to infer the high temperature limit $S_{T,i}^{\infty}$. This $S_{T,i}^{\infty}$ is constant for each conformational state $i = \{ss,ds\}$ of the nucleic acid. Due to the linearity of thermophoretic depletion [Equation (1)], the experimentally measured apparent S_T^{∞} is a linear superposition of the closed and melted state, showing a transition from $S_{T,ds}^{\infty}$ to $S_{T,ss}^{\infty}$ given by:

$$S_T^{\infty}(x) = x \cdot S_{T,ss}^{\infty} + (1 - x) S_{T,ds}^{\infty} \quad (3)$$

The parameter x represents the fraction of molecules in the single-stranded state. $S_{T,ss}^{\infty}$ is the high temperature limit S_T^{∞} for single-stranded DNA, $S_{T,ds}^{\infty}$ for double-stranded DNA. The melting temperature T_m represents the temperature at which $x = 0.5$ holds (18).

Presenting the thermophoretic melting curve in terms of the high temperature limit S_T^{∞} allows an analysis of the melting temperature combined with a quantification of the thermophoretic properties. These properties contain additional information about the molecular size and conformation.

The melting of nucleic acids is mostly interpreted as a two-state process, where double-stranded molecules are transferred into a single-stranded state. Such an interpretation ignores intermediate states (e.g. due to the unfolding of tertiary structures) but still is a good approximation for many DNA melting curves. An intermediate state with $S_{T,\mathrm{int}}^{\infty}$ leads to an expanded equation:

$$S_T^{\mathrm{obs}} = x_{ss} \cdot S_{T,ss}^{\infty} + x_{\mathrm{int}} \cdot S_{T,\mathrm{int}}^{\infty}(1 - x_{ss} - x_{\mathrm{int}}) S_{T,ds}^{\infty} \quad (4)$$

At the temperature with $x_{\mathrm{int}} = 0.5$, the double-stranded structure melts into the intermediate conformation, at $x_{ss} = 0.5$ the intermediate structure melts into single-stranded DNA. To infer T_m from the melting curve, the data was analysed using a sigmoidal fitting function:

$$x(T) = \frac{1}{1 + \exp\left(\frac{T_m - T}{\mathrm{width}}\right)} \quad (5)$$

If intermediate states were observed, the data was fitted with an additive superposition of two sigmoidal curves.

Experimental setup

In our experiments, temperature gradients in solution were generated by a local absorption of an infrared laser in the sample (19). At a wavelength of 1480 nm, water strongly absorbs the radiation and a local increase in temperature is obtained. An epi-fluorescence microscope was modified by adding an IR laser (Furukawa FOL1405-RTV-617-1480, 1480 nm, 320 mW maximum

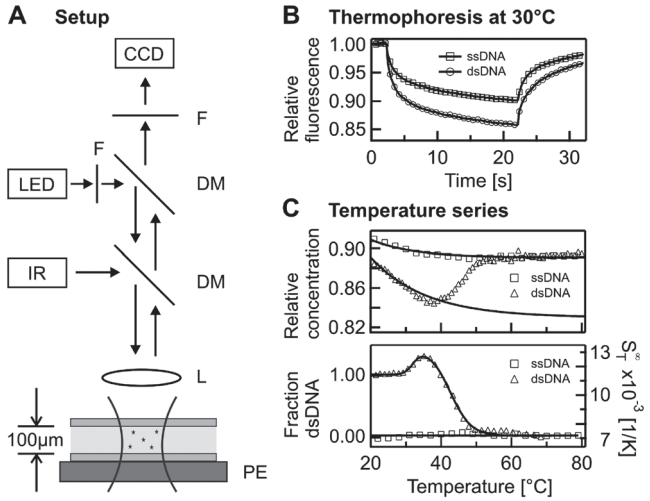

Figure 1. Thermophoresis assay. (**A**) The solution inside a capillary was locally heated with a focused infrared laser (IR), coupled into an epi-fluorescence microscope using a dichroic mirror (DM). A capillary was used as a sample compartment and placed on top of a peltier stage (PE), which allowed adjustment of the overall sample temperature. L, lens; LED, light emitting diode; F, fliter; CCD, CCD camera. (**B**) The data obtained with our setup was the relative concentration inferred from the recorded fluorescence signal. Single- and double-stranded DNA showed different depleted concentrations in the heated laser spot. (**C**) When repeated for different temperatures, single-stranded DNA (ssDNA) as well as double-stranded DNA (dsDNA) showed a pronounced temperature dependence, which was fitted using Equation (3). Correcting the data for this temperature dependence, a typical DNA melting curve appeared.

power, AMS Technologies AG, Martinsried, Germany) to the microscope. The setup is shown schematically in Figure 1A. The IR laser was coupled into the beam of light by inserting a dichroic mirror (NT46-386, Edmund Optics, Barrington, USA) between microscope (AxioTech Vario, Zeiss, Oberkochen, Germany) and objective ($40\times$ magnification, NA = 0.8, Partec GmbH, Münster, Germany). The dichroic mirror deflects infrared radiation and is transparent for visible light. Using this setting, the IR laser is focused in the sample plane and allowed simultaneous monitoring of the fluorescence inside the sample. Fluorescence was excited with Luxeon high-power LEDs (Luxeon V-star, cyan; Luxeon III-star, red; Luxeon, Calgary, Canada). The LEDs were built into a standard halogen lamp housing and driven at a current of 10–200 mA by an ILX Lightwave LD-3565 constant current source, providing low illumination noise levels. Fluorescence images were recorded with a Sensicam QE CCD camera (PCO AG, Kelheim, Germany). Measurement chambers were capillaries made of fused silica with an inner diameter of 100 µm (Polymicro Technologies, Phoenix, USA), resulting in a low sample consumption of ~250 nl per measurement. To obtain a more facile handling when preparing the samples and filling the capillaries, we typically used a priming volume of ~5 µl. This could be further reduced by using automated sample preparation.

The IR laser heating gave a Gaussian temperature profile with a $1/e^2$ diameter of 25 µm and a peak temperature of typically 15 K. The temperature profile was obtained using the temperature dependence of the fluorescent dye Cy5 in $1\times$ saline sodium citrate ($1\times$ SSC), which was determined independently by a fluorometer experiment (20). The temperature profile inside the capillaries was highly reproducible with a precision of ± 0.1 K (13). The overall sample temperature was controlled with a peltier element beneath the capillary, which allows to scan a broad range of sample temperatures with the precision of ± 0.1 K. The effective sample temperature was corrected for the additional temperature increase due to the laser heating. For better thermal contact, a thin layer of oil was used between the surface of the peltier element and the capillary.

Measurements

For recording a melting curve, the overall sample temperature was increased stepwise with an equilibration time of 60 s at each temperature. Typically a step size between 0.6 and 2°C was used but it could be lowered to 0.2°C depending on the desired accuracy. At every temperature, a thermophoretic time trace was recorded (Figure 1B). First, the fluorescence of the sample was acquired for several seconds and then the IR-Laser was switched on to create a temperature gradient and trigger the thermophoretic movement. Due to the small dimensions of the local heating, the spatial distribution of DNA molecules in the heated spot came close to its steady state within the measurement time of 20 s. After this time the IR-laser was switched off again and the molecules re-established their initial homogeneous molecule distribution. Throughout the measurement, the fluorescence is recorded with the CCD-camera. To infer the relative change in concentration from the fluorescence signal, the curve was normalized with a fluorescence image 500 ms after switching on the IR laser. At this time, the temperature profile in the capillary was already established, while the concentration profile was almost unchanged (7). This allowed correcting the fluorescence signal for the temperature dependence of the fluorescent dye. For the fluorophore HEX, the temperature dependence was in the order of 0.0–0.24%/K depending on the nucleic acid molecule attached. The Soret coefficient S_T was obtained from the magnitude of the depleted concentration according to Equation (1). When plotting the Soret coefficient over temperature a transition from the double-stranded state to the single-stranded state was observed (Figure 1C, top). This curve was then corrected with the temperature dependence of the Soret coefficient according to Equation (2) resulting in a melting curve presented in the high temperature limit S_T^{∞} (Figure 1C, bottom). Using Equation (3) or (4) allowed to determine the fraction of double-stranded and single-stranded DNA. To derive the exact melting temperatures the temperature used for plotting was corrected for the additional heating by the IR-laser. All experiments were compared to UV absorbance melting curves that were obtained with a temperature controlled spectrometer (Jasco GmbH, Gross-Umstadt, Germany) using the same DNA concentrations and equal buffer conditions.

Table 1. Sequences of nucleic acids. The underlined bases represent mutated or modified bases or dangling ends

	Sequence (5′–3′)
Reference DNA #1	HEX-ATTGAGATACACATTAGAACTA
Reference DNA #2	HEX-ATTGAGATATACATTAGAATTA
Reference DNA #3	HEX-AGTGAGATAGACAGTAGAACTA
Perfect match	TAGTTCTAATGTGTATCTCAAT
Single nucleotide mismatch	TAGTTCTAATGTCTATCTCAAT
Methylated perfect match	TAGTTCTXATGTGTATCTCXAT where X is a N6-Methyl-dA
22 nt dangling ends random	TTTATATTTGTAGTACTTCAGATAGTTCTAATGTGTATCTCAATACTTTTGTTACTG TTTACTATT
11 nt dangling ends random	AGTACTTCAGATAGTTCTAATGTGTATCTCAATACTTTTGTTAC
11 nt dangling ends polyA	AAAAAAAAAAATAGTTCTAATGTGTATCTCAATAAAAAAAAAAA
11 nt dangling ends polyT	TTTTTTTTTTTTAGTTCTAATGTGTATCTCAATTTTTTTTTTTT
5 nt dangling ends random	TCAGATAGTTCTAATGTGTATCTCAATACTTT
11 nt dangling ends polyA – Duplex #2	AAAAAAAAAAATAATTCTAATGTATATCTCAATAAAAAAAAAAA
11 nt dangling ends polyA – Duplex #3	AAAAAAAAAAATAGTTCTACTGTCTATCTCACTAAAAAAAAAAA
Hairpin DNA	Cy3–TTTACAACGGTTTAGCGTTGTA
DNA thrombin aptamer	Cy5–TGGTTGGTGTGGTTGGT
DNA thrombin aptamer mutant	Cy5–TGGTTGTTGTGGTTTGT
Reference RNA	HEX–UAGUUCUAAUGUGUAUCUCAAU
RNA perfect match	AUUGAGAUACACAUUAGAACUA

Molecules

The oligomers (Metabion AG, Martinried, Germany) used in this study are shown in Table 1. All molecules were diluted to a concentration of 1 μM in 1 × SSC (15 mM sodium citrate, pH 7.4, 150 mM NaCl) except for the DNA thrombin aptamer which was diluted in its selection buffer. (20 mM Tris–HCl pH 7.4, 150 mM NaCl, 5 mM KCl, 1 mM $CaCl_2$, 1 mM $MgCl_2$, 0.01% Tween-20). For duplex formation, the single-stranded nucleic acids were mixed in a ratio of 1:1 and annealed by heating the sample to 95°C and then gradually cooling it to room temperature. This procedure favours the energetically most likely conformation. Aptamer and hairpin were heated to 95°C, as well, but then rapidly cooled on ice to prevent homodimer formation and trap the molecules in their tertiary structure.

RESULTS

In the following, we used thermophoresis to perform various types of melting analysis. The experiments cover the melting of DNA duplexes and RNA structures like RNA-RNA duplexes. We further used the technique to analyse the melting of DNA tertiary structures and to investigate the influence of methylation on the melting properties. All results are compared to UV absorbance melting curves and to calculations estimating the melting temperature on the basis of nearest neighbour thermodynamics (21–24).

Standard DNA melting

First we analysed DNA–DNA melting using short DNA oligonucleotides in a range typical for antisense DNA (25). These nucleic acids can selectively inhibit the expression of a single protein when internalized into a cell (26). Thermophoresis is capable of acquiring standard melting curves with high precision and can distinguish between single point mutations. The S_T^∞ of the sample was measured in a temperature range from 30 to 90°C (Figure 2A). As double-stranded DNA melts into single-stranded molecules, the thermophoretic properties change significantly. When comparing the thermophoretic melting curve with the expected sigmoidal shape of a melting transition, an unexpected initial increase of the thermophoretic amplitude before the actual melting into single-strands was observed (Figure 2A, triangles). This may reflect a change in DNA size or indicate an intermediate conformation of the DNA duplex. For control, single-stranded DNA without complementary DNA was measured which showed neither transition and reproduced the S_T^∞ of completely melted DNA (Figure 2A, squares). The obtained melting temperature was $T_m = 56.3 \pm 0.1$°C, the melting temperature for the transition into the intermediate state was $T_m = 49.7 \pm 0.2$°C. This melting analysis was compared to theoretically predicted melting temperatures and control experiments performed with UV absorbance spectroscopy. The UV control yielded $T_m = 56.4 \pm 0.1$°C for the perfect match, but did not show an intermediate state before the melting. For the theoretically predicted value we found 56.3 ± 1.4°C (21–24) (Figure 2A, vertical bar). Both, the melting temperature obtained with UV absorbance and T_m obtained from thermodynamic calculations are in very good agreement with the results gained from the thermophoretic signal. This demonstrates that the thermophoresis signal is well suited to quantify the stability of nucleic acids.

We further tested if we could monitor the effect of a single point mutation on the melting behaviour with thermophoresis. The melting analysis of DNA containing such a mutation compared to the melting of a perfectly matching DNA is shown in Figure 2B. For DNA with a mismatch in the sequence a transition before the melting into two strands was observed at $T_m = 36.3 \pm 0.4$°C. The mismatch resulted in a lower melting temperature

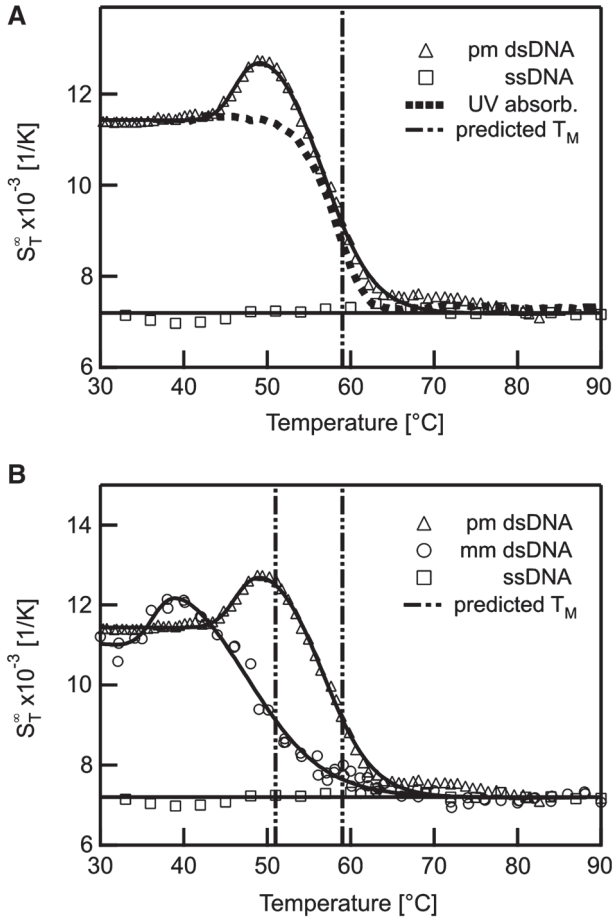

Figure 2. DNA melting curves. Thermophoresis allows the measurement of the melting curve of DNA molecules. (**A**) The melting of a 22 bp long DNA oligonucleotide was analysed with thermophoresis and UV absorbance and compared to thermodynamic calculations. (**B**) DNA containing a single base mismatch was compared to perfectly matching DNA. The mismatch showed a changed melting temperature T_m due to the lower thermal stability by the base mismatch.

$T_m = 47.7 \pm 0.9°C$ compared to the perfect match. This is in good agreement with thermodynamic calculations which yield a melting temperature of $47.9 \pm 1.4°C$. The measurement with UV absorbance also showed a deviation from the two-state model with melting temperatures $T_m = 37.7 \pm 0.5°C$ for the first transition and $T_m = 44.9 \pm 0.1°C$ for melting (data not shown). This is in fair agreement with the thermophoretic and calculated melting temperature. The deviation in the UV absorbance may be caused by the correction of the curves with sloping baselines (18).

The thermophoretic stability analysis was then applied to DNA with methylated bases to analyse the influence of this modification on the stability. DNA methylation is essential for cell differentiation and viability and seems to function as a tool for partitioning the genome into active and inactive parts (27–29). Methylation is further incorporated in various diseases like cancer (30) and heart disease as well as aspects of ageing (31). To test the thermophoretic analysis, two adenosines in the sequence of perfectly matching DNA were replaced with

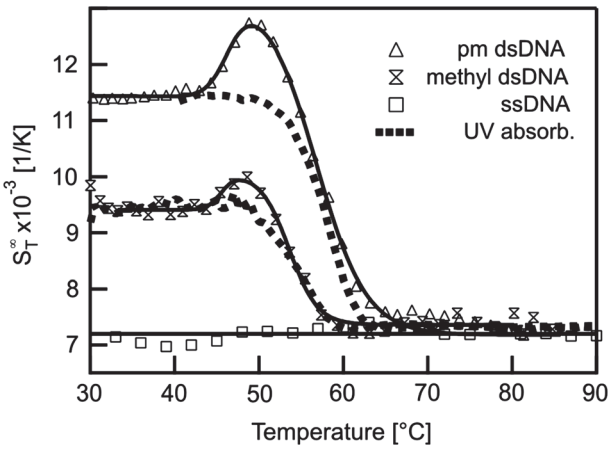

Figure 3. Methylated DNA. The effect of methylated bases on the stability of DNA was analysed with thermophoresis and compared to UV absorbance. Beside monitoring the melting of the two strands, the Soret coefficient at low temperatures showed a significant reduction in the thermophoretic amplitude resulting from the modified bases.

N6-Methyl-2′-dA. The modification led to a decrease in the melting temperature by 2.7°C to $T_m = 53.6 \pm 0.4°C$ (Figure 3). Before the melting an initial transition was measured at $45.5 \pm 0.7°C$. The reference experiment with UV absorbance spectroscopy yielded $T_m = 53.3 \pm 0.2°C$. Interestingly, the Soret coefficient showed a strong difference of 2.0×10^{-3} 1/K in S_T^∞ between normal and the methylated DNA at low temperatures and allowed for a discrimination of the two species by the Soret signal alone. Such a difference was still observable when comparing the perfect match and the single mismatch at low temperatures. Here, a difference in S_T^∞ of 0.4×10^{-3} 1/K was found. This underlines the high sensitivity of thermophoresis for the analysis of various surface properties of biomolecules (12–15).

In contrast to standard melting techniques, the thermophoretic melting data also contains information about possible intermediate states or conformational changes. A transition prior to melting has been observed for all measured samples. Such information may be of importance as cellular functions of nucleic acids not only rely on the sequence but also on their structure.

Additional transitions upon melting

The initial transitions before the actual melting were unexpected at first glance but appeared in all thermophoretic melting experiments. Hence, it seems to be a general process which occurs in the melting process. A possible explanation for the increase in S_T^∞ is shown in Figure 4A. We propose that partial unfolding of the duplex at the two ends increases the surface area of the duplex. This leads to a rise in the S_T^∞ (12). To test this hypothesis, the effect was tested by adding dangling ends at both sides of the duplex which should then result in an increase of the thermophoretic amplitude. Such overlaps are important in biology as they are known to determine the stability of codon–anticodon associations (32,33).

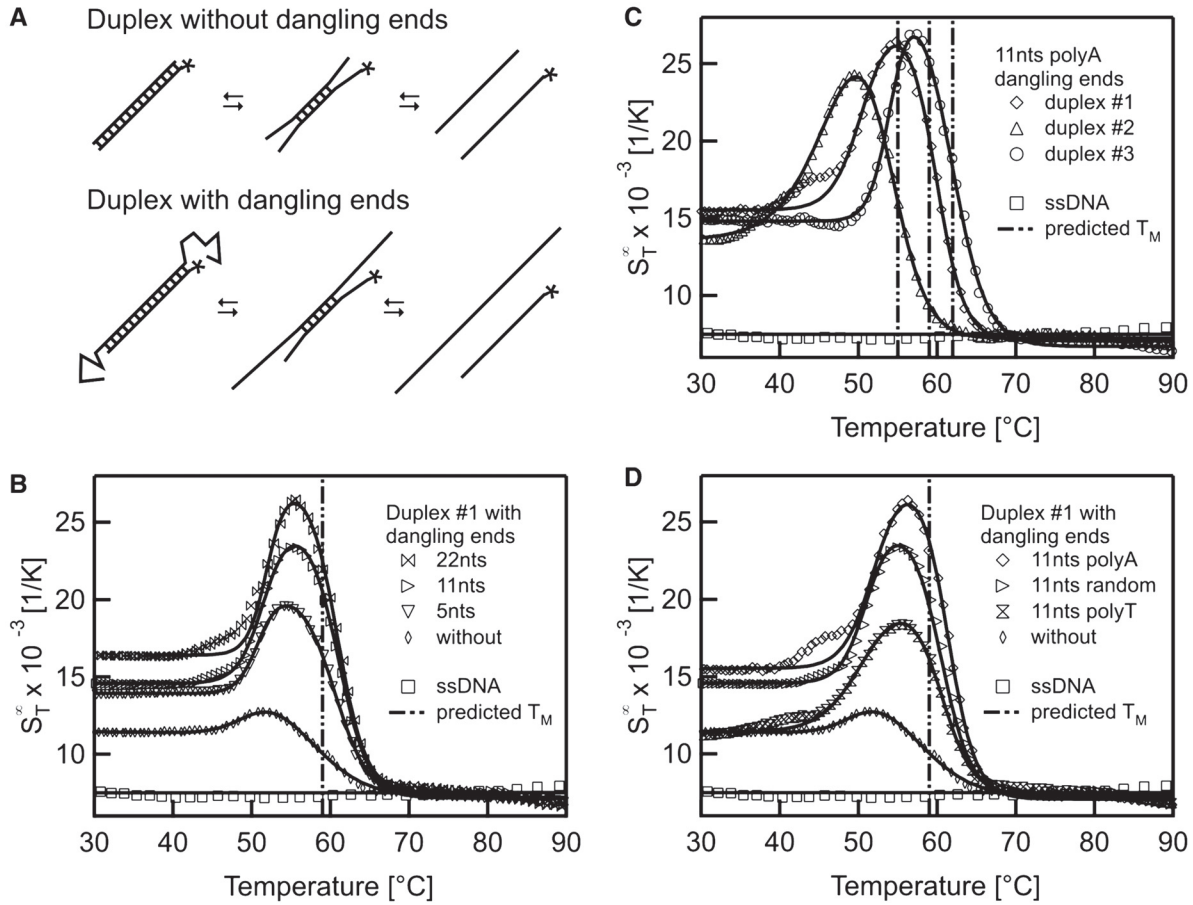

Figure 4. Effects of dangling ends. The melting of DNA double strands with dangling ends was analysed with thermophoresis. (**A**) As a hypothesis for the transition before the actual melting of the two DNA strands we propose an unbinding of the duplex-ends in a pre-melting transition. This 'end effects' should increase when adding overlapping DNA strands to both sides of one duplex strand. (**B**) The data for dangling ends of various length showed an increase of the Soret coefficient due to a change in the conformation before the actual melting transition. The final melting temperature matches the situation without dangling ends. (**C**) When changing the composition of the duplex forming sequence a shift in the melting temperature but also in the first transition was observed. (**D**) To rule out any potential structures of the dangling ends, duplex #1 was analysed with 11 nt overhangs of random sequence and compared to dangling ends with polyA and polyT sequence. Irrespective of the dangling ends, the melting temperature remained constant.

They may also play a role in modulating biological processes involving DNA (34). Concerning the stability of a duplex, dangling ends often alter the melting temperature but may also have no effect on the stability (23).

In Figure 4B the melting of a perfect match with dangling ends of various length is shown. For this experiment the sequence was kept constant but only the length of the dangling ends was varied. At low temperatures around 30°C a distinct difference in the S_T^{∞} was found for the perfect match and the asymmetric probes with dangling ends. With the addition of the dangling ends, the Soret coefficient raises as the molecule becomes larger. When melting a duplex with a 22 nt overhang on both sides the initial increase in the Soret coefficient was observed at 51.9 ± 0.1°C beside the melting into two single DNA strands at $T_m = 60.9 \pm 0.1$°C. These pre-melting transitions were obtained for dangling ends of all lengths at similar transition temperatures but with varying amplitude. Nearly no shift in the final melting temperatures was observed (11 nt: $T_m = 50.5 \pm 0.2$°C and $T_m = 60.0 \pm 0.1$°C; 5 nt: $T_m = 50.8 \pm 0.1$°C and $T_m = 60.6 \pm 0.1$°C). The height of the first transition increased with the length of the dangling ends. This indicates that the dangling ends form a more elongated structure prior to melting. This increases the surface of the molecules and thus the Soret coefficient.

To check whether the duplex forms a tertiary structure which melts at a given temperature, the analysis was performed with duplexes of changed composition (Figure 4C). In this case the dangling ends consisted of 11 nt polyA overlaps. The change of the duplex sequences led to a shift of the melting temperature from $T_m = 60.1 \pm 0.1$°C for duplex #1 to $T_m = 54.8 \pm 0.3$°C for duplex #2 and $T_m = 62.3 \pm 0.2$°C for duplex #3. These melting temperatures are in accordance with predicted values of 59 ± 1.4°C, 55 ± 1.4°C and 62 ± 1.4°C, respectively. Interestingly, a similar pre-melting transition is found for all duplexes, however shifted in accordance with the melting transition temperature (duplex #1: $T_m = 51.0 \pm 0.3$°C, duplex #2: $T_m = 45.6 \pm 0.4$°C,

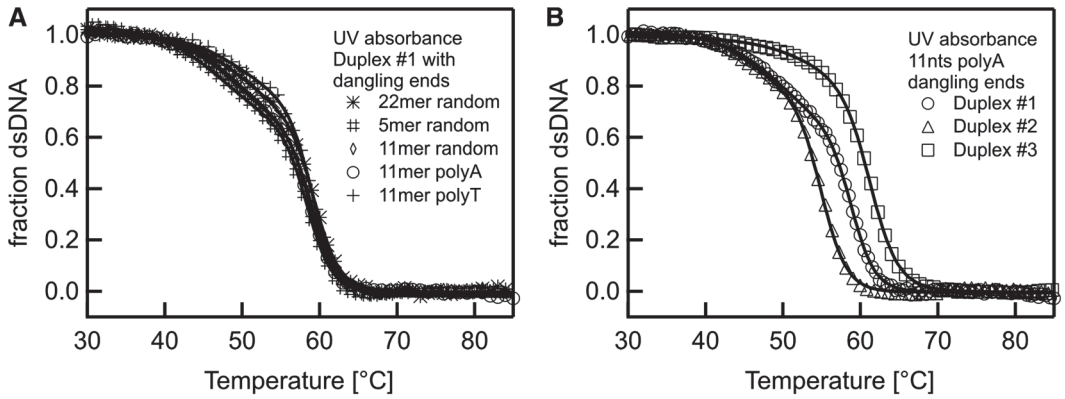

Figure 5. UV melting controls. Measurements with various dangling ends and duplex sequences confirm the thermophoretic melting curves. (**A**) The melting of double-stranded DNA (Figure 4) with dangling ends of various compositions was analysed with UV absorbance. As in the thermophoretic melting analysis, a deviation from the two-state model was observed although the first transitions were less pronounced than in the thermophoresis signal. Both melting transitions occurred at similar melting temperatures. (**B**) The duplex composition is varied while keeping the overlap of 11 nt fixed to a polyA structure. Both melting temperatures shift with the varied duplex sequence in accordance to the thermophoresis measurement of Figure 4C.

duplex #3: $T_m = 53.6 \pm 0.5°C$). This indicates that the rise in S_T^∞ is not due to a special tertiary structure only of duplex #1, but a sequence-independent common feature.

Finally, a possible special structure of the dangling ends itself could be ruled out. The sequence of a 11nt overlap was varied from a random sequence to polyA and polyT dangling ends, respectively (Figure 4D). Both transition temperatures remained constant (11 nt polyT: $T_m = 50.6 \pm 0.9°C$ and $T_m = 60.5 \pm 0.4°C$; 11 nt polyA: $T_m = 51.0 \pm 0.3°C$ and $T_m = 60.1 \pm 0.1°C$; 11 nt random: $T_m = 50.5 \pm 0.2°C$ and $T_m = 60.0 \pm 0.1°C$). This indicates that no (unpredicted) secondary or tertiary structure in the dangling ends exists. The height of the first transition was of comparable magnitude (random: 8.9×10^{-3} 1/K, polyA: 10.9×10^{-3} 1/K, polyT: 7.0×10^{-3} 1/K) but polyA dangling ends showed a slightly stronger signal than polyT dangling ends. This is in accordance with findings that polyA strands show a much higher persistence length compared to polyT strands and thus form more rigid dangling ends (35). Hence, the rise in S_T^∞ before the actual melting appears to be a natural intermediate state in the denaturing process.

In Figure 5 control experiments of above probes with dangling ends using UV absorbance are presented. The controls for duplex #1 with dangling ends of various length and composition showed a similar shape (Figure 5A). The curves also showed a deviation from a typical two state melting, but the tendency was less pronounced than in the thermophoretic melting curve. When fitting the UV curves with a three-state model, melting temperatures were obtained in a similar range as for the thermophoretic melting analysis. (random 22 nt: $50.6 \pm 0.3°C$ and $59.3 \pm 0.1°C$; random 11 nt: $49.4 \pm 0.3°C$ and $59.0 \pm 0.1°C$; random 5 nt: $47.4 \pm 0.3°C$ and $58.4 \pm 0.1°C$; polyA 11 nt: $49.4 \pm 0.2°C$ and $58.8 \pm 0.1°C$; polyT 11 nt: $50.2 \pm 0.4°C$ and $59.1 \pm 0.1°C$). When measuring 11 nt polyA dangling ends with varying duplex sequences a shift in the melting temperature was observed. This is in agreement with the thermophoretic melting curves (Figure 5B; duplex #1: $49.4 \pm 0.2°C$ and $58.8 \pm 0.1°C$; duplex #2: $46.1 \pm 0.5°C$ and $54.9 \pm 0.1°C$; duplex #3: $54.9 \pm 0.4°C$ and $61.2 \pm 0.1°C$). Deviations from a two-state behaviour were noticeable but less pronounced. Without the prior knowledge of a pre-melting transition, the rather small deviations from a two state model in the UV absorption signal would have been too insignificant to be analysed.

Conformational information

Tertiary structures formed by DNA often have a strong effect on possible interactions. They are known to enhance the affinity to the binding partner but can also reduce the binding strength due to steric shielding of the binding site (36). Hence, information on the stability of tertiary structures is desirable. In Figure 6, we show examples of obtaining purely conformational information from thermophoretic melting curves of structure-forming ssDNA molecules. In Figure 6A we show the melting of a hairpin with a double-stranded stem. In the thermophoretic melting curve, the Soret coefficient showed a first transition at $T_m = 55.8 \pm 0.8°C$, followed by a second transition at $T_m = 83.3 \pm 1.1°C$. The first transition could be attributed to an initial change of the tertiary structure while the second transition is likely due to the complete melting of the hairpin stem. The second transition was also observed with UV absorbance spectroscopy, but a different melting temperature of $T_m = 78.0 \pm 0.4°C$ was obtained. Compared to the theoretical prediction of $T_m = 64.3 \pm 1.4°C$ (21), the experimentally observed melting temperatures are considerably higher. This may be due to uncertainties of the thermodynamic calculations when analysing hairpin structures. Nevertheless, the melting of the DNA hairpin is measurable with thermphoresis. In Figure 6B the melting of a thrombin DNA aptamer is presented. This aptamer is known to form a G-quadruplex, but no duplex structures (37). When analysing the melting behaviour of this structure a clear transition was observed. The S_T^∞ increased when unfolding the quadruplex structure at

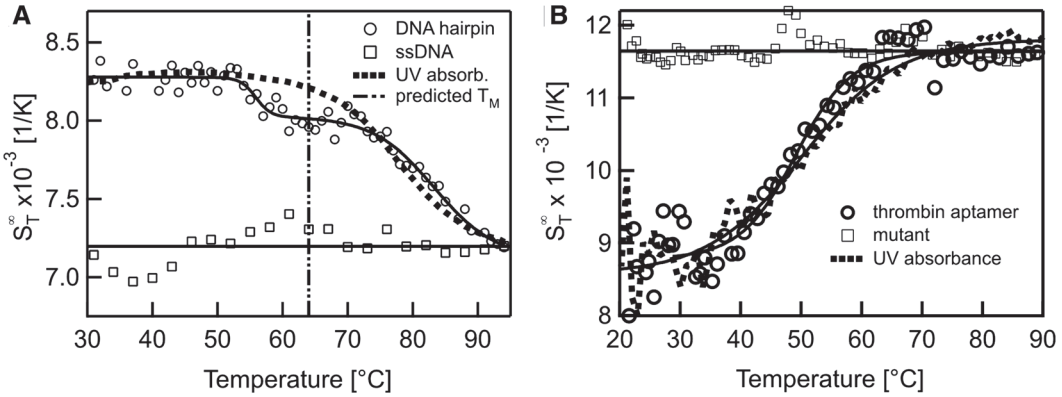

Figure 6. Structural information of DNA molecules. (**A**) The change in conformation of a DNA hairpin was resolved by evaluating its thermophoretic behaviour with temperature. We found a distinct deviation from a two-state behaviour, attributed to a breakage or re-orientation of the duplex structure. (**B**) As an example for a pure conformational melting signal, a DNA aptamer which is known to form a G-quadruplex was analysed with thermophoresis. It showed a clear transition without deviations from a two-state model.

$T_m = 49.2 \pm 0.4°C$. Such an increase was expected as the molecules change from a compact form in the G-quadruplex state to a more elongated form after melting which leads to an increased surface of the molecule. A control experiment with a mutated DNA sequence which does not form a quadruplex structure (14) showed no transition (Figure 6B, squares). The UV absorbance measurement yielded a $T_m = 50.1 \pm 0.3°C$ which is in good agreement with the thermophoretic measurement and literature (37). As expected, the change in conformation was readily detectable in the thermophoretic melting curve although no changes in mass or charge occured. The sensitivity to these kinds of conformational changes is attributed to the dependence of thermophoresis on changes in size or hydrophobicity.

RNA melting

The melting of RNA can be equally analysed with thermophoresis. Short non-coding RNA, for example, plays a fundamental role in cellular processes and regulates gene expression. It is the target of antisense oligonucleotides, which are primarily designed because of their ability to hybridize with the mRNA of interest (38,39). This mRNA has a complex secondary and tertiary structure that restricts the accessibility of certain segments. Therefore, it is interesting to investigate the stability of RNA duplexes used for RNA silencing and in parallel gather information about possible tertiary structures.

The shape of the thermophoretic melting curve for double-stranded RNA (Figure 7) also showed a deviation from standard two-state melting. A significant increase in the S_T^∞ in an initial transition ($T_m = 52.4 \pm 0.4°C$) was followed by a second transition to the single-stranded state ($T_m = 67.0 \pm 0.4°C$). In comparison to DNA the increase for RNA was considerably more pronounced. This could be attributed to the higher flexibility of single-stranded RNA which is significantly more polymorphic than DNA (40).

As for the case of DNA, the second downward transition was close to the theoretically predicted melting

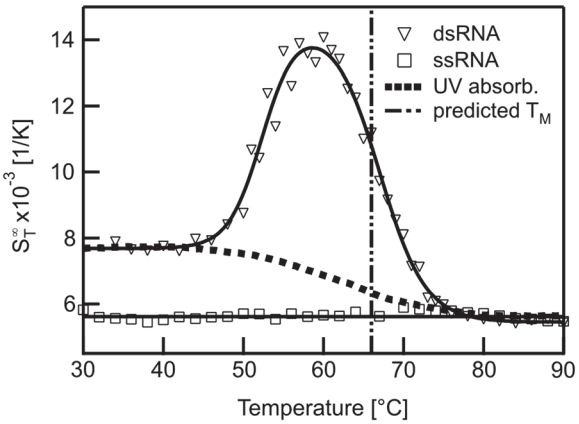

Figure 7. Melting of RNA duplexes. The melting of RNA showed a strong change in S_T^∞ before the actual melting occurs. This increase in S_T^∞ prior to melting for dsRNA was attributed to a partial melting of the double strand beginning at the ends of the RNA duplex. It was significantly larger for RNA as compared to DNA.

temperature of $T_m = 66 \pm 1.3°C$. Under close examination, the UV absorbance also revealed deviations from a two-state melting (Figure 7, filled squares). We found melting temperatures at $T_m = 54.1 \pm 1.4°C$ and $T_m = 65.0 \pm 0.9°C$, in close accordance to the results from the more pronounced thermophoresis signal.

Thermophoretic properties of nucleic acids

The presented data showed that the stability analysis of nucleic acids can be performed with thermophoresis. We found that the thermophoretic signal is not only sensitive to the hybridization state of nucleic acids. Moreover, the magnitude of the Soret coefficient provides information about the conformation, size and modification of the polynucleotides. The sensitivity readily allows the resolution of a single nucleotide mismatch for short ssDNA (13). Each of the investigated molecules featured a distinct S_T^∞ and yielded information about its molecular properties (Table 2). This implies that differences in the composition

Table 2. The Soret coefficient S_T^∞ and melting temperatures for various types of nucleic acids

Molecule	$S_T^\infty \times 10^{-3}$ (1/K)	T_m pre-melting transition (°C)	T_m melting transition (°C)
ssDNA	7.2 ± 0.1	–	–
22-mer hairpin	8.3 ± 0.1	55.8 ± 0.8	83.3 ± 1.1
Thrombin aptamer	8.7 ± 0.5	–	49.2 ± 0.4
Thrombin aptamer mutant	11.7 ± 0.1	–	–
Perfect match dsDNA	11.4 ± 0.1	49.7 ± 0.2	56.3 ± 0.1
Mismatched dsDNA	11.0 ± 0.4	36.3 ± 0.4	47.7 ± 0.9
Methylated dsDNA	9.4 ± 0.1	45.5 ± 0.7	53.6 ± 0.4
Duplex #1 with 22 nt random	16.4 ± 0.1	51.9 ± 0.1	60.9 ± 0.1
Duplex #1 with 11 nt random	14.6 ± 0.1	50.5 ± 0.2	60.0 ± 0.1
Duplex #1 with 5 nt random	13.8 ± 0.1	50.8 ± 0.1	60.6 ± 0.1
Duplex #1 with 11 nt polyT	11.6 ± 0.4	50.6 ± 0.9	60.5 ± 0.4
Duplex #1 with 11 nt polyA	15.7 ± 0.6	51.0 ± 0.3	60.1 ± 0.1
Duplex #2 with 11 nt polyA	13.7 ± 0.2	45.6 ± 0.4	54.8 ± 0.3
Duplex #3 with 11 nt polyA	14.8 ± 0.2	53.6 ± 0.5	62.3 ± 0.2
ssRNA	5.5 ± 0.1	–	–
dsRNA	7.7 ± 0.2	52.4 ± 0.4	67.0 ± 0.4

The thermophoretic effect provides information about the molecular properties of nucleic acids, both for DNA and RNA. Thus, thermophoresis not only discriminates molecules of different sizes but is sensitive to various conformations or modifications. The error in S_T^∞ represents the standard deviation of each data point calculated from five measurement points in the double-stranded regime.

of DNA strands lead to different S_T^∞ signals and thus are distinguishable with thermophoresis.

This sensitivity to size, charge and conformational structure can be used to identify a molecule only based on its Soret coefficient when compared to a calibration curve of a known species. Hence the Soret coefficient, together with the pre-melting and melting temperature can serve as a molecule's fingerprint, which can allow the identification of species in an unknown sample.

CONCLUSION

The experiments herein demonstrated that thermophoresis is a versatile tool for analysing the stability of nucleic acids. Beside the standard melting temperature T_m, the data showed that additional information about conformational states is accessible. This provides insights into the behaviour prior to melting. This additional information is especially important for RNA, where functionality highly relies on its tertiary structure. Due to its sensitivity to conformations, thermophoresis may thus help in the investigation of complex structures of nucleic acids and provide more detailed information about molecular processes.

Recently, Mast *et al.* (41) showed that the thermophoretic analysis of DNA is possible using intercalating fluorophores and that thermophoresis can be employed to quantify the length of PCR products. Based on these measurements, we expect that the presented thermophoretic measurements are also accessible with intercalating dyes.

To conclude, we have developed a sensitive, sample-efficient method for the analysis of the thermal stability of nucleic acids. Using 250 nl of sample, the cost for an analysis is low and thus, expensive or rare samples can be used sparingly. The technique requires only one fluorescently labelled oligonucleotide probe and no complex FRET probe pairs, further decreasing the cost and complexity of mutation-specific analysis. Furthermore, no special buffers are required to record thermophoresis signals and the buffer conditions can be chosen freely. The duration of the experiment is comparable to UV absorbance melting curve experiments. However, the experiment times could be shortened by reducing the equilibration time of the peltier elements and by acquiring thermophoretic depletion without recording the back-diffusion of the molecules.

The sensitivity of thermophoresis offers the possibility to resolve complex melting behaviours, and due to its additional information, the technique can provide more detailed insights into the interactions of nucleic acids. With its sensitivity for conformational states of the nucleic acids thermophoresis provides a promising experimental approach for testing biological models and allows for a more detailed understanding of the melting behaviour of biologically relevant nucleic acids.

ACKNOWLEDGEMENTS

The authors thank Hubert Krammer for help with the UV absorbance melting curves and Uta Steinbach and Ann Fornof for helpful discussions and for comments on the article. We also want to express our gratitude to the Center for Nanoscience (CeNS).

FUNDING

The LMU initiative Functional NanoSystems (FuNS); the Excellence Cluster NanoSystems Initiative Munich (NIM); NanoTemper Technologies GmbH. Funding for open access charge: Center for NanoScience (CeNS) and Ludwig-Maximilians-Universität München.

Conflict of interest statement. P.B. and S.D. are founders of the University Spin Off Company NanoTemper Technologies GmbH which provides services and devices based on thermophoresis. D.B. and C.J.W. declare no conflict of interests.

REFERENCES

1. Doty,P. (1957) The physical chemistry of deoxyribonucleic acids. *J. Cell Comp. Physiol.*, **49**, 27.
2. Marmur,J. and Doty,P. (1959) Heterogeneity in deoxyribonucleic acids: I. Dependence on composition of the configurational stability of deoxyribonucleic acids. *Nature*, **183**, 1427–1429.
3. Marmur,J. and Doty,P. (1962) Determination of the base composition of deoxyribonucleic acid from its thermal denaturation temperature. *J. Mol. Biol.*, **5**, 109–118.
4. Ansevin,A.T., Vizard,D.L., Brown,B.W. and McConathy,J. (1976) High-resolution thermal denaturation of DNA. I. Theoretical and

practical considerations for the resolution of thermal subtransitions. *Biopolymers*, **15**, 153–174.
5. Mergny,J.L. and Maurizot,J.C. (2001) Fluorescence resonance transfer as a probe for G-quartet formation by a telomeric repeat. *ChemBioChem*, **2**, 124–132.
6. Reed,G.H., Kent,J.O. and Wittwer,C.T. (2007) High-resolution DNA melting analysis for simple and efficient molecular diagnostics. *Pharmacogenomics*, **8**, 597–608.
7. Baaske,P., Duhr,S. and Braun,D. (2007) Melting curve analysis in a snapshot. *Appl. Phys. Lett.*, **91**, 133901.
8. Lyon,E. (2001) Mutation detection using fluorescent hybridization probes and melting curve analysis. *Expert Rev. Mol. Diagn.*, **1**, 92–101.
9. Thatcher,D.R. and Hodson,B. (1981) Denaturation of proteins and nucleic acids by thermal-gradient electrophoresis. *Biochem. J.*, **197**, 105–109.
10. Rosenbaum,V. and Riesner,D. (1987) Temperature-gradient gel electrophoresis thermodynamic analysis of nucleic acids and proteins in purified form and in cellular extracts. *Biophys. Chem.*, **26**, 235–246.
11. Ludwig,C. (1856) Diffusion zwischen ungleich erwärmten Orten gleich zusammengesetzter Lösungen. *Sitzungsber. Akad. Wiss. Wien: Math.-Naturwiss.*, **20**, 539.
12. Duhr,S. and Braun,D. (2006) Why molecules move along a temperature gradient. *Proc. Natl Acad. Sci. USA*, **103**, 19678–19682.
13. Reineck,P., Wienken,C.J. and Braun,D. (2010) Thermophoresis of single stranded DNA. *Electrophoresis*, **31**, 279–286.
14. Baaske,P., Wienken,C.J., Reineck,P., Duhr,S. and Braun,D. (2010) Optical thermophoresis for quantifying the buffer dependence of aptamer binding. *Angew. Chem. Int. Ed.*, **49**, 2238–2241.
15. Wienken,C.J., Baaske,P., Rothbauer,U., Braun,D. and Duhr,S. (2010) Protein binding assays in biological liquids using microscale thermophoresis. *Nat. Commun.*, **1**, 100.
16. Duhr,S. and Braun,D. (2006) Thermophoretic depletion follows Boltzmann distribution. *Phys. Rev. Lett.*, **96**, 168301.
17. Iacopini,S., Rusconi,R. and Piazza,R. (2004) The ''macromolecular tourist'': universal temperature dependence of thermal diffusion in aqueous colloidal suspensions. *Phys. J. E*, **19**, 59–67.
18. Mergny,J. and Lacroix,L. Analysis of thermal melting curves. *Oligonucleotides*, **13**, 515–537.
19. Duhr,S., Arduini,S. and Braun,D. (2004) Thermophoresis of DNA determined by microfluidic fluorescence. *Eur. Phys. J. E*, **15**, 277.
20. Skirtach,A.G., Déjugna,C., Braun,D., Susha,A.S., Rogach,A.L., Parak,W.J., Möhwald,H. and Sukhorukov,G.B. (2005) The role of metal nanoparticles in remote release of encapsulated materials. *Nano Lett.*, **7**, 1371–1377.
21. Zuker,M. (2003) Mfold web server for nucleic acid folding and hybridization prediction. *Nucleic Acids Res.*, **31**, 3406.
22. SantaLucia,J. and Hicks,D. (2004) The thermodynamics of DNA structural motifs. *Annu. Rev. Biophys. Biomol. Struct.*, **33**, 415–440.
23. Bommarito,S., Peyret,N. and Santa Lucia,J. (2000) Thermodynamic parameters for DNA sequences with dangling ends. *Nucleic Acids Res.*, **28**, 1929–1934.
24. Allawi,H. and SantaLucia,J. (1998) Nearest neighbor thermodynamic parameters for internal G-A mismatches in DNA. *Biochemistry*, **36**, 10581–10594.
25. Patil,S.D., Rhodes,D.G. and Burgess,D.J. (2005) DNA-based therapeutics and DNA delivery systems: a comprehensive review. *AAPS J.*, **7**, E61–E77.
26. Crooke,S.T. (1999) Molecular mechanisms of action of antisense drugs. *Biochim. Biophys. Acta*, **1489**, 31–43.
27. Robertson,K.D. and Wolffe,A.P. (2000) DNA methylation in health and disease. *Nat. Rev. Gen.*, **1**, 11–19.
28. Li,E., Bestor,T.H. and Jaenisch,R. (1992) Targeted mutation of the DNA methyltransferase gene results in embryonic lethality. *Cell*, **69**, 915–926.
29. Okano,M., Bell,D.W., Haber,D.A. and Li,W. (1999) DNA methyltransferases *Dnmt3a* and*Dnmt3b* are essential for *de novo* methylation and mammalian development. *Cell*, **99**, 247–257.
30. Baylin,S.B., Herman,J.G., Herman,J.R., Vertino,P.M. and Issa,J.-P. (1998) Alterations in DNA methylation: a fundamental aspect of neoplasia. *Adv. Cancer Res.*, **72**, 141–196.
31. Post,W.S., Goldschmidt-Clermont,P.J., Wilhide,C.C., Heldman,A.W., Sussman,M.S., Ouyang,P., Milliken,E.E. and Issa,J.J. (1999) Methylation of the estrogen receptor gene is associated with aging and atherosclerosis in the cardiovascular system. *Cardiovasc. Res.*, **43**, 985–991.
32. Grosjean,H., Soll,D.G. and Crothers,D.M. (1976) Studies of the complex between transfer RNAs with complementary anticodons: I. Origins of enhanced affinity between complementary triplets. *J. Mol. Biol.*, **103**, 499.
33. Yoon,K., Turner,D.H., Tinoco,I., von der Haar,F. and Cramer,F. (1976) The kinetics of binding of U-U-C-A to a dodecanucleotide anticodon fragment from yeast $tRNA^{Phe}$. *Nucleic Acids Res.*, **3**, 2233–2242.
34. Senior,M., Jones,R.A. and Breslauer,K.J. (1988) Influence of dangling thymidine residues on the stability and structure of two DNA duplexes. *Biochemistry*, **27**, 3879–3885.
35. Millsa,J.B., Vacanoa,E. and Hagerman,P.J. (1999) Flexibility of single-stranded DNA: use of gapped duplex helices to determine the persistence lengths of Poly(dT) and Poly(dA). *J Mol. Biol.*, **285**, 245–257.
36. Travers,A.A. (1989) DNA conformation and protein binding. *Annu. Rev. Biochem.*, **58**, 427–452.
37. Kankia,B.I. and Marky,L.A. (2001) Folding of the thrombin aptamer into a G-quadruplex with Sr(2+): stability, heat, and hydration. *J. Am. Chem. Soc.*, **123**, 10799–10804.
38. Kim,V.N. (2005) MicroRNA biogenesis: coordinated cropping and dicing. *Nat. Rev. Mol. Cell Biol.*, **6**, 376–385.
39. He,L. and Hannon,G.J. (2004) MicroRNAs: small RNAs with a big role in gene regulation. *Nat. Rev. Genet.*, **5**, 522–531.
40. Pan,Y.P. and MacKerell,A.D. (2003) Altered structural fluctuations in duplex RNA versus DNA: a conformational switch involving base pair opening. *Nucleic Acids Res.*, **31**, 7131–7140.
41. Mast,C.B. and Braun,D. (2010) Thermal trap for DNA replication. *Phys. Rev. Lett.*, **104**, 188102.

Peptide surfactants for cell-free production of functional G protein-coupled receptors

Xiaoqiang Wang[a,b,1], Karolina Corin[a,1], Philipp Baaske[c], Christoph J. Wienken[d], Moran Jerabek-Willemsen[d], Stefan Duhr[c], Dieter Braun[d], and Shuguang Zhang[a,2]

[a]Center for Biomedical Engineering NE47-379, Massachusetts Institute of Technology, 77 Massachusetts Avenue, Cambridge, MA 02139-4307; [b]Center for Bioengineering and Biotechnology, China University of Petroleum (East China), Qingdao, Shandong 266555, People's Republic of China; [c]NanoTemper Technologies GmbH, Amalienstrasse 54, 80799 Munich, Germany; and [d]Systems Biophysics, Functional Nanosystems, Department of Physics, Ludwig-Maximilians University Munich, Amalienstrasse 54, 80799 Munich, Germany

Edited* by Alan R. Fersht, Medical Research Council Laboratory of Molecular Biology, Cambridge, United Kingdom, and approved March 29, 2011 (received for review December 10, 2010)

Two major bottlenecks in elucidating the structure and function of membrane proteins are the difficulty of producing large quantities of functional receptors, and stabilizing them for a sufficient period of time. Selecting the right surfactant is thus crucial. Here we report using peptide surfactants in commercial *Escherichia coli* cell-free systems to rapidly produce milligram quantities of soluble G protein-coupled receptors (GPCRs). These include the human formyl peptide receptor, human trace amine-associated receptor, and two olfactory receptors. The GPCRs expressed in the presence of the peptide surfactants were soluble and had α-helical secondary structures, suggesting that they were properly folded. Microscale thermophoresis measurements showed that one olfactory receptor expressed using peptide surfactants bound its known ligand heptanal (molecular weight 114.18). These short and simple peptide surfactants may be able to facilitate the rapid production of GPCRs, or even other membrane proteins, for structure and function studies.

in vitro translation | label-free

Membrane proteins play vital roles in all living systems. Approximately 30% of genes in almost all sequenced genomes code for membrane proteins (1–3). However, our detailed understanding of membrane protein structure and function lags far behind that of soluble proteins. Indeed, as of April 2011, there are over 72,000 structures in the Protein Data Bank. Of these, only 280 are unique membrane proteins, and only six are unique G protein-coupled receptors (GPCRs). This surprising disparity is due to bottlenecks at nearly every stage of experimentation, from large-scale membrane protein production to X-ray crystal diffraction.

Recent advances have overcome several bottlenecks in studying membrane proteins. Commercial development of nanoliter drop-setting robots and a wide variety of kits have made crystal screening less laborious. The development of worldwide accessible synchrotron facilities, and microfocus beamlines capable of collecting data from crystals <10–60 μm, have overcome the bottlenecks in data collection. Likewise, rapid advancements in computing power and an increase in open access software development have made the determination of structures a much less daunting task. However, inexpensive large-scale production of soluble and nonaggregated membrane proteins still remains a formidable challenge. Likewise, systematic surfactant screens still remain one of the most time-consuming and expensive experimental tasks. To overcome these bottlenecks, the discovery or invention of simple and broadly useful surfactants is crucial.

Several cell-based membrane protein production systems have been developed, but they are costly and require months to generate sufficient quantities of protein. Commercial cell-free systems are alternative methods of producing membrane proteins. However, to produce nonaggregated membrane proteins, optimal selection of surfactants is critical: The newly produced membrane proteins must not only fold correctly, they must also remain soluble and biologically functional. Until now, finding an appropriate surfactant for specific membrane proteins has been laborious, because even highly related proteins may react differently to the same detergent. It would be advantageous if a class of simple surfactants could be used for stabilizing diverse membrane proteins.

We previously reported the invention of a class of short peptide surfactants (4–8). We also reported that these peptides effectively stabilized the transmembrane protein glycerol-3-phosphate dehydrogenase (9), the photosystem-I protein complex (10, 11), and the G protein-coupled receptor bovine rhodopsin (12). We recently asked if these peptides could also be used in cell-free production of membrane proteins, particularly bioengineered olfactory receptors (13), trace amine-associated receptors (14), and formyl peptide receptors (15–17).

Here we report using commercially available *Escherichia coli* cell-free kits with our peptide surfactants (Fig. 1) to rapidly produce four GPCRs in milligram quantities. The surfactant property of the peptides was necessary to yield soluble GPCRs. They not only solubilized and stabilized the GPCRs, they also facilitated the proper folding of these receptors. Moreover, the cell-free produced olfactory receptor mOR103-15 was able to bind its odorant ligand heptanal [molecular weight (MW) 114.18], suggesting that the receptor is biologically functional. Our results indicate that these short and simple peptide surfactants may be a general class of surfactants that can facilitate the production of a wider range of GPCRs, and perhaps other membrane proteins.

Results

We previously achieved expression of olfactory receptors hOR17-4, mOR23, and mS51, using the Roche wheat germ cell-free protein production technology (18). However, the Roche system is expensive and requires a special apparatus to use, making it unaffordable for most laboratories. To attract more people to study membrane proteins, a rapid, affordable, and commercially available production method is needed. In this study, we were able to produce milligram quantities of four GPCRs using commercial *E. coli* cell-free systems. The receptors include the olfactory receptors (ORs) hOR17-210 and mOR103-15, the human formyl peptide receptor 3 (hFPR3) (15–17), and the human trace amine-associate receptor 5 (hTAAR5) (14).

Author contributions: X.W., K.C., D.B., and S.Z. designed research; X.W., K.C., P.B., C.J.W., M.J.-W., and S.D. performed research; X.W., K.C., P.B., C.J.W., M.J.-W., and S.D. contributed new reagents/analytic tools; X.W., K.C., P.B., C.J.W., M.J.-W., S.D., D.B., and S.Z. analyzed data; and X.W., K.C., P.B., D.B., and S.Z. wrote the paper.

The authors declare no conflict of interest.

*This Direct Submission article had a prearranged editor.

[1]X.W. and K.C. contributed equally to this work.

[2]To whom correspondence should be addressed. E-mail: shuguang@mit.edu.

This article contains supporting information online at www.pnas.org/lookup/suppl/doi:10.1073/pnas.1018185108/-/DCSupplemental.

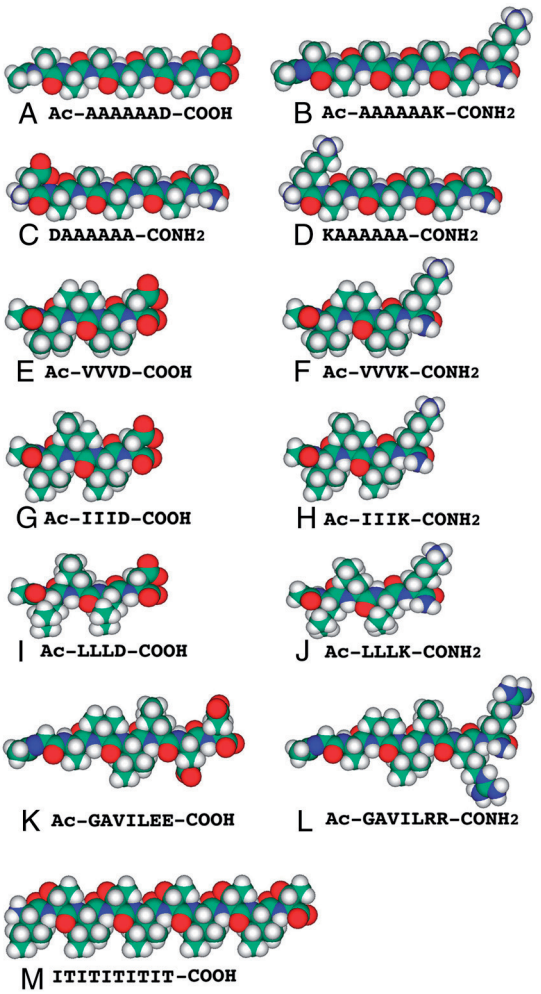

Fig. 1. Molecular models of the peptide surfactants and nonsurfactant peptide at pH 7.5. The peptide sequences are under each molecular model. Aspartic acid (D) and glutamic acid (E) are negatively charged whereas arginine (R) and lysine (K) are positively charged. The hydrophobic tails of the peptide surfactants consist of glycine (G), alanine (A), valine (V), isoleucine (I), and leucine (L). Each peptide surfactant is approximately 2–2.5 nm long, similar to biological phospholipids. Color code: teal, carbon; red, oxygen; blue, nitrogen; and white, hydrogen.

The Effect of Peptide Surfactants for Cell-Free GPCR Expression and Solubility. We systematically screened 12 peptide surfactants with hOR17-210, mOR103-15, hFPR3, and hTAAR5 in a commercial *E. coli* cell-free expression system. Western blotting was used to quantify protein expression. Fig. 2 shows the results for hFPR3 and hOR17-210. Very little soluble protein was produced without a peptide surfactant. Although high yields were consistently achieved with several peptides, the total yield depended on both the specific protein and the specific peptide. For example, the peptide Ac-GAVILRR-NH_2 consistently yielded low levels of receptor, whereas high levels were consistently achieved with the peptide Ac-A_6D-OH. In contrast, receptor yields with Ac-I_3K-NH_2 and Ac-A_6K-NH_2 were variable. Low expression levels in the presence of the nonsurfactant peptide $(IT)_5$ demonstrate the necessity of using a surfactant with the GPCRs. However, the low expression levels in the presence of several surfactant peptides indicate that a surfactant character for the peptides is necessary, but not sufficient.

Fig. 3 shows that the peptide surfactants solubilized the tested GPCRs, but with varying effectiveness. This efficacy depended on both the peptide and the specific GPCR. The receptors hFPR3 and hTAAR5 consistently had 60–90% of the total synthesized

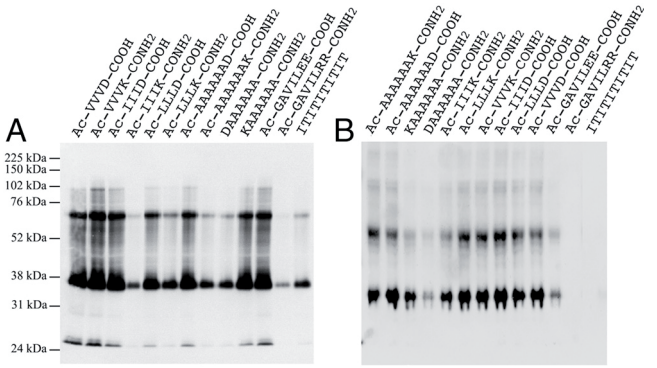

Fig. 2. Western blotting detection of cell-free produced GPCRs. After the reactions, the samples were centrifuged. The supernatant containing the solubilized protein was removed, and the pellet was resuspended in an equivalent volume of buffer. The solubilized protein and resuspended pellets were detected by Western blotting. As controls, reactions with no peptide or the nonsurfactant peptide $(IT)_5$ were performed. (*A*) Western blot of solubilized hFPR3 in the presence of different peptides. (*B*) Western blot of solubilized hOR17-210 produced in the presence of different peptides. Similar results were obtained with hTAAR5 and mOR103-15.

monomer solubilized, whereas hOR17-210 and mOR103-15 were highly soluble in the presence of only three peptides. The peptides KA_6-NH_2, Ac-A_6K-NH_2, and Ac-V_3K-NH_2 were able to solubilize more than 70% of at least three GPCRs, whereas Ac-A_6K-NH_2 and Ac-A_6D-OH were able to solubilize 80–90% of two GPCRs. The peptides Ac-GAVILRR-NH_2, DA_6-NH_2, and Ac-I_3D-OH were least efficient at solubilizing the GPCRs, particularly the olfactory receptors. The controls demonstrated that the presence of a surfactant was necessary for GPCR solubilization. Interestingly, the peptide $(IT)_5$, which has alternating hydrophobic isoleucine and hydrophilic serine residues, was also able to solubilize some proteins. However, unlike the peptide surfactants, it seemed to inhibit protein synthesis.

The Maximum Yields of Cell-Free Produced GPCRs. Western blotting was used to estimate protein yields from the cell-free reactions

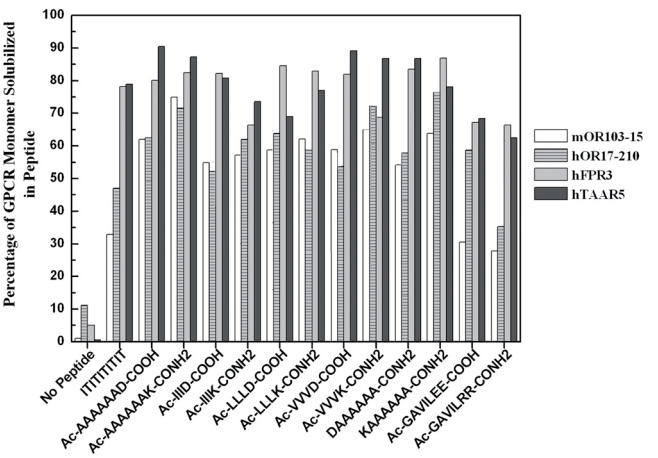

Fig. 3. Comparison of the solubility of four GPCRs in 12 different peptide surfactants. Each GPCR was expressed in the presence of surfactant peptides using an *E. Coli* cell-free protein expression system. Upon completion, reactions were centrifuged to separate solubilized protein from aggregate. The soluble fraction was removed, and the pellet was resuspended in an equivalent volume of buffer. Solubilized and nonsolubilized protein fractions were assayed using a Western blot; relative band intensities were used to calculate the percentage of solubilized protein. As controls, reactions with no peptide or with the nonsurfactant peptide $(IT)_5$ were performed. The presence of any peptide increased the fraction of solubilized protein. However, significant quantities of solubilized protein were only obtained in the presence of surfactant peptides.

using a known protein concentration as a standard reference. Fig. 4 shows that cell-free synthesis in the presence of peptide surfactants can yield a few milligrams of receptor per 10 mL reaction, and may thus be a good alternative for large-scale membrane protein production. However, as with the solubilization results, the protein yield depends on both the specific GPCR and the specific peptide surfactant used (Fig. 4 and Table S1). At least approximately 2 mg of three purified GPCRs could be produced in a 10 mL reaction with three of the peptide surfactants. The peptide Ac-A_6D-OH yielded the largest amounts of protein, with a maximum yield of approximately 4.8 mg for mOR103-15. Five other peptides were able to exceed 2.5 mg of purified receptors per 10 mL reaction for at least one GPCR: Ac-I_3D-OH, Ac-L_3K-NH_2, Ac-V_3D-OH, Ac-V_3K-NH_2, and Ac-GAVILEE-OH. The peptide Ac-GAVILRR-NH_2 consistently gave low protein yields for all receptors except hTAAR5. Overall, at least 2 mg of each purified receptor could be synthesized in a 10 mL reaction in the presence of at least one of the peptide surfactants. The control experiments demonstrate that the presence of a peptide is necessary for protein synthesis. The $(IT)_5$ control further indicates that surfactant properties are necessary for sufficient GPCR yields.

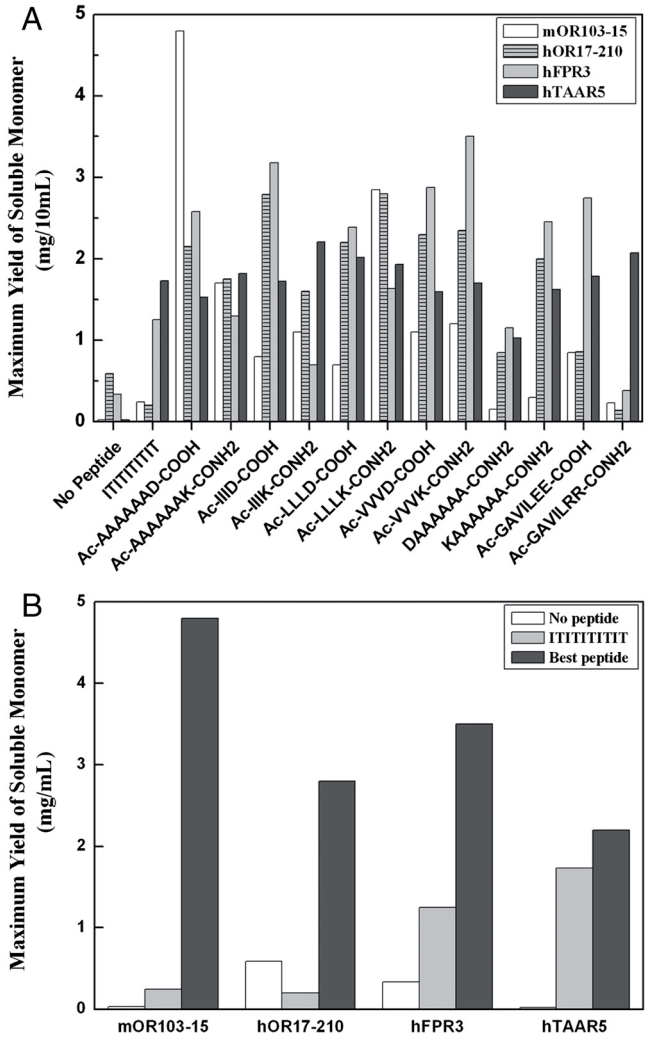

Fig. 4. The maximum expected yields of soluble receptors produced in the presence of peptide surfactants. (*A*) The maximum expected yields of solubilized monomer for each GPCR in the presence of each peptide or control condition. To determine the expected yields, solubilized protein and protein with a known concentration were assayed on a Western blot. The relative intensities of the known protein sample and the test samples were used to calculate the maximum protein yields. Surfactant peptides increased the yield of the solubilized monomeric form of the tested GPCRs. (*B*) The maximum yield of the monomeric form of each tested GPCR in a 10 mL reaction. Results from the most effective surfactant peptide are shown; it is compared to the maximum expected yield without peptide, or with a nonsurfactant peptide. The yield for each receptor varies with peptide surfactants used.

Our results show that the presence of peptide surfactants is necessary to achieve both high solubility and high protein yields (Figs. 3 and 4). They further suggest that the peptide surfactants may have a preference for different receptors, perhaps due to the nature of their composition and structure. For example, the different yields in Ac-A_6D-OH vs. DA_6-NH_2, or Ac-A_6K-NH_2 vs. KA_6-NH_2 suggest that the ionic character of the peptide is important. Our results suggest that ionic peptides yield more protein than zwitterionic peptides when the head group is negatively charged. However, when the head group is positively charged, a trend with the tested GPCRs is not visible. It is also possible that the peptide batch or structural phase can affect their ability to act as surfactants. Several investigators have observed that the peptides form dynamic structures in aqueous phase, changing between micelles, vesicles, nanotubes, and other structures (4–8, 19, 20). It is possible that different mesoscale peptide phases affect protein production and solubility, and more research is required to elucidate these effects. Because a large number of diverse peptide surfactants can be designed, it may be possible to engineer a peptide that works well for a specific receptor.

Secondary Structural Analysis Using CD. CD was used to verify that the cell-free produced receptors were properly folded, and that the peptide surfactants did not significantly affect the receptors' structures. In these experiments, the GPCRs were purified with fos-choline-14 (FC-14) because the peptide CD signal interferes with and overwhelms the receptor signals, and also because FC-14 has successfully been used with diverse GPCRs (21–24). Fig. 5 shows the CD spectra of each receptor. These purified receptors have characteristic α-helical structures, with signature minima at 220 and 208 nm. Because GPCRs are expected to have seven transmembrane helical domains, these CD spectra indicate that the receptors are properly folded.

Ligand Binding Measurements of Purified GPCRs Using Microscale Thermophoresis. Next, we tested whether the purified GPCRs were able to bind to their ligands. Microscale thermophoresis, a technique, which uses temperature gradients to measure ligand binding, was used because it can detect interactions between small ligands and large receptors in free solution (25–27). Because odorants are less than 300 Da whereas their receptors are greater than 300 kDa, mass-based measurements like quartz crystal microbalance cannot be used. As negative controls, boiled receptors were used to rule out the possibility of nonspecific binding or surfactant interference.

Fig. 6 shows that peptide-produced mOR103-15 bound its ligand heptanal (MW 114.18), whereas the boiled control did not. The peptide surfactant-produced sample displayed a typical sigmoidal binding curve, with a half maximal effective concentration (EC_{50}) of approximately 0.9 μM. In contrast, the boiled control did not show any significant differences between low and high ligand concentrations. These results suggest that peptide surfactants can be used to produce soluble and functional GPCRs.

Discussion

Peptide Surfactants for Membrane Protein Studies. Surfactants play an indispensible role in the study of membrane proteins, as their presence is necessary to solubilize and stabilize these proteins outside of their native membrane environment. The choice of surfactant is crucial. Previous studies showed that the most successfully used surfactants in crystallization experiments have short hydrophobic tails about 6–12 carbons in length (28). However, the surfactants that are often best for crystallization can

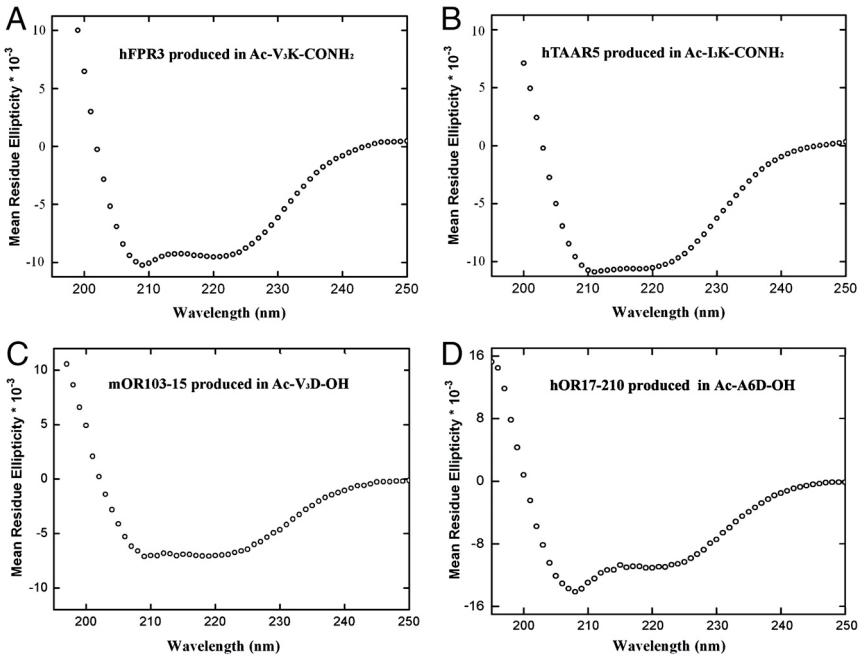

Fig. 5. CD spectra of four GPCRs produced in the presence of peptide surfactants using a commercial *E. coli* cell-free system. (*A*) hFPR3 produced in Ac-VVVK-$CONH_2$. (*B*) hTAAR5 produced in Ac-IIIK-$CONH_2$. (*C*) mOR103-15 produced in Ac-VVVD-OH. (*D*) hOR17-210 produced in Ac-AAAAAAD-OH. These receptors all have characteristic α-helical spectra with valleys at 208 and 222 nm. Because GPCRs have 7-transmembrane α-helical domains, the CD spectra indicate that the receptors are properly folded.

destabilize some membrane proteins. Careful surfactant screening of individual membrane proteins is thus necessary.

Surfactant peptides are a class of molecules with properties similar to those of surfactants that have successfully been used for crystallization. They have hydrophilic heads comprised of 1–2 residues, and hydrophobic tails 3–6 residues long. They are about 2–3 nm in length, and their ionic character and strength can be controlled by selecting appropriate amino acids or by capping the termini. Additionally, they have shown potential for use with membrane proteins (9–12). They have been used to solubilize glycerol-3-phosphate dehydrogenase, and to stabilize bovine rhodopsin and subunits of the photosystem I protein complex (9–12).

To evaluate the potential of peptide surfactants to be used with membrane proteins, we screened four GPCRs with 12 different peptides. Our current study suggests that these peptides may represent a class of surfactants that can aid in the solubilization and stabilization of GPCRs. The milligram protein yields we obtained further suggest that cell-free protein synthesis performed in the presence of peptide surfactants is a rapid, efficient, and relatively cost-effective means of producing the milligram quantities of membrane proteins necessary for structure and function studies. CD spectroscopy measurements of the GPCRs showed that the peptides facilitate proper protein folding, whereas microscale thermophoresis indicates that the peptide-produced proteins are functional.

Perspective. The studies reported here suggest that peptide surfactants are versatile, and can be used with a wider range of GPCRs. Their ease of use with commercially available protein production kits further underscores their value: They can now be used to produce milligram quantities of properly folded and functional GPCRs. Future experiments need to be performed to determine

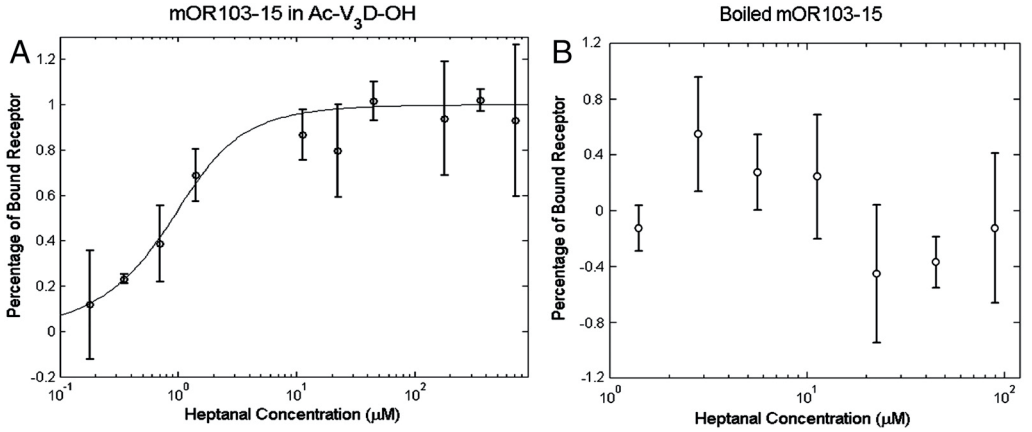

Fig. 6. Microscale thermophoresis ligand binding measurements of mOR103-15 produced in Ac-VVVD-OH. (*A*) Peptide-produced mOR103-15 has a sigmoidal shape, suggesting that the receptor binds to its ligand heptanal (MW 114.18). The measured EC_{50} is approximately 0.9 μM. (*B*) The boiled control showed fluctuations around a centerline, suggesting that binding observed with the normal receptor is not a result of nonspecific binding to the surfactant or denatured receptor. All curves were normalized to the fraction of bound receptor. Open circles show the mean measurements from three experiments; the lines through the points are the best-fit curves using the Hill equation.

whether a single peptide or a cocktail of several peptides are optimal surfactants for a given membrane protein. Future experiments are also needed to determine whether these surfactants can be useful for membrane protein crystallization. Our studies and previous research (9–12) suggest that peptide surfactants are a promising material not only for membrane protein studies, but also in the development of GPCR-based nanodevices.

Materials and Methods

Peptide Design and Synthesis. Peptide surfactants are comprised of a hydrophilic head and a hydrophobic tail. Three kinds of surfactant peptides were designed and used in this study: cationic, anionic, and zwitterionic. The ionic nature of the peptides was controlled by acetylation at the N terminus, amidation at the C terminus, or both. It was further controlled by choosing positively charged lysine or negatively charged asparatic acid for the head group. The length of hydrophobic tail ranged from three to six amino acids. As a control, the nonsurfactant peptide $(IT)_5$ was also designed and used. Molecular models of the surfactant peptides and control are shown in Fig. 1.

All peptides were commercially synthesized and purified by CPC Scientific, Inc. The peptides were received as a powder and dissolved in Milli-Q water before use. Each peptide suspension was sonicated, and the pH value was adjusted above 7.0 with NaOH or HCl solutions to increase peptide solubility. The suspension was then filtered through a 0.22 μm filter to remove insoluble particles. The filtered peptide solution was kept at room temperature (RT) as a stock solution.

Determination of CACs of Peptide Surfactants. To determine the critical aggregation concentration (CAC) of the peptides, two methods were used: electrical conductivity and surface tension. For each peptide surfactant, 30 serial dilutions were prepared in Milli-Q water (resistivity >18 MΩ·cm). The CACs of the cationic peptide surfactants (Ac-AAAAAAK-$CONH_2$, KAAAAAA-$CONH_2$, Ac-VVVK-$CONH_2$, Ac-IIIK-$CONH_2$, Ac-LLLK-$CONH_2$, and Ac-GAVILRR-$CONH_2$) were determined by electrical conductivity measurements using a conductivity meter (model DDS-307) at $25.0 + 0.1$ °C. Because of their relatively low solubility in Milli-Q water, the anionic and zwitterionic peptide solutions (Ac-AAAAAAD, Ac-VVVD, Ac-IIID, Ac-LLLD, Ac-GAVILEE, and DAAAAAA-$CONH_2$) were adjusted to pH 9.0 before surface tension measurements were employed to determine their CACs. The surface tension measurements were carried out with the EasyDyne tensiometer (Kruss) at 25.0 ± 0.1 °C by using the Wilhelmy plate method. The values of surface tension γ were determined after a period of 10 min to ensure equilibration conditions. The CACs are shown in Table S2.

GPCR DNA Template Design and Construction. Protein sequences of the following four GPCRs were obtained from the National Center for Biotechnology Information online database: hOR17-210 (UniProt release no. Q8WZA6), mOR103-15 (NP release no. 035113.1), hTAAR5 (NP release no. 003958.2), and hFPR3 (NP release no. 002021.3). To adapt the GPCRs for detection and purification, the rho1D4 epitope tag (TETSQVAPA) was added to their C termini. Codons of the engineered GPCRs were optimized for expression in *E. coli*. The genes were then commercially synthesized and subcloned into the pIVEX2.3d vector (Roche Diagnostics Corp.) by GENEART. The final constructs were verified by DNA sequencing and were used for all subsequent studies.

Cell-Free GPCR Production. *E. coli*-based cell-free expression kits were purchased from Invitrogen (catalog no. K9900-97, Qiagen 32506). To compensate for the lack of a natural membrane, surfactant peptides were added directly to the reactions. The experimental concentrations of each peptide surfactant for each GPCR are shown in Table S2. A final reaction volume of 25 μL was used for all screens.

Systematic Screen of Peptide Surfactants. Six pairs of surfactant peptides were used in the cell-free production of GPCRs. As a control, the nonsurfactant peptide $(IT)_5$ was also used. The surfactant peptides were all tested at concentrations above their determined or estimated CACs. Cell-free reactions were performed according to the manufacturers instructions. Briefly, plasmid DNA, peptide, and the reaction reagents were incubated at 33 °C and 260 rpm for 30 min. A feed buffer was then added, and the reaction was incubated for an additional 90 min. The samples were then centrifuged at 10,000 rpm for 5 min. The supernatant containing the solubilized protein was removed, and the pellet was resuspended in an equivalent volume of PBS. The quantity of each protein produced and solubilized was determined with Western blotting.

Western Blotting Detection of rho1D4 Tagged GPCRs. Samples were prepared and loaded in Novex 10% Bis-Tris SDS-PAGE gels (Invitrogen) according to the manufacturer's protocol, with the exception that the samples were incubated at RT prior to loading as boiling causes membrane protein aggregation. The Full-Range Rainbow Molecular Weight Marker (GE Healthcare) was loaded as the protein size standard. After the samples were resolved on the SDS-PAGE gels, they were transferred to a 0.45 μm nitrocellulose membrane, blocked in milk [5% nonfat dried milk in Tris-buffered saline plus Tween-20 (TBST), 1 h, RT], and incubated with a rho1D4 primary antibody (1:3,000 in TBST, 1 h, RT). The GPCRs were then detected with a goat anti-mouse HRP-conjugated secondary antibody (Pierce) (1:5,000 in TBST, 1 h, RT) and visualized using the ECL Plus kit (GE Healthcare). Western blotting images were captured using a FluorChem gel documentation system (Alpha Innotech).

Immunoaffinity Purification. We used the rho1D4 monoclonal antibody (Cell Essentials) chemically linked to CNBr-activated Sepharose 4B beads (GE Healthcare). The rho1D4 elution peptide Ac-TETSQVAPA-$CONH_2$ was synthesized by CPC Scientific, Inc. Solubilized protein from the cell-free reactions was mixed with a rho1D4-coupled sepharose bead slurry (binding capacity 0.7 mg/mL) and rotated overnight at 4 °C to capture the GPCRs. The beads were pelleted by centrifugation at 1,400 g for 1 min. The beads were then washed with wash buffer (PBS + 0.2% FC-14) until spectrophotometer readings indicated that all excess protein had been removed (mg/mL < 0.01). The captured GPCRs were eluted with elution buffer (PBS + 0.2% FC-14 + 800 μM elution peptide). Elutions were performed until spectrophotometer readings indicated no more protein was present (mg/mL < 0.01). The protein was then concentrated using a 30 kDa molecular weight cut-off filter column (Millipore) and its concentration was measured using the NanoDrop 1000 spectrophotometer (Thermo Scientific).

Secondary Structure Analysis by CD Spectroscopy. Spectra were recorded on a CD spectrometer (Aviv Associates model 410) at 15 °C over the wavelength range of 195 to 250 nm with a step size of 1 nm and an averaging time of 4 s. Spectra for purified GPCRs were blanked to wash buffer. Spectra were collected with a 111-QS quartz sample cell (Hellma) with a path length of 1 mm. The spectra were smoothed using an averaging filter with a span of five.

Microscale Thermophoresis Ligand Binding Measurements. Binding interactions between the purified mOR103-15 and the ligand heptanal (MW 114.18) were measured using microscale thermophoresis as described (24–27). Briefly, for each tested receptor, a titration series with constant receptor concentration and varying ligand heptanal (MW 114.18) concentrations was prepared in a final solution of 10% DMSO and 0.2% FC-14 in PBS. Approximately 1.5 μL of each sample was loaded in a fused silica capillary (Polymicro Technologies). An infrared laser diode was used to create a 0.12 K/μm temperature gradient inside the capillaries [Furukawa FOL1405-RTV-617-1480, wavelength $\lambda = 1{,}480$ nm, 320 mW maximum power (AMS Technologies AG)]. Tryptophan fluorescence was excited with an ultraviolet light emitting diode (285 nm), and was measured with a 40x SUPRASIL synthetic quartz substrate microscope objective, numerical aperture 0.8 (Partec). The local receptor concentration in response to the temperature gradient was detected with a photon counter photomultiplier tube P10PC (Electron Tubes, Inc.). All measurements were performed at RT. The Hill equation ($n = 2$) was fit to the data to determine the EC50 value for each sample; the EC50 value is the concentration at which half of the GPCR sample is bound to its ligand.

ACKNOWLEDGMENTS. We thank members of Zhang lab for stimulating discussions. This work is supported in part by Defense Advanced Research Projects Agency HR0011-09-C-0012, the Center for NanoScience and the NanoSystems Initiative Munich. X.W. is also supported by a fellowship from China University of Petroleum (East China).

1. Wallin E, von Heijne G (1998) Genome-wide analysis of integral membrane proteins from eubacterial, archaean, and eukaryotic organisms. *Protein Sci* 7:1029–1038.
2. Loll PJ (2003) Membrane protein structural biology: The high throughput challenge. *J Struct Biol* 142:144–153.
3. Nilsson J, Persson B, von Heijne G (2005) Comparative analysis of amino acid distributions in integral membrane proteins from 107 genomes. *Proteins* 60:606–616.
4. Vauthey S, Santoso S, Gong H, Watson N, Zhang S (2002) Molecular self-assembly of surfactant-like peptides to form nanotubes and nanovesicles. *Proc Natl Acad Sci USA* 99:5355–5360.
5. Santoso S, Hwang W, Hartman H, Zhang S (2002) Self-assembly of surfactant-like peptides with variable glycine tails to form nanotubes and nanovesicles. *Nano Lett* 2:687–691.

6. von Maltzahn G, Vauthey S, Santos S, Zhang S (2003) Positively charged surfactant-like peptides self-assemble into nanostructures. *Langmuir* 19:4332–4337.
7. Nagai A, Nagai Y, Qu H, Zhang S (2007) Self-assembling behaviors of lipid-like peptides A6D and A6K. *J Nanosci Nanotechnol* 7:2246–2252.
8. Khoe U, Yang Y, Zhang S (2009) Self-assembly of nano-donut structure from cone-shaped designer lipid-like peptide surfactant. *Langmuir* 25:4111–4114.
9. Yeh JI, Du S, Tordajada A, Paulo J, Zhang S (2005) Peptergent: Peptide detergents that improve stability and functionality of a membrane protein glycerol-3-phosphate dehydrogenase. *Biochemistry* 44:16912–16919.
10. Kiley P, Zhao X, Bruce BD, Baldo M, Zhang S (2005) Self-assembling peptide detergents stabilize isolated photosystem I on a dry surface for an extended time. *PLoS Biol* 3:1181–1186.
11. Matsumoto K, Koutsopoulos S, Vaughn M, Bruce BD, Zhang S (2009) Designer lipid-like peptide surfactants stabilize functional photosystem I membrane complex in solution. *J Phys Chem* 115:75–83.
12. Zhao X, et al. (2006) Designer lipid-like peptides significantly stabilize G protein-coupled receptor bovine rhodopsin. *Proc Natl Acad Sci USA* 103:17707–17712.
13. Gaillard I, Rouquier S, Giorgi D (2004) Olfactory receptors. *Cell Mol Life Sci* 61:456–469.
14. Lindemann L, et al. (2005) Trace amine-associated receptors form structurally and functionally distinct subfamilies of novel G protein-coupled receptors. *Genomics* 85:372–385.
15. Migeotte I, Communi D, Parmentier M (2006) Formyl peptide receptors: A promiscuous subfamily of G protein-coupled receptors controlling immune responses. *Cytokine Growth Factor Rev* 17:501–519.
16. Bao L, Gerard NP, Eddy RL, Jr, Shows TB, Gerard C (1992) Mapping of genes for the human C5a receptor (C5AR), human FMLP receptor (FPR), and two FMLP receptor homologue orphan receptors (FPRH1, FPRH2) to chromosome 19. *Genomics* 13:437–440.
17. Rivière S, Challet L, Fluegge D, Spehr M, Rodriguez I (2009) Formyl peptide receptor-like proteins are a novel family of vomeronasal chemosensors. *Nature* 459:574–577.
18. Kaiser L, et al. (2008) Efficient cell-free production of olfactory receptors: Detergent optimization, structure, and odorant binding analyses. *Proc Natl Acad Sci USA* 105:15726–15731.
19. Zhao X, et al. (2010) Molecular self-assembly and applications of designer peptide amphiphiles. *Chem Soc Rev* 39:3480–3498.
20. Yaghmur A, Laggner P, Zhang S, Rappolt M (2007) Tuning curvature and stability of monoolein bilayers by designer lipid-like peptide surfactants. *PLoS One* 2:e479.
21. Cook BL, Ernberg KE, Chung H, Zhang S (2008) Study of a synthetic human olfactory receptor 17-4: Expression and purification from an inducible mammalian cell line. *PLoS One* 3:e2920.
22. Cook BL, et al. (2009) Large-scale production and study of a synthetic G protein-coupled receptor: Human olfactory receptor 17-4. *Proc Natl Acad Sci USA* 106:11925–11930.
23. Ren H, et al. (2009) High-level production, solubilization, and purification of synthetic human GPCR chemokine receptors CCR5, CCR3, CXCR4, and CX3CR1. *PLoS One* 4:e4509.
24. Leck K-J, Zhang S, Hauser CAE (2010) Study of bioengineered zebra fish olfactory receptor 131-2: Receptor purification and secondary structure analysis. *PLoS One* e15027.
25. Duhr S, Braun D (2009) Why molecules move along a temperature gradient. *Proc Natl Acad Sci USA* 103:19678–19682.
26. Baaske P, Wienken CJ, Reineck P, Duhr S, Braun D (2010) Optical thermophoresis for quantifying the buffer dependence of aptamer binding. *Angew Chem Int Ed Engl* 49:2238–2241.
27. Wienken CJ, Baaske P, Rothbauer U, Braun D, Duhr S (2010) Protein-binding assays in biological liquids using microscale thermophoresis. *Nat Commun* 1, doi: 10.1038/ncomms1093.
28. le Maire M, Champeil P, Moller JV (2000) Interaction of membrane proteins and lipids with solubilizing detergents. *Biochim Biophys Acta* 1508:86–111.